Actuator Leakage Fault Detection and Isolation Based on Extended Kalman Filtering Scheme

A thesis submitted

by

Liang An

to

The Department of Mechanical and Manufacturing Engineering

in partial fulfillment of the requirements

for the degree of

Doctor of philosophy

in the subject of

Mechanical Engineering

The University of Manitoba

Winnipeg, Manitoba

October 2006

THE UNIVERSITY OF MANITOBA

FACULTY OF GRADUATE STUDIES

*****

COPYRIGHT PERMISSION

Actuator Leakage Fault Detection and Isolation Based on Extended Kalman Filtering Scheme

BY

Liang An

A Thesis/Practicum submitted to the Faculty of Graduate Studies of The University of Manitoba in partial fulfillment of the requirement of the degree

Doctor of Philosophy

Abstract

In this research, the dynamics of a typical class of hydraulic actuators is studied and actuator leakage Fault Detection and Isolation (FDI) schemes are proposed based on the Extended Kalman Filtering (EKF) algorithm.

A dynamic model of the hydraulic actuation test rig combined with an actuator friction model is first derived. The parameters of the friction model are obtained by careful experiments. Simulations conducted to validate the model shows that the simulation errors are bounded within 10% of actual measurements and, within the normal operating bandwidth, the dynamic model adequately represents the actuator used in the test rig.

Based on the validated dynamic model, an offline actuator leakage fault detection scheme employing EKF algorithm is developed. Simulations and experiments are carried out to verify the effectiveness of the proposed FDI scheme without the presence of external disturbance. With a residual generation scheme that compared the actual measurements and the EKF estimates, three types of leakage - the cylinder chamber leakage at either side of the actuator and the leakage between the two chambers - are tested. The leakage faults are detected and identified by tracking the variation of the residual errors and an offline actuator FDI scheme is developed. The leakage identification patterns are recognized.

To further study the performance of the EKF based FDI scheme in normal operat-

ing conditions with external disturbances, the system model is improved to estimate any arbitrary load. Actuator friction is regarded as part of the external disturbance in this phase and, together with the environmental load, becomes a time-varying parameter of the system. Simulations and experiments show that the external load, including the actuator friction, can be accurately estimated. Different types of testing signals are applied to investigate the effectiveness of the FDI scheme. Experiments show that the leakage fault identification patterns are consistent with the conclusion obtained in the unloaded mode. A potential online FDI scheme and an offline actuator friction estimator are further proposed.

Acknowledgments

First and foremost I would like to express my sincere gratitude to professor Nariman Sepehri, an excellent professor and supervisor, for his patience, advice and support throughout the course of this research.

My gratitude also goes to professors Steve Onyshko and Waldemar H. Lehn, who acted as my committee members, for the time they spent reading and examining this thesis. Their valuable suggestions helped significantly improve the quality of my work.

Special thanks are also given to professor Christine Q. Wu and other professors and office staff who have given me assistance and inspiration in one form or another.

I am very grateful to my friends Mark Karpenko, Richard Song and Hairong Zeng, for their technical support and suggestions throughout the development of this thesis. I am also grateful to all other group members of the Robotics and Teleoperation Laboratory, whose knowledge and abilities helped me a great deal.

I would like to dedicate this work to my wife, Ping, whose love and whole-hearted support helped me to bring this work and my degree to completion. I would also like to give thanks to my parents, my brother and sisters for encouraging me in pursuing my education.

Contents

List of Figures

List of Tables

Nomenclature

Parameters and Variables

C_d	Orifice coefficient of discharge
q_1	Flow between servovalve and actuator cylinder chamber 1
q_2	Flow between servovalve and actuator cylinder chamber 2
w	Orifice area gradient
x_{sp}	Servovalve spool displacement
ρ	Density of hydraulic oil
p_s	Pump pressure
p_e	Return tank pressure
p_1	Pressure at cylinder chamber 1
p_2	Pressure at cylinder chamber 2
x_a	Actuator displacement
A	Effective piston area
β	Effective bulk modulus
V_1	Volume of the fluid trapped in cylinder chamber 1
V_2	Volume of the fluid trapped in cylinder chamber 2
q_{il}	Internal leakage across the piston seal
q_{el1}	External flow loss from chamber 1
q_{el2}	External flow loss from chamber 2

k_{il}	Leakage coefficient for internal leakage
k_{el1}	Leakage coefficient for external leakage flow at cylinder chamber 1
k_{el2}	Leakage coefficient for external leakage flow at cylinder chamber 2
V_1^0	Volume of the fluid trapped in supply pipe connecting cylinder chamber 1
V_2^0	Volume of the fluid trapped in supply pipe connecting cylinder chamber 2
X_{min}	Position of the actuator when fully retracted
X_{max}	Position of the actuator when fully extended
u	Valve input voltage
K_{sp}	DC gain of servovalve model
ω_n	Natural frequency of servovalve model
d_m	Damping ratio of servovalve model
f_a	Actuation force
m_a	Mass of ram
F_c	Actuator friction
f_{st}	Static stick friction of friction model
f_{sl}	Slip friction of friction model
d	Damping ratio of friction model
α	Decay ratio of slip friction in friction model
v_o	Threshold for zero in discrete friction model
$\mathbf{x}$	System state vector
x_i	System state variable
$\mathbf{x}_k$	Discrete system state vector
$\mathbf{A}$	Transition matrix $(n \times n)$

$\mathbf{B}$	Input matrix $(n \times r)$
$\mathbf{W}$	Process noise matrix $(n \times s)$
$\mathbf{w}$	Process noise vector $(s \times 1)$
$\mathbf{H}$	Measurement matrix $(m \times n)$
$\mathbf{v}$	Measurement noise vector $(m \times 1)$
$\mathbf{Q}$	Covariance matrix of process noise $(m \times n)$
$\mathbf{R}$	Covariance matrix of measurement noise $(m \times n)$
$\mathbf{P}_k$	Covariance matrix of the transition matrix
$\mathbf{P}_k^-$	*a priori* covariance matrix of the transition matrix at discrete moment k
$\mathbf{P}_k^+$	*a posteriori* covariance matrix of the transition matrix at discrete moment k
$\mathbf{z}_k$	Measurement at discrete moment k
$\hat{\mathbf{x}}_k^-$	*a priori* estimation of state vector at discrete moment k
$\hat{\mathbf{x}}_k^+$	*a posteriori* estimation of state vector at discrete moment k
$\mathbf{K}_k$	Kalman gain matrix at discrete moment k
$\mathbf{P}_o^+$	Initial covariance matrix of transition matrix
$\hat{\mathbf{x}}_o^+$	Initial state vector
$\mathbf{f}(\cdot)$	Nonlinear model of the system
f_i	ith component of nonlinear model $\mathbf{f}(\cdot)$
$\mathbf{e}$	Residual error vector
e_a	Moving average of residual error
$\bar{k}_{el1}$	Average leakage coefficient at cylinder chamber 1
$\bar{k}_{el2}$	Average leakage coefficient at cylinder chamber 2
$\bar{k}_{il}$	Average internal leakage coefficient

σ_{el1}	Standard deviation of the external leakage coefficient at cylinder chamber 1
σ_{el2}	Standard deviation of the external leakage coefficient at cylinder chamber 2
σ_{il}	Standard deviation of the internal leakage coefficient
F_r	Load generated by environment
F_e	Effective external load
$\boldsymbol{\xi}$	State vector of the extended system model
$\boldsymbol{\theta}$	State vector representing time-varying parameters of the extended model

Abbreviations

MAE	Moving Average Error
KF	Kalman Filter
EKF	Extended Kalman Filter
ANN	Artificial Neural Network
FDI	Fault Detection and Isolation
VDP	Variable Displacement Pump
LC	Leakage Coefficient
EBM	Effective Bulk Modulus

Chapter 1

Introduction

1.1 Preliminary Remarks

With the rapid development of modern machinery, hydraulically powered machines are widely used in various fields. Due to their complexities, the reliability of these systems is under serious consideration. As a result, fault detection and isolation (FDI) techniques for hydraulic systems have been growing in the past decade. This growth benefited greatly from the development of personal computers. More and more computationally intensive methods can now be applied to this research area. However, due to its nonlinearity, hydraulic FDI technology is far from satisfactory.

Typical hydraulically powered systems consisting of hydraulic pumps, solenoid servovalves and hydraulic actuators are popular in industrial applications, such as the airplane flight control and off-highway machines. Since the reliability of these systems is crucial for safe operation, a sound diagnostic system can efficiently improve the safety by detecting and identifying the faults. In some applications such as the unmanned flight vehicle operation, the system is required to keep working with the presence of faults. When this occurs, if the information of the fault can be obtained and analyzed, the control system can be adjusted or different control strategies

can correspondingly be applied to implement fault tolerant control. Furthermore, a diagnostic system can report abnormal operating conditions to prevent the faulty system from more serious damage.

1.2 Faults in Hydraulic Systems

1.2.1 Basic System Structure

In the aforementioned hydraulic actuation systems, hydraulic power supplies are always necessary to pressurize the hydraulic fluid to a constant pressure, typically 3.5 to 21 MPa. This high-pressure flow is then regulated by the control valves and delivered to the actuator. The actuator, consisting of a cylinder that is separated into two chambers by a movable piston, is connected to the corresponding outlets of a servovalve. The flow at the outlets is controlled by an electric input; therefore the piston in the cylinder is pushed by high-pressure flow causing it to move according to the input signal. In practice, a rod is attached to the piston to transfer force between the actuator and the load.

1.2.2 Common Faults and Related Research

When the system above is considered, various papers show that faults may occur at any of the three components (Skormin and Apone, 1995; Zhou et al., 2002; Zavarehi et al., 1999; Khan and Sepehri, 2002; Zhang and Jiang, 2002). The topics cover a wide range from mechanical component failure, fluid contamination and pipe leakage to metal wear. One of the greatest concerns among these topics is the leakage of hydraulic fluid. Since the high pressure propagates everywhere within the hydraulic pipe, leakage can occur almost anywhere in the system. According to its location,

leakage can be classified into two types: internal leakage and external leakage. If the fluid leaks to another part of the fluid circulation within the hydraulic system, it is internal leakage; if the fluid leaks out of the hydraulic circulation, it is external leakage.

Leakage Faults

Leakages in hydraulic systems are caused by different sources. One primary source is the wear of the valves, pistons and other moving components. Debris caused by the wear in turn accelerates the process (Skormin and Apone, 1995). Mechanically, a tiny leakage is designed between the moving parts to guarantee non-stick movement without excessive friction and to supply necessary lubrication for the contact surface (slippers, bearings, barrel and drive shaft of the pump) (Skormin and Apone, 1995). The contamination particles can gradually deteriorate this condition by widening the clearance between the moving parts and eventually cause the performance of the system to fall below the tolerable level of the design. Component defect and connection damage are other causes that contribute to the leakage faults.

In the hydraulic power supply, leakage occurs mainly around the pump. Among these hydraulic pumps, a class of Variable Displacement Pumps (VDP) is broadly applied. Driven by an electric motor, the barrel of the VDP, which contains cylinders and pistons, rotates. The pistons are attached to the swashplate by their slippers and the slippers/pistons are rotated inside the barrel along the face of the swashplate. The pistons move in and out so that the hydraulic fluid is drawn into VDP through the suction port and is expelled out of VDP through the discharge port. The swashplate angle is adjustable to regulate the pressure of outlet flow. Skormin and Apone (1995)

analyzed the mechanism of typical failures of hydraulic pumps, including the leakage and its causes.

Leakage in the actuator is another cause of leakage faults. Both the seal of the piston and the inner wall of the cylinder can wear during the running time. As a result, the clearance in between permits more hydraulic fluid to flow across the chambers. This cross-port leakage is an internal leakage and may cause the actuator to stall if it deteriorates. Extra power is then needed from the pump to compensate the pressure loss from the cross-port leakage.

Skormin et al. (1994) built a linear model for a hydraulic actuation system in which the leakage faults, the control valve fault, the bulk modulus change and the excessive friction fault were discussed. Crowther et al. (1998) simulated the cross-port leakage of an actuator by introducing a cross-port bleed valve between the annulus and the piston sides. External leakages at connecting pipes and couplers were of less interest among researchers but still drew attention. Ashton et al. (1998) showed their work on detecting the pipeline leakage for oil transportation with a nonlinear observer. The model is, however, not suitable for complexities of hydraulic actuation systems.

Other Faults under Investigation

Supply pressure fluctuation is a type of common fault that occurs in hydraulic systems. A malfunctioning pump causes supply pressure fluctuations that seriously affect the performance of the actuator. Most commercial power supplies regulate the pressure by adjusting the pressure relief valve. According to Merritt (1967), valve controlled hydraulic systems are most efficient when designed such that the maximum

load pressure is approximately 68% of the nominal supply pressure. Therefore, a drop in supply pressure leads to a less efficient system. In extreme situations, stalling of the actuator occurs. On the other hand, excessive supply pressure causes accelerated wear on the hydraulic components. This may lead to unexpected behavior in which serious damage may occur. Rising pressure will eventually destroy the power supply unit if the situation is not corrected in time.

The causes of fluctuation in supply pressure vary. In some cases, the malfunction is due to the breach of delicate components of the pump and valves. This changes the characteristics of the pump, such as the motor efficiency and total inertia (Yu et al., 1997). Preston et al. (1996) simulated the system dynamics with a 10% drop in pump pressure. An increase of the initial force on the adjustable springs of a bent-axis type VDP was investigated by Zhou et al. (2002). Partially or entirely damaged connection between the pump and the rest of the system can also cause significant loss of pressure on the whole system. In severe cases, the supply pressure may be reduced to between 40% (Crowther et al, 1998) and 60% (Niksefat and Sepehri, 2002) of the nominal value. Broken pipes and blocked high-pressure filters are common explanations for this type of failure.

Fluid contamination also directly causes an array of problems by changing the effective bulk modulus (EBM) of the hydraulic oil. EBM describes the stiffness as both the compressibility of the fluid and the expansion of the cylinder, hoses or pipes. An important indicator for fluid characteristics, EBM is sensitive to fluid contaminants such as water and air. The properties of mechanical components are generally unchanged (Skormin and Apone, 1995). Small amounts of solid contaminants, such

as dirt, metal, sand and rubber, do not cause significant change on EBM, though they do contribute considerably to component wear. Water and air entrained in the fluid are crucial to the hydraulic characteristics. Since the bulk modulus of air as compared to hydraulic fluid is so small, a tiny amount of air trapped in the hydraulic circuit considerably reduces EBM. This results in a slower system response and softens the characteristics of the actuator when the load is applied. On the contrary, water drops mixed in hydraulic fluid increase EBM as the bulk modulus of water is higher than that of the hydraulic fluid. Therefore, the stiffness of the system increases.

Skormin and Apone (1995) reported a drop of 20% in EBM where air contamination exists. An increase of 10% in EBM due to water contamination was also reported in the same paper. Yu (1997) showed that a change of 10% in EBM could be detected. Furthermore, Zavarehi et al. (1999) showed that change in EBM had little influence on the performance of a proportional servovalve.

Other system faults caused by parameter changes are studied in various research papers. Servovalves, the primary executors of control commands, are important parts for hydraulic systems. Popular servovalves are designed to have at least two stages so that they are sensitive and can swiftly respond to the control signals while supplying enough power to drive the actuator. Zavarehi et al. (1999) constructed a nonlinear model for a two-stage proportional servovalve. With this model, critical parameters such as the effective orifice area of the servovalve were monitored using the extended Kalman filter. Their research shows the possibility to diagnose servovalve faults caused by component wear, which is the main cause for change of the effective orifice area.

Coulomb friction of moving components as an important parameter can significantly affect the dynamic performance of an actuator. Lischinsky et al. (1999) showed this friction may go up to 30% of the total driving force. Crowther et al. (1997) simulated dynamic friction of the load using a bleed valve across the load actuator and observed change of the friction coefficient with a trained neural network. The pilot spool friction in a two-stage servovalve was monitored by Zavarehi et al. (1999).

Research on mechanical and electrical failures of system components is relatively sparse. Loss of magnetism of the pump motor was considered by Skormin and Apone (1994). Zhou et al. (2002) presented loss of the compressed air that was supplied to the reservoir in aircraft applications.

In this study, leakages on the actuator are considered.

1.3 Fault Detection and Diagnosis in Hydraulic Systems

As a branch of fault detection and isolation (FDI) research, FDI for hydraulic systems has developed rapidly in the past decade. Hydraulic system FDI is relatively difficult due to the strong nonlinearity of hydraulic components. In spite of this, researchers have accomplished many achievements. Several system-modeling techniques have been developed for reconstructing nonlinear system information and variation detection. Residual generation strategies are also put forward to handle the nonlinearities.

1.3.1 Parametric Model-Based FDI Schemes

As a general system identification method, least squares (LS) algorithm or, in its numerically efficient form, recursive least squares (RLS) is suitable in practical applications where the process parameters are not known at all or just partially known. Models based on this algorithm are called auto regressive with exogenous input (ARX) models. Using this algorithm, the process model can be expressed in terms of a parameter vector and running-time data vectors. Sampling at a certain frequency, the actual process is discretized and the parameters are estimated by minimizing the sum of squares of the equation error. Therefore, the basic idea of RLS is to find a proper parameter vector so that the system represented by this model best fits the physical system and the determination of the vector is based on the parameter estimation methods which utilize input and output sequences of the system.

Since implementation of the model is not unique, an appropriate realization of the model is the key for obtaining correct parameter estimates (Isermann, 1992). Yu (1997) showed an application of ARX parameter estimation on a hydraulic torque rig. If the basic structure of the model is known, the order of the LS model or the dimension of the parameter vector can be readily obtained. Otherwise, theoretical determination of the ARX model is impossible, which is common in actual applications. Obtaining a best-fit parameter vector without losing too much system information is the only feasible strategy. Hahn et al. (2001) applied an empirical model in a vehicle power auto-transmission control system. The order of the ARX model was obtained by trial-and-error and was then adjusted from the tenth to the second order to simplify the representation of the system.

Although simplification of system model is possible, the mismatch of model parameters and system parameters, however, incurs a problem for FDI research - elements of the acquired parameter vector are irrelevant to actual physical parameters of the system. In attempting to solve this problem, the concept of vector space was developed by Tan and Sepehri (2002) who showed a way to construct this space. The pattern of faults in this vector space could be classified by neural networks.

On the other hand, the linear nature of RLS confines its applications in nonlinear systems. An improved algorithm called RLS with forgetting factor was developed to handle this drawback. The forgetting factor exponentially removes the influence of old data when new measurements become available. However, only slow time-varying systems can be considered because convergence of this algorithm is always a concern when only limited data are available for nonlinear system. Song and Sepehri (2002) showed a possible way for sinusoidal signal fault detection of pump fault in a hydraulic actuator using this algorithm. Pump pressure fluctuation fault was discussed and sinusoidal test signals were applied to the experimental results.

1.3.2 Observer-Based FDI Schemes

State-observer techniques for linear systems have been well developed. Meanwhile, attempts to extend observers into nonlinear applications have also been conducted. As a result, different types of observer have been developed to explore their feasibilities of estimating state variables, which are essential for abnormal condition monitoring. According to Garcia and Frank (1997), observers can be classified into nonlinear identity observer (NIO), nonlinear unknown input observer (NUIO), disturbance-decoupling nonlinear observer (DDNO), adaptive nonlinear observer (ANO) and bilinear systems

state observer (BSO).

NIO is asymptotically stable if a feedback gain matrix satisfies certain conditions (Adjallah et al., 1994). In some cases, the feedback gain matrix can be a constant matrix if the nonlinear system representation satisfies certain constraints (Frank, 1987). Gaddouna and Ouladsine (1997) applied a linear state observer with unknown input to a hydraulic system. A similar observer was built by Hahn (2001) and the state model was identified using RLS algorithm.

NUIO takes advantage of the structure of the system model, which is assumed to be in observable canonical form and a constant state transformation is conducted. However, since it is difficult to transform a general system into the required form, its applications on nonlinear systems are limited. Khan et al. (2002) showed the possibility of applying a nonlinear observer on a hydraulic test rig. As an improvement of NUIO, DDNO basically applies the same idea as NUIO except that a nonlinear state transformation is used rather than a linear one. It linearizes the system at a chosen set point and approximates the system by omitting the second and higher order terms in the linear expansion of the system. On solving the problem of the weakness in detecting slowly developing faults, ANO is developed. In certain types of nonlinear systems, bilinear models are studied and applied to suspension systems, fermentation processes, hydraulic drives and heat exchange systems. Yu et al. (1994) developed a bilinear fault detection scheme for hydraulic systems with BSO. Similar work has also been reported by Preston et al. (1996).

1.3.3 Artificial Neural Network-Based FDI Schemes

Artificial neural network (ANN) as a newly developed technique has found its applications in many fields that require pattern recognition and parameter approximation. ANNs have different structures, among which is the well-known structure of multi-layer perceptron (MLP). This type of ANN consists of several layers and each of those layers contains a number of processing nodes, called neurons. The first layer is called the input layer, the last layer the output layer, while the layers in between are defined as hidden layers. Different layers are coupled by connections that identify themselves as weight matrices. When fed with actual system inputs in training stage, ANN achieves self-regulation to approximate the actual system output by adjusting values of the weights that connect different neurons. A sensitive but slow algorithm for this learning phase is called Back Propagation. This algorithm updates all weights iteratively from the last layer to the first. However, it does not guarantee a convergence, which is a major disadvantage of MLP networks. By forcing the training phase to an end, the user can obtain a perceptron network based on the training data with minimum error.

Crowther et al. (1998) presented an output vector space classification approach for increased pump pressure, increased actuator friction and internal leakage fault diagnosis of a hydraulic actuator. It shows that, training separate ANNs alone using experimental data for specific fault allows quick and accurate detection for that fault. But these ANNs are not sensitive to faults other than that they are trained to detect. Yu (2001) also showed a 3-layer perceptron network for fault diagnosis in a hydraulic turbine governor.

1.3.4 Kalman Filtering Theory-Based FDI Scheme

The Kalman filter (KF) theory is another widely applied technique in nonlinear and stochastic system modeling such as navigation problems (Sridhar et al, 1993; Foresti, 2001). Based on state space modeling, the Kalman filter (KF) is developed to recursively estimate system states. Mathematically, Kalman filter theory relies on Bayesian estimation to obtain the *a posteriori* estimate of current states by correcting the *a priori* estimate using the current measurements of outputs. If the system is fully observable, all state variables can be estimated utilizing system input and output sequences. Due to its mathematical nature, KF works not only on static systems, but also on dynamic systems, while linearity is a sufficient condition. To apply KF to nonlinear systems, researchers developed extensions of Kalman filter algorithms called extended Kalman filters (EKF). The basic idea of EKF is to linearize the system based on the latest estimation of system states. If the sampling interval is small enough, the output of EKF estimator can converge to the system output with satisfactory precision.

Both the KF and the EKF algorithms consist of two stages: (i) time updating phase, which uses system equations that represent the actual process to calculate the evolution of the state and, (ii) measurement updating phase, which corrects the estimation with current measurements to obtain the *a posteriori* estimation.

The applications of KF and EKF estimation in fault diagnosis have been reported in many industrial areas. However, few literatures have been contributed to hydraulic power systems. Abbas (1998) applied this algorithm in a linear electrohydraulic drive system. Zavarehi et al. (1999) showed the feasibility of applying EKF algorithm in

modeling a two stage proportional servovalve. With the presence of friction in the model, this paper shows that it is possible to monitor some key parameters of the servovalve. Zhang and Jiang (2002) developed an active fault-tolerant control scheme for a class of aircraft actuators. An adaptive Kalman filter was applied in their research to detect parameter changes and the system representation was specially constructed so that an effectiveness factor was introduced to indicate the seriousness of the faulty mode. However, the system was linearized to simplify the problem and only simulation studies were conducted. Chinniah et al. (2003) developed an EKF based method to estimate the parameters of an actuator friction model as well as the effective bulk modulus of the hydraulic fluid. When actuator leakages are considered, no literature has been reported focusing on nonlinear actuation systems.

1.4 Objectives and Scope of This Research

With all the reviewed research and attempts shown in Section 1.3, hydraulic FDI is still under development and is attracting much attention. This study presents the application of EKF towards hydraulic actuator leakage FDI. It focuses on the leakage faults around a typical hydraulic actuator that is widely used on aircrafts. These leakage faults include external leakage on either side of the actuator cylinder and the cross-port internal leakage between the two cylinder chambers.

The objective of this study is to firstly verify the feasibility of applying EKF to nonlinear electrohydraulic actuation systems. A nonlinear model for an actuator test rig will be developed and simulation results will be shown to verify the model and the EKF based FDI scheme. Secondly, an offline leakage FDI scheme using EKF

algorithm will be developed and tested with experiments. In this phase, different input signals, including sinusoidal, step and pseudorandom signals will be applied to the test rig. Thirdly, the external load will be included and the system model and FDI scheme will be modified to accomplish online fault detection. A simple external load will be set up to simulate environmental interaction.

1.5 Thesis Outlines

This thesis consists of eight chapters. Chapter 1 introduces hydraulic system applications and the development of FDI techniques. The scope and objectives of this research are also outlined in this chapter.

Chapter 2: The electrohydraulic actuation test rig is introduced in this chapter. Specifications of the test rig are listed and the system structure is diagrammed. Nonlinear dynamic equations and a mathematical model of the test rig are developed.

Chapter 3: The system model that takes dynamic effects and was developed in Chapter 2 is validated in this chapter by simulation. The simulation results are compared with actual running data obtained from the test rig to verify the fidelity of the model.

Chapter 4: The Kalman filtering algorithm is introduced in this chapter and the basic FDI scheme is developed, based on EKF algorithm.

Chapter 5: The FDI scheme developed in Chapter 4 is validated in this chapter. Different types of signal are tested on the test rig and the results are discussed to illustrate the effectiveness of this FDI scheme. An offline FDI scheme is summarized at the end of this chapter.

Chapter 6: The system model and the FDI algorithm are further developed to include unknown external load. With this development, the FDI scheme has the potential to detect actuator leakages when the actuator is in faulty but running condition.

Chapter 7: Simulation and test results are elaborated in this chapter to illustrate the effectiveness of the FDI scheme developed in Chapter 6.

Contributions made in this study are provided in Chapter 8.

Chapter 2

Experimental Test Rig Configuration and System Modeling

2.1 Experimental Setup

The experimental setup is shown in Figure 2.1 and its schematic is shown in Figure 2.2. The entire system is powered by a motor driven hydraulic pump, which offers continuous and stable high-pressure hydraulic fluid (up to 18.27MPa, i.e., 2650psi) to the actuator.

The actuator is a double-rod cylinder. Since the actuator is symmetric and can actually move in either direction, modeling of the two chambers are identical. The two chambers are thus noted as chamber 1 and chamber 2. The actuator is connected to and controlled by a Moog D765 servovalve (see Figure 2.2). This servovalve receives control signals from a PC equipped with a DAS-16 data acquisition board and a Metrabyte M5312 encoder card. When operated at 20.7MPa (3000psi), Moog D765 valve can supply the actuator with hydraulic fluid at a rate of 34L/min. In the experiments, the actual operating pressure is set to $\sim$ 13.8MPa (2000psi). All

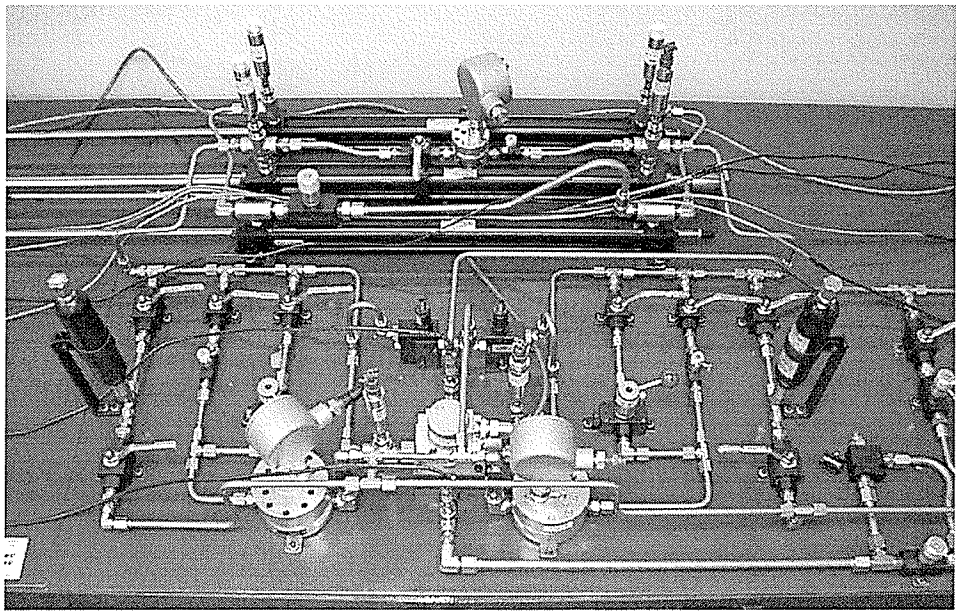

Figure 2.1: Hydraulic actuator and fault simulation system.

the control strategies and experimental algorithms are implemented on the PC with a Pentium III processor. Using a Metrabyte M5312 quadrature incremental encoder card, the displacement of the actuator can be measured. With its rotary optical encoder, M5312 reaches a resolution of 0.03mm per increment. Other necessary system states are measured by transducers mounted on the hydraulic circuit and transmitted to the DAS-16 board; meanwhile, the DAS-16 board also transmits control signals from PC to Moog D765 valve.

Figure 2.3 shows the leakage faults the test rig can simulate. Since the actuator is symmetric, the positive direction for the rod's movement is arbitrarily defined and the cylinder chambers of the actuator are labeled accordingly. The entire system structure is shown in Figure 2.4.

Working as a fault simulator, the test rig is designed to reproduce common faults

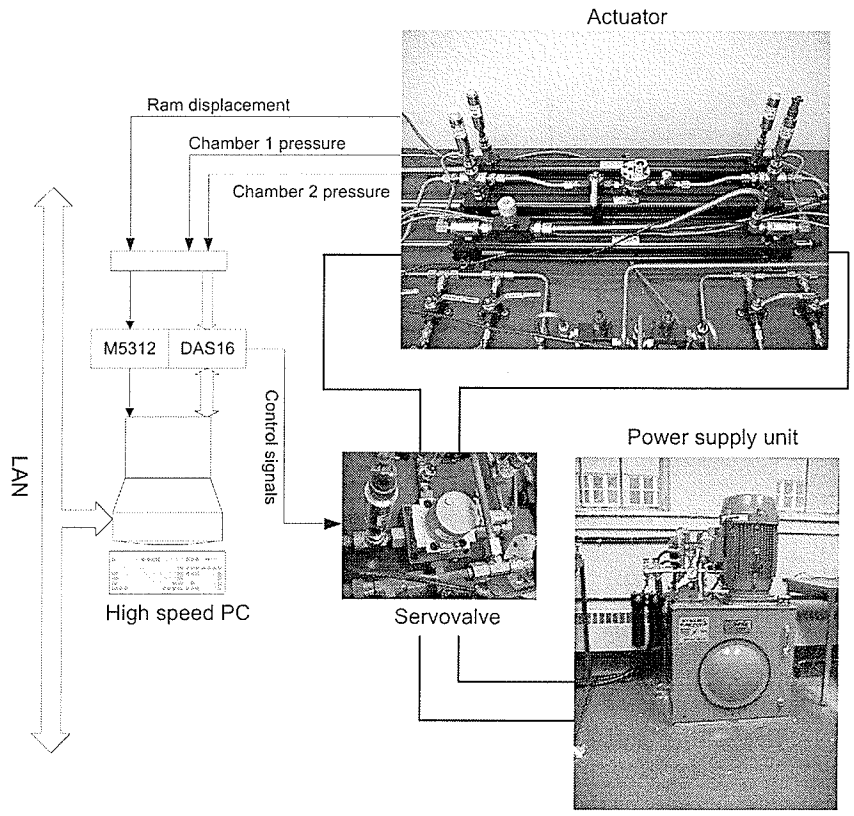

Figure 2.2: Hydraulic test rig with its interfacing.

in the actuator. These include the external leakage at both chambers of the actuator cylinder, the internal (cross-port) leakage between the two chambers, the supply line leakage and the return line blockage (filter blockage). In this study, only actuator leakages are considered. Figure 2.5 shows pictures of the bypasses where the external leakages occur. The pipe shown in the center of both pictures consists of a bypass that communicates the corresponding chamber and the return line. Two valves, a ball valve and a needle valve, are mounted in series on each of the bypasses. The ball valve is designed to break the hydraulic flow, while the needle valve can be finely

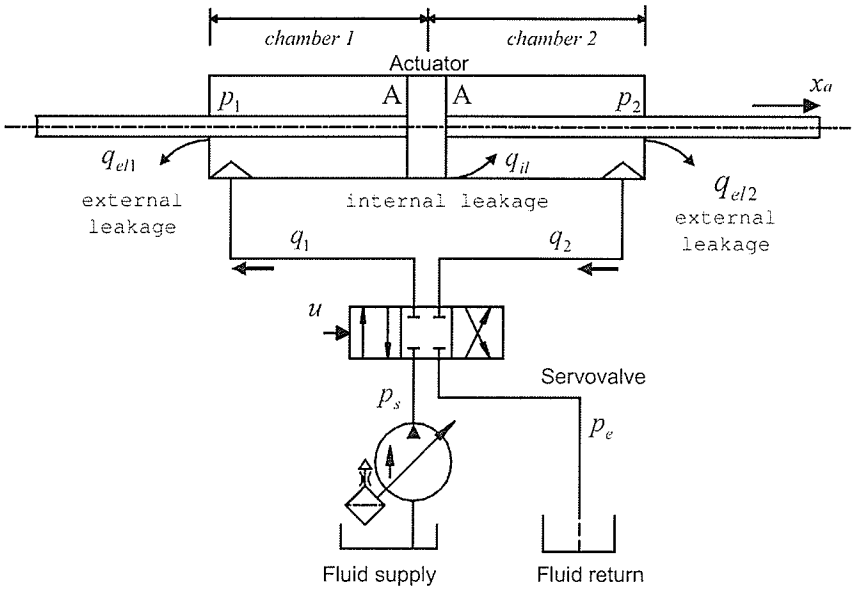

Figure 2.3: Schematic of actuator leakages faults.

tuned to create specific amount of leakage at the chamber it links to. The bypass mechanism for both chambers is similar.

The bypass for the cross-port leakage simulation is shown in Figure 2.6a and has the similar mechanism as external leakages. A flow meter is mounted between the ball valve and the needle valve. This arrangement is also applied to the pump leakage simulation, shown in Figure 2.6b.

2.2 Dynamic Equations

Understanding the dynamic features of the servovalve and the actuator is essential. The dynamics of a high performance servovalve can be properly represented by equations given by Merritt (1967). Given the shape of the discharge orifices, various

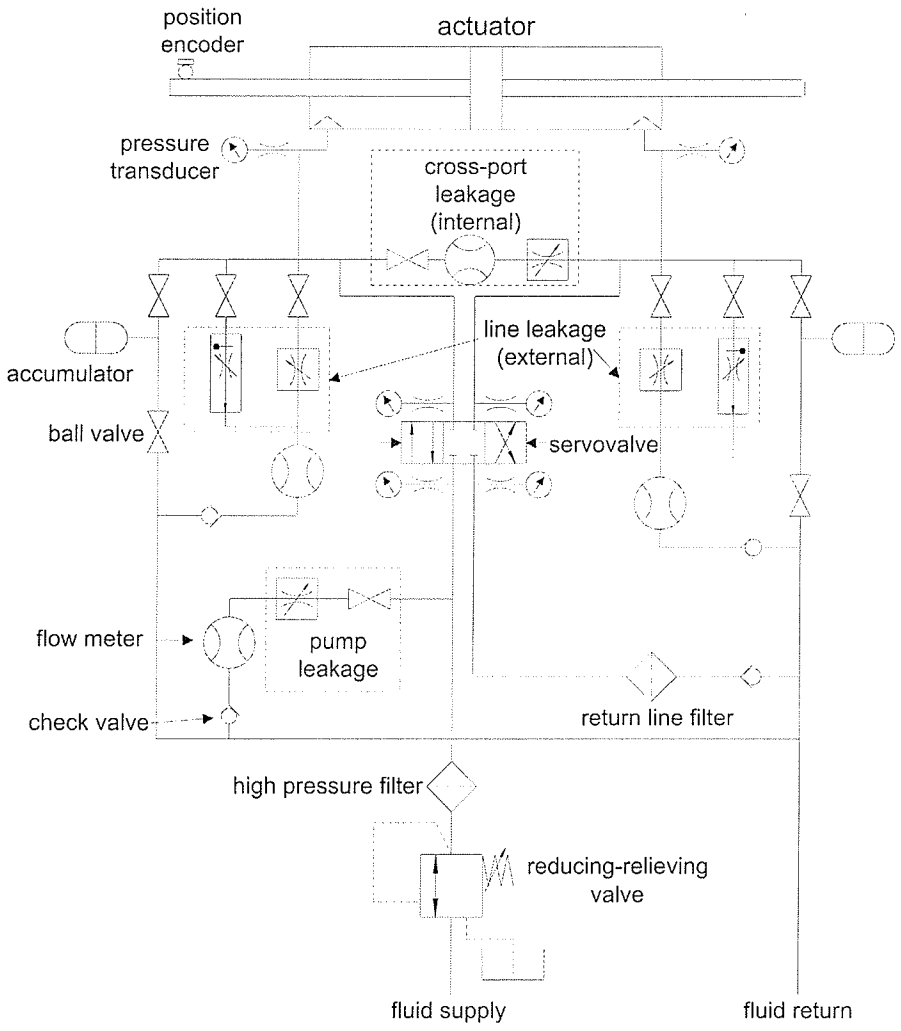

Figure 2.4: Detailed schematic of actuation system showing sensors and bypasses.

models between the spool displacement and the flow can be developed. By applying a linear orifice area gradient related to the spool displacement, the flow equations of the servovalve become:

$$\begin{cases} q_1 = C_d w x_{sp} \sqrt{\frac{2}{\rho}(p_s - p_1)} \\ q_2 = C_d w x_{sp} \sqrt{\frac{2}{\rho}(p_2 - p_e)} \end{cases} \quad x_{sp} > 0 \tag{2.1}$$

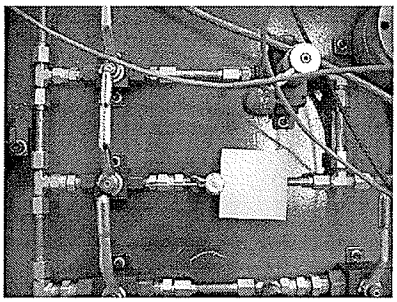

(a) Chamber 1

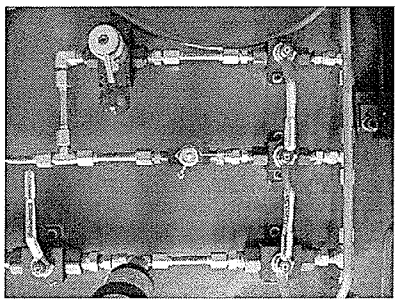

(b) Chamber 2

Figure 2.5: Bypasses for external leakages at either chamber of the actuator cylinder.

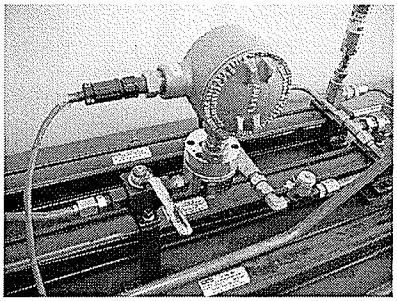

(a) Bypass for crossport leakage

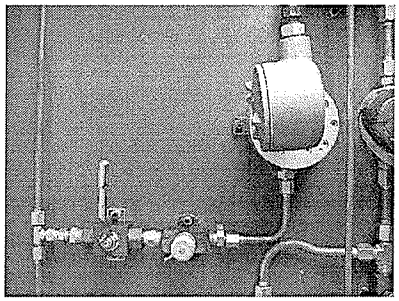

(b) Bypass for pump leakage

Figure 2.6: Bypasses for cross-port leakage and pump leakage.

$$\begin{cases} q_1 = C_d w x_{sp} \sqrt{\frac{2}{\rho}(p_1 - p_e)} \\ q_2 = C_d w x_{sp} \sqrt{\frac{2}{\rho}(p_s - p_2)} \end{cases} \quad x_{sp} < 0 \tag{2.2}$$

where q_1 and q_2 are the flows between the servovalve and the chambers 1 and 2 of the actuator. Pressures p_s and p_e are the pump pressure and the return pressure. The pressures at chamber 1 and chamber 2 of the cylinder are given as p_1 and p_2. Variable x_{sp} is the displacement of the spool of the servovalve. Servovalve parameters C_d and w are the orifice coefficient of discharge and the orifice area gradient; and ρ is the density of the hydraulic oil.

Continuity equations for hydraulic flow of the actuator in which internal and

external leakage are modeled, are

$$\begin{cases} q_1 = A\dot{x}_a + \frac{1}{\beta}V_1(x_a)\dot{p}_1 + q_{il} + q_{el1} \\ q_2 = A\dot{x}_a - \frac{1}{\beta}V_2(x_a)\dot{p}_2 - q_{il} + q_{el2} \end{cases} \tag{2.3}$$

A is the effective piston area; x_a represents the actuator displacement; effective bulk modulus of the hydraulic fluid is indicated by β. Internal leakage flow across the piston seal is q_{il}. External flow leaks from chamber 1 and 2 of the actuator are q_{el1} and q_{el2}, respectively. More detailed discussion about leakage modeling will be elaborated in Chapter 5. $V_1(x_a)$ and $V_2(x_a)$ are the volumes of fluid trapped in corresponding chambers of the actuator, and are formulated by the following equations:

$$\begin{cases} V_1(x_a) = V_1^0 + A(x_a - X_{min}) \\ V_2(x_a) = V_2^0 + A(X_{max} - x_a) \end{cases} \tag{2.4}$$

where V_1^0 and V_2^0 are volumes of fluid trapped in the supply pipes connected to chamber 1 and chamber 2, estimated from the test rig. X_{min} and X_{max} are the positions when the ram is fully retracted and fully extended. Although equation (2.3) represents the general form of continuity dynamics, only a healthy system is modeled with the intention to detect the variation caused by the leakages. As a result, leakages q_{il}, q_{el1} and q_{el2} will be simulated to produce leakages in the program and estimated in experiments.

The dynamics of the servovalve are characterized by a typical linear second-order system between the spool displacement, x_{sp}, and the valve input voltage, u.

$$u = \frac{1}{k_{sp}\omega_n^2}\ddot{x}_{sp} + \frac{2d_m}{k_{sp}\omega_n}\dot{x}_{sp} + \frac{1}{k_{sp}}x_{sp} \tag{2.5}$$

where ω_n is the natural frequency; k_{sp} is the DC gain, and d_m is the damping ratio.

The dynamics of the actuator are modeled based on the pressure difference between the inlet and the outlet side of the cylinder. This pressure difference generates the force, f_a, which pushes the piston in the cylinder.

$$f_a = (p_1 - p_2)A \tag{2.6}$$

The dynamic equation of an ideal unloaded actuator is

$$m_a \ddot{x}_a = f_a \tag{2.7}$$

where m_a is the mass of the ram.

2.3 Actuator Frictions

As an inevitable factor in moving machinery, friction and its impact have to be handled carefully. In hydraulic actuators the seals' friction is substantial due to the high fluid pressure and may account for up to 30% of the total driving force (Lischinsky et al, 1999). Because the existence of friction significantly changes the dynamics of the system, researchers have put considerable efforts into modeling friction. In its simplest form, friction can be modeled as a sign function with non-unity magnitudes. However, this simple form generally does not satisfy the modeling requirement. For this reason, additional models are developed to describe the dynamic features of friction. A typical stick-slip friction model was proposed by Karnopp (1985). Also reported were state space representation (Canudas-de-Wit et al., 1995) and empirical models (Kwak, et al., 1999; Bonchis et al., 1999). After extensive experiments on the test station, the improved Karnopp model by Laval (1996) has been adopted in this

research to model the friction in the actuator. The final form of the model is

$$F_c = \begin{cases} [f_{st} - (f_{st} - f_{sl})(1 - e^{-\frac{|\dot{x}_a|}{\alpha}})]\text{sgn}(\dot{x}_a) + d\dot{x}_a & \dot{x}_a \neq 0 \\ f_a & f_a < f_{st} \quad \& \quad \dot{x}_a = 0 \\ f_{st} & f_a \geq f_{st} \quad \& \quad \dot{x}_a = 0 \end{cases} \tag{2.8}$$

in which, $\dot{x}_a$ is the velocity of the actuator and F_c is the actuator friction. The static friction and the slip friction are f_{st} and f_{sl}, respectively. Factor α works as the constant that decides the decay ratio from stick friction to slip friction, while d is the effective damping ratio. The function sgn$(\cdot)$ is a sign function that can be expressed as:

$$\text{sgn}(\dot{x}_a) = \begin{cases} \frac{\dot{x}_a}{|\dot{x}_a|} & \dot{x}_a \neq 0 \\ 0 & \dot{x}_a = 0 \end{cases} \tag{2.9}$$

Equation (2.8) shows that the friction force is dependent on the actuator force when the actuator is still. This definition guarantees that static friction is always opposing the driving force with the same magnitude preventing it from moving. After the actuator starts to move, the friction starts from the stiction when the actuator velocity is close to zero and then decreases when the velocity increases. When the velocity increases more, the influence of the actuator viscosity becomes significant. The Karnopp model is a symmetric model. However it can be adjusted to be asymmetric in implementation, which is critical for actual applications. With this model, equations (2.6)and (2.7) are combined to form the following

$$f_a = (p_1 - p_2)A = m_a\ddot{x}_a + F_c \tag{2.10}$$

2.4 State Space Model

Based on equations (2.1) to (2.10), the nonlinear state space model for the entire system under normal operating condition can be constructed. Choosing the state vector

$$\mathbf{x} = [x_1, x_2, x_3, x_4, x_5, x_6]^{\mathrm{T}} = [x_{sp}, p_1, p_2, x_a, \dot{x}_a, \dot{x}_{sp}]^{\mathrm{T}} \tag{2.11}$$

The state space model for the servovalve and the actuator is shown below.

$$\begin{cases} \dot{x}_1 = x_6 \\ \dot{x}_2 = \begin{cases} \frac{\beta}{V_1(x_4)}[C_d w x_1 \sqrt{\frac{2}{\rho}(p_s - x_2)} - A x_5] & x_1 > 0 \\ \frac{\beta}{V_1(x_4)}[C_d w x_1 \sqrt{\frac{2}{\rho}(x_2 - p_e)} - A x_5] & x_1 < 0 \end{cases} \\ \dot{x}_3 = \begin{cases} \frac{\beta}{V_2(x_4)}[-C_d w x_1 \sqrt{\frac{2}{\rho}(x_3 - p_e)} + A x_5] & x_1 > 0 \\ \frac{\beta}{V_2(x_4)}[-C_d w x_1 \sqrt{\frac{2}{\rho}(p_s - x_3)} + A x_5] & x_1 < 0 \end{cases} \\ \dot{x}_4 = x_5 \\ \dot{x}_5 = \frac{1}{m_a}(A x_2 - A x_3 - F_c(x_5)) \\ \dot{x}_6 = -2 d_m \omega_n x_6 - \omega_n^2 x_1 + k_{sp} \omega_n^2 u \end{cases} \tag{2.12}$$

F_c represents the actuator friction. With the definition of the state variables, equation (2.8) becomes the following:

$$F_c(x_5) = \begin{cases} [f_{st} - (f_{st} - f_{sl})(1 - e^{-\frac{|x_5|}{\alpha}})]\mathrm{sgn}(x_5) + d x_5 & x_5 \neq 0 \\ f_a & f_a < f_{st} \;\; \& \;\; x_5 = 0 \\ f_{st} & f_a \geq f_{st} \;\; \& \;\; x_5 = 0 \end{cases} \tag{2.13}$$

correspondingly, the sign function is:

$$\mathrm{sgn}(x_5) = \begin{cases} \frac{x_5}{|x_5|} & x_5 \neq 0 \\ 0 & x_5 = 0 \end{cases} \tag{2.14}$$

In order to apply the discrete EKF algorithm, and to meet the requirement of digital computing, equation (2.12) is discretized using the forward difference method. Equation (2.12) is thus approximated by a discrete nonlinear state space model shown in equation (2.15), in which T is the sampling interval.

$$\begin{cases} x_1(k+1) = Tx_6(k) + x_1(k) \\ x_2(k+1) = \begin{cases} \frac{T\beta}{V_1(x_4(k))}[C_d w x_1(k)\sqrt{\frac{2}{\rho}(p_s - x_2(k))} - Ax_5(k)] + x_2(k) & x_1(k) > 0 \\ \frac{T\beta}{V_1(x_4(k))}[C_d w x_1(k)\sqrt{\frac{2}{\rho}(x_2(k) - p_e)} - Ax_5(k)] + x_2(k) & x_1(k) \le 0 \end{cases} \\ x_3(k+1) = \begin{cases} \frac{T\beta}{V_2(x_4(k))}[-C_d w x_1(k)\sqrt{\frac{2}{\rho}(x_3(k) - p_e)} + Ax_5(k)] + x_3(k) & x_1(k) > 0 \\ \frac{T\beta}{V_2(x_4(k))}[-C_d w x_1(k)\sqrt{\frac{2}{\rho}(p_s - x_3(k))} + Ax_5(k)] + x_3(k) & x_1(k) \le 0 \end{cases} \\ x_4(k+1) = Tx_5(k) + x_4(k) \\ x_5(k+1) = \frac{T}{m_a}(Ax_2(k) - Ax_3(k) - F_c(x_5(k))) + x_5(k) \\ x_6(k+1) = T[-2d_m\omega_n x_6(k) - \omega_n^2 x_1(k) + k_{sp}\omega_n^2 u(k+1)] + x_6(k) \end{cases} \tag{2.15}$$

Again, the actuator friction is presented by the following equations:

$$F_c(x_5(k)) = \begin{cases} [f_{st} - (f_{st} - f_{sl})(1 - e^{-\frac{|x_5(k)|}{\alpha}})]\mathrm{sgn}(x_5(k)) & \\ +dx_5(k) & |x_5(k)| > v_o \\ f_a & f_a < f_{st} \ \& \ |x_5(k)| \le v_o \\ f_{st} & f_a \ge f_{st} \ \& \ |x_5(k)| \le v_o \end{cases} \tag{2.16}$$

where v_o is the threshold for zero in numerical computation and the sign function is:

$$\mathrm{sgn}(x_5(k)) = \begin{cases} \frac{x_5(k)}{|x_5(k)|} & |x_5(k)| > v_o \\ 0 & |x_5(k)| \le v_o \end{cases} \tag{2.17}$$

The actual system parameters applied in the state space model are listed in Table 2.1. The parameters related to the structure of the test rig are obtained from the

product specifications of the actuator, the servovalve and the power unit. The value of bulk modulus, β, reported in this table is taken from Merrit (1967). The friction model parameters are results based on a series of experiments for identifying the friction model. This procedure is shown in Chapter 3. The determination of sampling time is also based on simulation and experimental results which will be elaborated in following chapters.

Table 2.1: Hydraulic test station parameters

Parameter	Value	Parameter	Value
A (m^2)	6.33×10^{-4}	k_{sp} (V/m)	2.794×10^{-5}
m_a (kg)	10.0	ω_n (rad/s)	200.0π
X_{min} (m)	0	d_m	0.7
X_{max} (m)	0.6069	V_1^0 (m^3)	2.14×10^{-5}
d (N·s/m)	350	V_2^0 (m^3)	2.14×10^{-5}
C_d	2.915×10^{-2}	ρ (kg/m^3)	847.15
β (Pa)	6.89×10^8	v_o(m/s)	0.001
f_{st} (N)	2.4×10^3	w (m^2/m)	2.075×10^{-2}
f_{sl} (N)	1.1×10^3	T (s)	0.001
α (m/s)	0.04		

Chapter 3

Model Validation

In this Chapter, simulations and tests are carried out to validate the state space model developed in Chapter 2. Friction model parameters are identified through experiments prior to the simulation to obtain an accurate friction model. Two types of signals, sinusoidal and varying frequency inputs, are applied in the validation. To be specific, the input signals are applied to both the actual system and the simulation program in open-loop mode, then the actual system measurements and the simulation results are compared. In this validation, the simulation program adequately represents the actual system.

3.1 Identification of Friction Parameters

Accurate friction model parameters are necessary for the system model. Experiments have been carried out on the test rig in two steps: (1) obtaining the plot of taking-off actuation force vs velocity and (2), obtaining the average actuation force under different velocities. The actuator works in unloaded mode in both scenarios. To be specific, step (1) records the actuation force when the actuator starts to move. This is achieved by slowly increasing the input of the servovalve. In the experiments,

this increase is controlled by the PC. Peaks of the actuation force are observed even without noticeable change on the velocity curves. The acceleration force can thus be ignored and the maximum actuation forces are recorded as the stiction. Ten locations are sampled evenly along entire length of the stroke and the average value is adopted. In step (2), specific constant velocities are maintained and the average actuation force is obtained. The average force is recorded as the slip friction at corresponding velocity.

With experiments in different velocities, the Force-vs-Velocity curve is obtained. Figure 3.1 shows the experimental values for f_{st} and f_{sl} are around 2.4kN and 1.1kN, respectively, while the damping ratio, d, is around 250$\sim$ 360 N·s/m. The factor, α, is chosen as 0.04 m/s according to the actual measurements. The velocity-dependent friction model is also shown in Figure 3.1. After these parameters determined, the simulation program outputs match the actual system measurements.

3.2 Validation of State Space Model

The state space model is validated by comparing the simulated and the measured states given the same input signals. With the same input sequence, the simulation program and the actual actuator are supposed to produce similar state trajectories. Simulations shown in this section use two types of input signals: sinusoidal inputs and varying frequency sinusoidal inputs. The actuator typically works with low frequency region. Therefore, the varying frequency inputs reveal the actuator's working bandwidth.

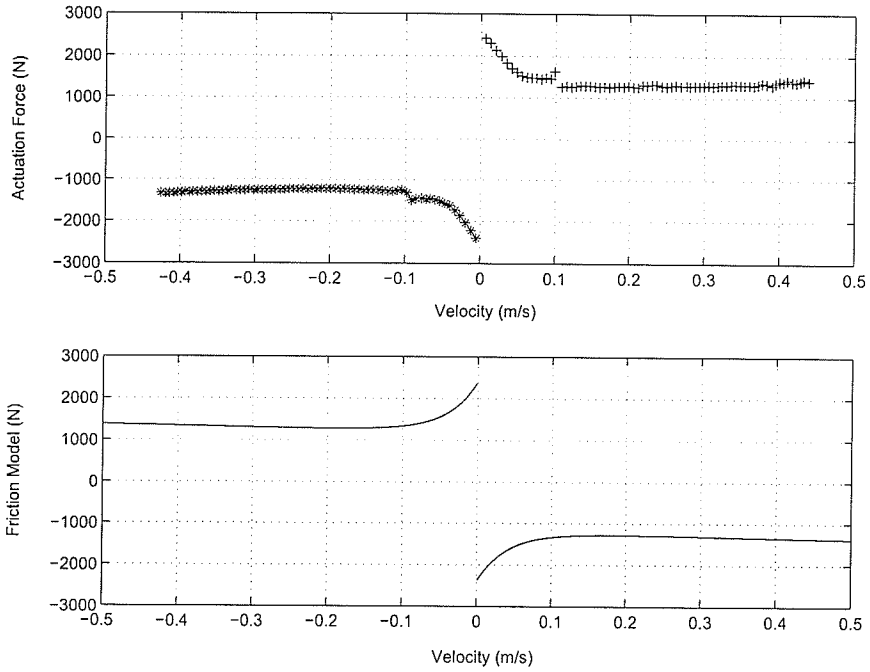

Figure 3.1: Experimental curves of actuator friction.

3.2.1 Sinusoidal Inputs

The sinusoidal signal, $u = 3.0 \sin(2\pi t + 0.1)$ volts, is applied as the input for the servovalve. The test rig and the simulation both run for 10 seconds. Results are shown in Figures 3.2 to 3.6, which are the trajectories of the actuator displacement, x_a, the chamber pressures p_1 and p_2 and the spool displacement, x_{sp}.

From Figure 3.2, it can be seen that the simulation program successfully represents the actuator displacement. The simulated and the measured displacements are so close to each other that it is difficult to distinguish them in the plot. An upward shifting is observed on the plot. This shift indicates the actuator is drifting towards one side of the cylinder during the movement. This is due to asymmetry of the

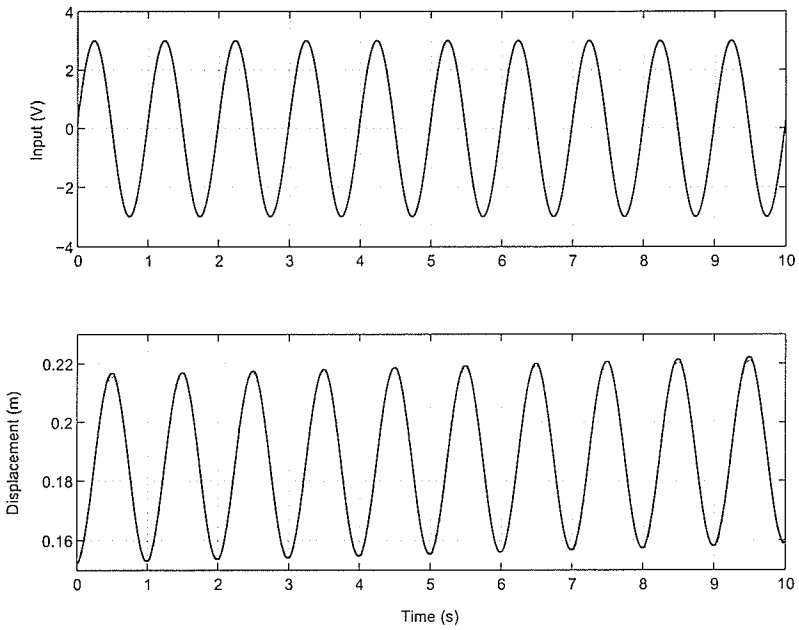

Figure 3.2: Servovalve inputs, measured and simulated actuator displacements (measured and simulated displacements overlap).

extending friction and the retraction friction, as well as the tiny spool drift in the servovalve. By adjusting the friction model, this drift can be successfully simulated.

Figure 3.3 shows detailed trajectories of the measured and simulated actuator displacement and corresponding simulation error. The range of the simulation error is within 2×10^{-3} m with an average of 2.8×10^{-4} m. Compared to the amplitude of the movement, this error can be ignored. The comparison between the measurement and the simulation of chamber pressures is shown in Figures 3.4 and 3.5. The figures show that the simulation data are close to the actual chamber pressures and the errors are within the range of 10^6 Pa. Average values of the pressure errors at chambers 1 and 2 are 1.8×10^5 Pa and 1.1×10^5 Pa. These errors are within 10% of the actual measurements and are considered acceptable. In EKF modeling, these errors are

classified as modeling uncertainties which are represented by process noises.

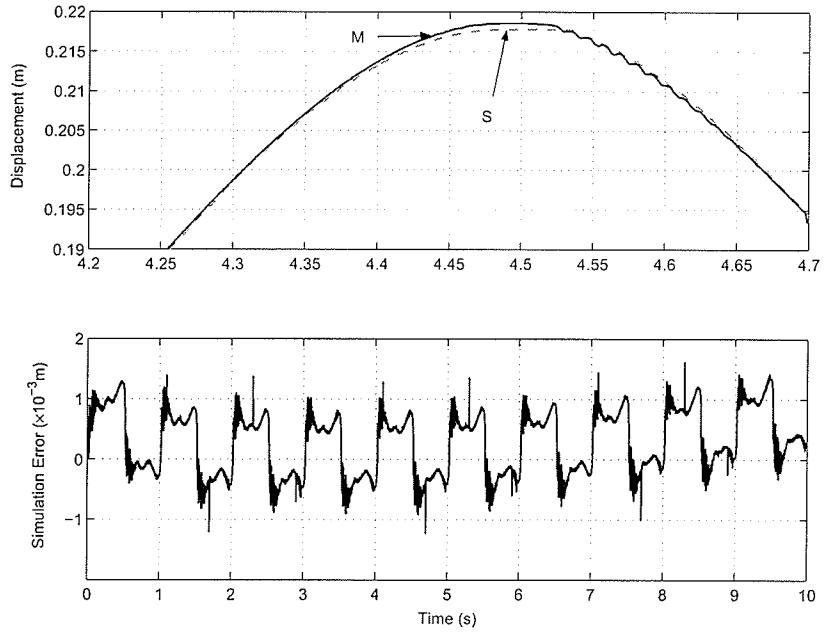

Figure 3.3: Closeup plot of the measured (M) and simulated (S) actuator displacements, and the simulation error.

The displacement of servovalve spool is shown in Figure 3.6. By carefully investigating the figure, it is seen that a bias exists in the measurement curve. This bias is caused by the imprecision of the servovalve and can be improved by recalibrating the servovalve. The average of this bias is -9.8×10^{-6} m, i.e. 10% of the actual amplitude of the spool displacement.

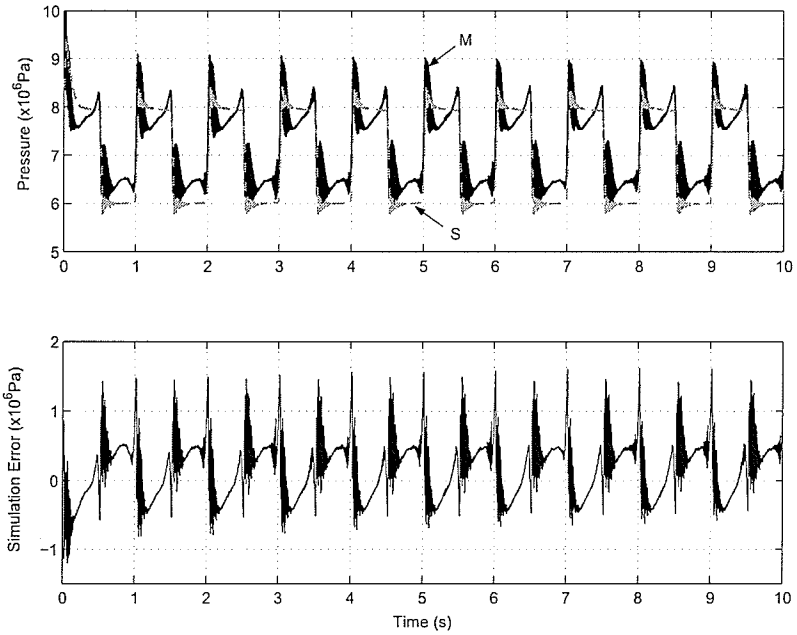

Figure 3.4: Measured (M) and simulated (S) pressure at chamber 1, and simulation error.

3.2.2 Varying Frequency Inputs

To further test the system model in frequency domain, specially designed varying frequency inputs are applied. With the input $3.0\sin(\pi(1+\frac{t}{4})t)$ volts, the actuator runs for 40 seconds so that the frequency of the input signals range from 0.5~10.5Hz, which covers the bandwidth of actuator operation. Test results are shown in Figures 3.7 to 3.11. Figures 3.7 and 3.8 show that the simulated actuator displacements matches the actual measurements with an error range of 4×10^{-3} m. Simulation results for the chamber pressures are shown in Figures 3.9 and 3.10, in which the average errors are 5.6×10^3 Pa and -2.4×10^5 Pa at chamber 1 and 2.

Simulation result for the spool displacement is shown in Figure 3.11, in which it can be observed that the simulation error of the spool displacement increases when

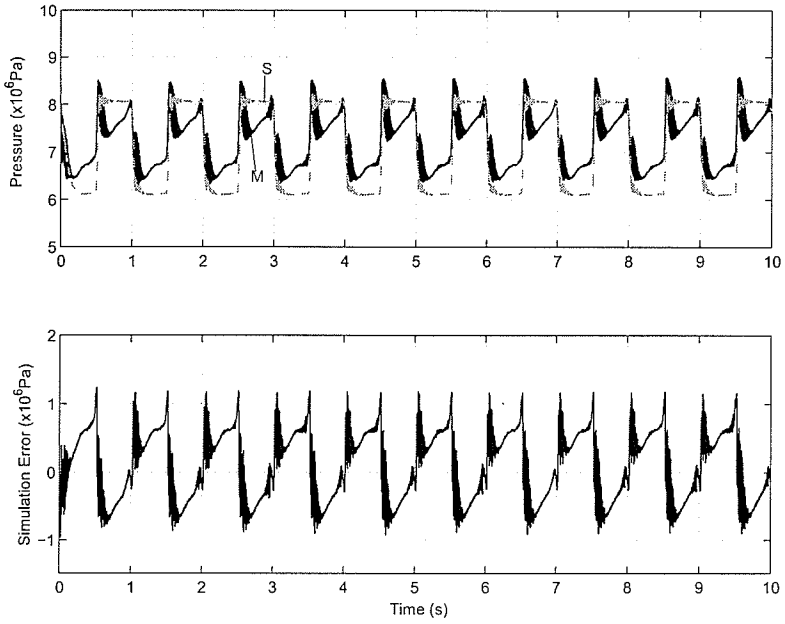

Figure 3.5: Measured (M) and simulated (S) pressure at chamber 2, and simulation error.

the frequency of the input signal increases. This indicates the model is not sufficiently reflecting the actual system characteristics in high frequency region. However, this error is acceptable within the normal range of operating frequency.

With the test shown above, it can be concluded that the developed state space model can effectively represent the actual test rig, though the simulation errors are inevitable and some of them have to be seriously considered when constructing the process noise covariance matrices in later sections.

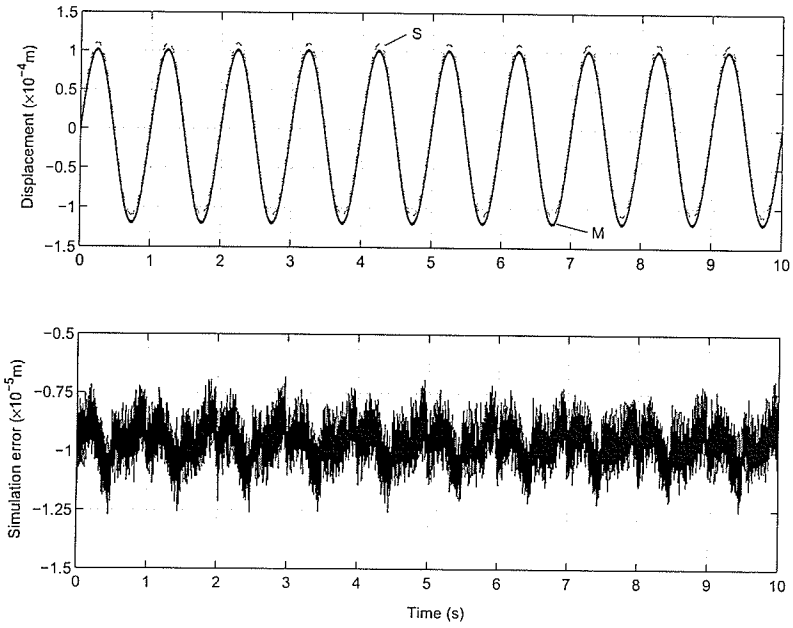

Figure 3.6: Measured (M) and simulated (S) displacements of the servovalve spool, and simulation error.

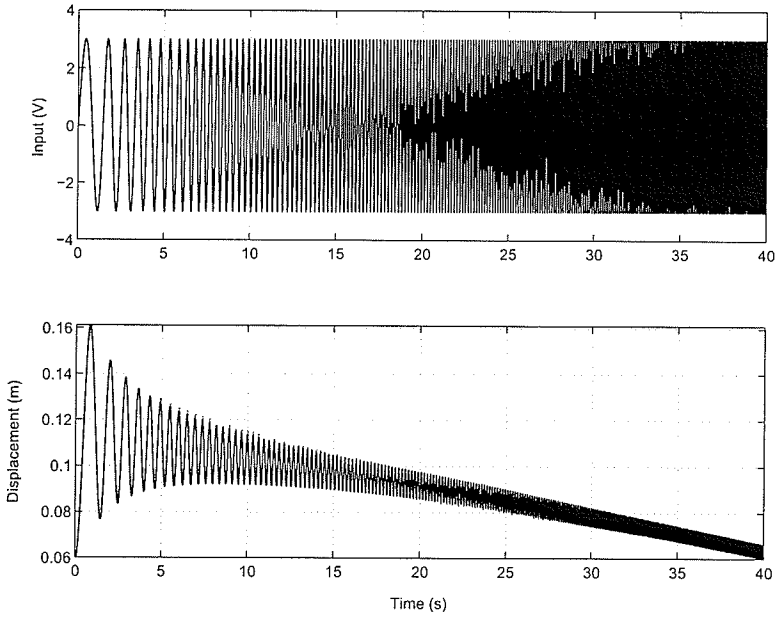

Figure 3.7: Servovalve input signal, measured and overlapped simulated actuator displacements.

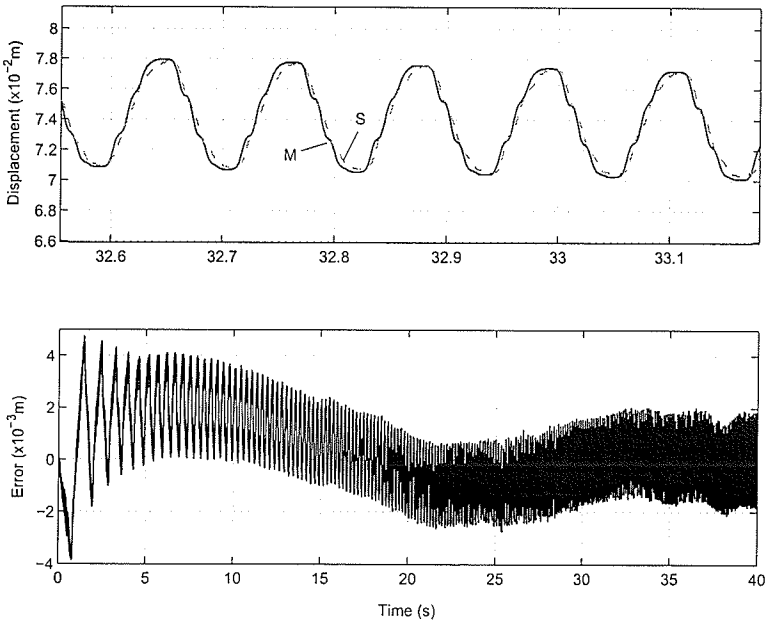

Figure 3.8: Closeup plot of measured (M) and simulated (S) actuator displacements, and simulation error.

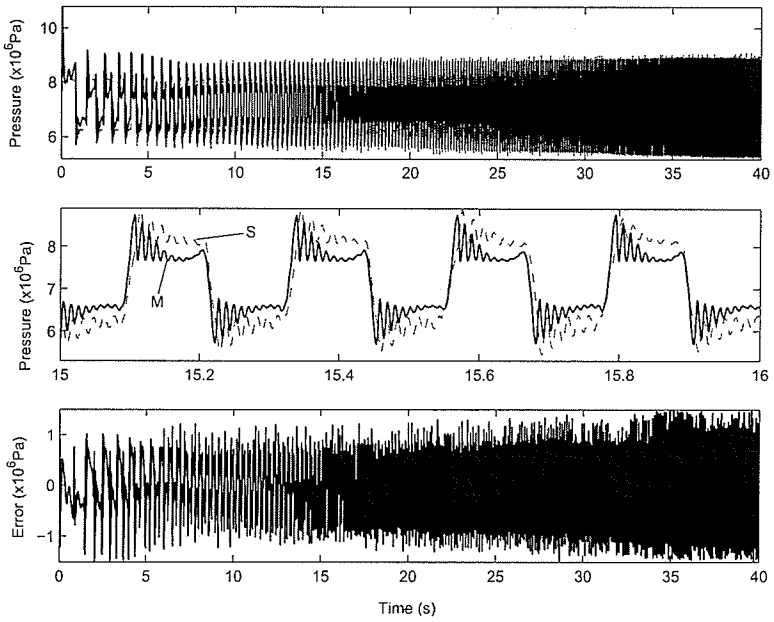

Figure 3.9: Complete and closeup plots of measured (M) and simulated (S) pressure at chamber 1, and simulation error.

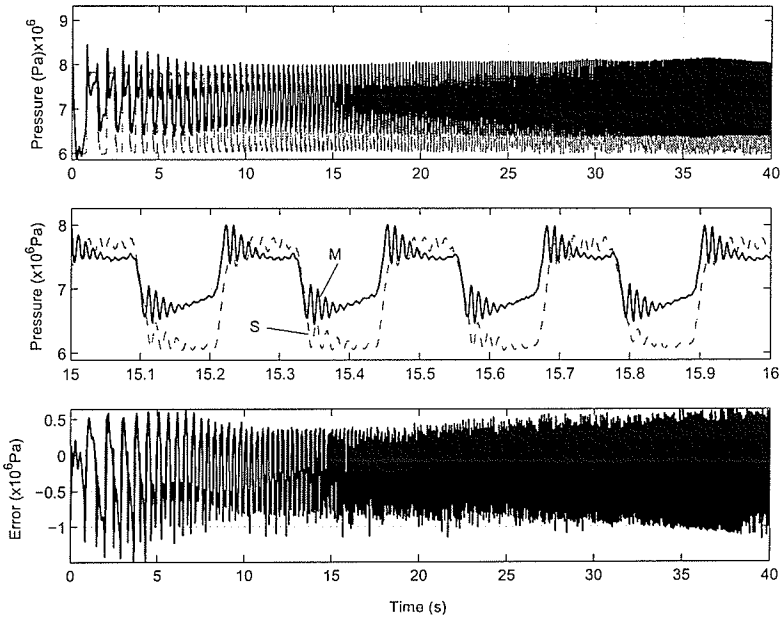

Figure 3.10: Complete and closeup plots of measured (M) and simulated (S) pressure at chamber 2, and simulation error.

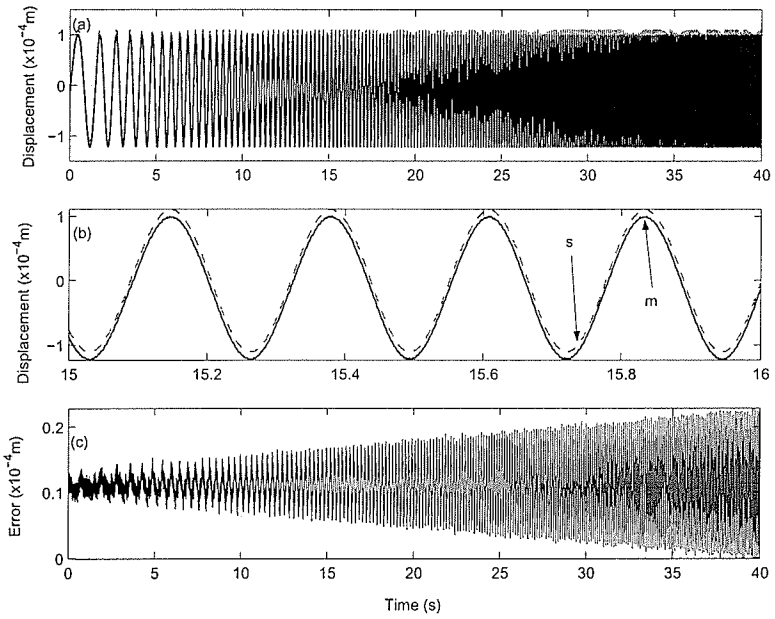

Figure 3.11: Complete and closeup plots of measured (M) and simulated (S) displacements of the servovalve spool, and simulation error.

Chapter 4

Development of Fault Detection and Isolation Scheme Based on Kalman Filter

Kalman filter is named after its inventor, Rudolf Emil Kalman (born May 19, 1930). This mathematical technique is now widely used in control systems and avionics to extract a signal from a series of incomplete and noisy measurements. In 1960, R.E. Kalman (1960) published his famous paper describing a recursive solution to the discrete-data linear filtering problem. Since that time, due in large part to advances in digital computing, the Kalman filter has been the subject of extensive research and application, particularly in the area of autonomous or assisted navigation.

The basic Kalman filtering algorithm is derived applying stochastic process and probability theory to linear problems. It provides a general way to statistically estimate the states of a linear dynamic system if the state space model of the system is known. The concept of extended Kalman filter (EKF) is developed later to further expand this algorithm to time-varying and even nonlinear systems. EKF continually linearizes the model of the system at each step around the *a posteriori* estimate of the state vector that is obtained at last sampling time and computes the *a priori*

estimate of the state vector for current sampling time. Corrections to this *a priori* estimate are then calculated using new measurements to update the *a priori* estimate to the *a posteriori* estimate of system states at current sampling time.

4.1 Basic Kalman Filter

First consider a linear dynamic system represented in the form of a linear state space difference equation.

$$\mathbf{x}_k = \mathbf{A}\mathbf{x}_{k-1} + \mathbf{B}\mathbf{u}_k + \mathbf{W}\mathbf{w}_{k-1} \tag{4.1}$$

where $\mathbf{x}_k$ is the system state vector of dimension n. Vector $\mathbf{u}_k$ is the input vector of dimension r. $\mathbf{A}$ is the $n \times n$ transition matrix; $\mathbf{B}$ is the $n \times r$ input matrix; $\mathbf{W}$ is the $n \times s$ process noise matrix and vectors $\mathbf{w}_k$ represents the process noise that has a dimension of s. The available measurements are modeled by the following equation:

$$\mathbf{z}_k = \mathbf{H}\mathbf{x}_k + \mathbf{v}_k \tag{4.2}$$

in which, $\mathbf{z}_k$ is the measurement vector of dimension m. $\mathbf{H}$ is the $m \times n$ measurement matrix, and $\mathbf{v}_k$ is the measurement noise vector of dimension m. The process and measurement noises are assumed to be white, Gaussian and independent of each other. With these assumptions, the noises can be regarded as stationary stochastic processes that have normal probability distributions with mean values equal to $\mathbf{0}$ and covariance matrices $\mathbf{Q}$ and $\mathbf{R}$; i.e., distributions $\mathbf{f}(\mathbf{w}) \sim N(0, \mathbf{Q})$ and $\mathbf{f}(\mathbf{v}) \sim N(0, \mathbf{R})$, where the notation N represents normal distribution.

At current sampling time, k, the *a posteriori* estimates of the system states at sampling time $k-1$ are available and can be denoted as $\hat{\mathbf{x}}_{k-1}^{+}$. The purpose of Kalman

filter is to obtain the *a posteriori* estimate, $\hat{\mathbf{x}}_k^+$, for current sampling time using the information of $\hat{\mathbf{x}}_{k-1}^+$ and current measurement $\mathbf{z}_k$. Since the system is regarded as a stochastic process, the system states $\{\mathbf{x}_i | i = 0, 1, \quad , k\}$ are random variables and their probability distributions are conditional with the existence of measurement sequence $\{\mathbf{z}_1 \quad \mathbf{z}_i\}$. If we assume this conditional distribution to be Gaussian, the expectation of $\mathbf{x}_k$ is the optimal estimate, i.e. $\hat{\mathbf{x}}_k^+ = E[\mathbf{x}_k | \mathbf{z}_1 \quad \mathbf{z}_k]$, where the operator $E[\cdot]$ denotes the expectation of a random variable. Correspondingly, the conditional covariance matrix is given as $\hat{\mathbf{P}}_k^+ = E[(\mathbf{x}_k - \hat{\mathbf{x}}_k^+)(\mathbf{x}_k - \hat{\mathbf{x}}_k^+)^{\mathrm{T}} | \mathbf{z}_1 \quad \mathbf{z}_k]$. The conditional probability density is:

$$f(\mathbf{x}_k | \mathbf{z}_1 \quad \mathbf{z}_k) = \frac{1}{\sqrt{(2\pi)^n |\hat{\mathbf{P}}_k^+|}} e^{[(\mathbf{x}_k - \hat{\mathbf{x}}_k^+)(\hat{\mathbf{P}}_k^+)^{-1}(\mathbf{x}_k - \hat{\mathbf{x}}_k^+)^{\mathrm{T}}]} \tag{4.3}$$

Define the *a priori* estimate at current sampling time as $\hat{\mathbf{x}}_k^-$. It can be obtained as the optimal estimate at the kth sampling time based on the *a posteriori* estimate at the $(k-1)$th sampling time, which is $\hat{\mathbf{x}}_k^- = \mathbf{A}\hat{\mathbf{x}}_{k-1}^+ + \mathbf{B}\mathbf{u}_{k-1}$. The conditional covariance matrix is given as $\mathbf{P}_k^- = E[(\mathbf{x}_k - \hat{\mathbf{x}}_k^-)(\mathbf{x}_k - \hat{\mathbf{x}}_k^-)^{\mathrm{T}} | \mathbf{z}_1 \quad \mathbf{z}_{k-1}]$. It can be proved (Maybeck, 1979) that the following relations exist providing aforementioned state vector and noise distributions are applicable.

$$\hat{\mathbf{x}}_k^+ = \hat{\mathbf{x}}_k^- + \mathbf{K}_k(\mathbf{z}_k - \mathbf{H}\hat{\mathbf{x}}_k^-) \tag{4.4}$$

$$\mathbf{P}_k^+ = (\mathbf{I} - \mathbf{K}_k\mathbf{H})\mathbf{P}_k^- \tag{4.5}$$

$$\mathbf{P}_k^- = \mathbf{A}\mathbf{P}_{k-1}^+\mathbf{A}^{\mathrm{T}} + \mathbf{W}\mathbf{Q}\mathbf{W}^{\mathrm{T}} \tag{4.6}$$

where $\mathbf{K}_k$ is defined as the Kalman gain, and is given by the following equation:

$$\mathbf{K}_k = \mathbf{P}_k^-\mathbf{H}^{\mathrm{T}}(\mathbf{H}\mathbf{P}_k^-\mathbf{H}^{\mathrm{T}} + \mathbf{R})^{-1} \tag{4.7}$$

Equations (4.4) to (4.7) present an implementation for linear Kalman filter. From these equations the Kalman filter algorithm can be described as two stages of computation: (a) the filter predicts the system state at current sampling time with the information of previous inputs and measurements (*a priori*); (b) the prediction of the system state is corrected using the information of measurements at current sampling time, and an adjustable Kalman gain (*a posteriori*):

Stage 1: time updating (prediction):

$$\begin{cases} \hat{\mathbf{x}}_k^- = \mathbf{A}\hat{\mathbf{x}}_{k-1}^+ + \mathbf{B}\mathbf{u}_k \\ \mathbf{P}_k^- = \mathbf{A}\mathbf{P}_{k-1}^+\mathbf{A}^{\mathrm{T}} + \mathbf{W}\mathbf{Q}\mathbf{W}^{\mathrm{T}} \end{cases} \tag{4.8}$$

Stage 2: measurements updating (correction):

$$\begin{cases} \mathbf{K}_k = \mathbf{P}_k^-\mathbf{H}^{\mathrm{T}}(\mathbf{H}\mathbf{P}_k^-\mathbf{H}^{\mathrm{T}} + \mathbf{R})^{-1} \\ \hat{\mathbf{x}}_k^+ = \hat{\mathbf{x}}_k^- + \mathbf{K}_k(\mathbf{z}_k - \mathbf{H}\hat{\mathbf{x}}_k^-) \\ \mathbf{P}_k^+ = (\mathbf{I} - \mathbf{K}_k\mathbf{H})\mathbf{P}_k^- \end{cases} \tag{4.9}$$

This algorithm adopts a recursive way to propagate the *a posteriori* estimates following the evolution of the actual system state.

4.2 Extended Kalman Filter

Basic Kalman filter gives a general way for estimating states of a linear stochastic difference equation. For time-varying and nonlinear systems, however, a Kalman filter that linearizes the model of an actual system around the current mean and covariance is employed. This is referred to as the algorithm of extended Kalman filter (EKF). The basic algorithm for EKF is similar to those of Kalman filter. Consider a nonlinear system represented by the following stochastic difference equation (Welch

and Bishop, 2001)(Jazwinski, 1970):

$$\begin{cases} \mathbf{x}_k = \mathbf{f}(\mathbf{x}_{k-1}, \mathbf{u}_k, \mathbf{w}_{k-1}) \\ \mathbf{z}_k = \mathbf{h}(\mathbf{x}_k, \mathbf{v}_k) \end{cases} \tag{4.10}$$

where $\mathbf{f}(\cdot)$ and $\mathbf{h}(\cdot)$ are the nonlinear functions describing the system state vector, $\mathbf{x}_k$, and the measurement vector, $\mathbf{z}_k$. Vector $\mathbf{u}_k$ is the input vector of dimension r. The process noise and measurement noise vectors $\mathbf{w}_k$ and $\mathbf{v}_k$ are s-vector and m-vector as defined before. The linearized representation of this nonlinear system is

$$\begin{cases} \mathbf{x}_k \approx \hat{\mathbf{x}}_k^- + \mathbf{A}(\mathbf{x}_{k-1} - \hat{\mathbf{x}}_{k-1}^+) + \mathbf{W}\mathbf{w}_{k-1} \\ \mathbf{z}_k \approx \hat{\mathbf{z}}_k + \mathbf{H}(\mathbf{x}_k - \hat{\mathbf{x}}_k^-) + \mathbf{V}\mathbf{v}_k \end{cases} \tag{4.11}$$

where $\hat{\mathbf{x}}_k^-$ is the *a priori* estimate of system state or in other words, the prediction of the system states at current sampling time given the information of previous estimation and measurements; and $\hat{\mathbf{z}}_k$ is the approximation, calculated by the following equations

$$\begin{cases} \hat{\mathbf{x}}_k^- = \mathbf{f}(\hat{\mathbf{x}}_{k-1}^+, \mathbf{u}_k, \mathbf{0}) \\ \hat{\mathbf{z}}_k = \mathbf{h}(\hat{\mathbf{x}}_k^-, \mathbf{0}) \end{cases} \tag{4.12}$$

$\mathbf{A}$, $\mathbf{H}$, $\mathbf{W}$, and $\mathbf{V}$ are Jacobian matrices of the linearized model updated at each sampling time. Suppose the current instant is sampling time k, the matrices are obtained by

$$\mathbf{A}_{k[i,j]} = \left.\frac{\partial f_{[i]}}{\partial x_{[j]}}\right|_{(\hat{\mathbf{x}}_{i-1}^+, \mathbf{u}_i, 0)} \tag{4.13}$$

$$\mathbf{H}_{k[i,j]} = \left.\frac{\partial h_{[i]}}{\partial x_{[j]}}\right|_{(\hat{\mathbf{x}}_i^-, 0)} \tag{4.14}$$

$$\mathbf{W}_{k[i,j]} = \left.\frac{\partial f_{[i]}}{\partial w_{[j]}}\right|_{(\hat{\mathbf{x}}_{i-1}^+, \mathbf{u}_i, 0)} \tag{4.15}$$

$$\mathbf{V}_{k[i,j]} = \left.\frac{\partial h_{[i]}}{\partial v_{[j]}}\right|_{(\hat{\mathbf{x}}_i^-,0)} \tag{4.16}$$

With the linearization above, the complete EKF algorithm can also be grouped into two stages as shown in the following:

Stage 1: time updating equations (prediction):

$$\begin{cases} \hat{\mathbf{x}}_k^- = \mathbf{f}(\hat{\mathbf{x}}_{k-1}^+, \mathbf{u}_k, \mathbf{0}) \\ \mathbf{P}_k^- = \mathbf{A}\mathbf{P}_{k-1}^+\mathbf{A}^{\mathrm{T}} + \mathbf{W}_k\mathbf{Q}_{k-1}\mathbf{W}_k^{\mathrm{T}} \end{cases} \tag{4.17}$$

Stage 2: measurements updating equations (correction):

$$\begin{cases} \mathbf{K}_k = \mathbf{P}_k^-\mathbf{H}^{\mathrm{T}}(\mathbf{H}\mathbf{P}_k^-\mathbf{H}^{\mathrm{T}} + \mathbf{V}_k\mathbf{R}_k\mathbf{V}_k^{\mathrm{T}})^{-1} \\ \hat{\mathbf{x}}_k^+ = \hat{\mathbf{x}}_k^- + \mathbf{K}_k\big[\mathbf{z}_k - \mathbf{h}(\hat{\mathbf{x}}_k^-, \mathbf{0})\big] \\ \mathbf{P}_k^+ = (\mathbf{I} - \mathbf{K}_k\mathbf{H})\mathbf{P}_k^- \end{cases} \tag{4.18}$$

As seen, the updating equations of EKF are similar to those of the standard KF. However in EKF, the Jacobian matrices are updated at each step, k, due to the requirement of continual linearization. The measurement and the process noise covariance matrices are also considered to be changing at each step. However, similar to those in the derivation of basic Kalman filter, the noise covariance matrices can be constant if the noises are stationary processes that are white and Gaussian. In this research, the covariance matrices were estimated prior to the experiment.

4.3 Application to Hydraulic Actuation Systems

To apply EKF algorithm to the state space model represented by equation (2.15), it is necessary to determine the elements of Jacobian matrices **A**, **W**, **H** and **V**. Given the sampling time T, the elements of matrix **A** can be obtained from equation (4.11)

as

$$\mathbf{A} = \frac{\partial \mathbf{f}}{\partial \mathbf{x}} = \left[\frac{\partial f_1}{\partial \mathbf{x}}, \frac{\partial f_2}{\partial \mathbf{x}}, \frac{\partial f_3}{\partial \mathbf{x}}, \frac{\partial f_4}{\partial \mathbf{x}}, \frac{\partial f_5}{\partial \mathbf{x}}, \frac{\partial f_6}{\partial \mathbf{x}}\right]^{\mathrm{T}} \tag{4.19}$$

where

$$\frac{\partial f_1}{\partial \mathbf{x}} = [1, \quad 0, \quad 0, \quad 0, \quad 0, \quad T]$$

$$\frac{\partial f_2}{\partial \mathbf{x}} = \begin{bmatrix} \frac{T\beta}{V_1(x_4(k))} C_d w x_1(k) \sqrt{\frac{2}{\rho}(p_s - x_2(k))}, \\ 1 + \frac{T\beta}{V_1(x_4(k))} C_d w x_1(k) \Big(\frac{-1}{\rho \sqrt{\frac{2}{\rho}(p_s - x_2(k))}} \Big), \\ 0, \\ -\frac{T\beta}{V_1^2(x_4(k))} \dot{V}_1(x_4(k)) \Big[C_d w x_1(k) \sqrt{\frac{2}{\rho}(p_s - x_2(k))} - A x_5(k) \Big], \\ \frac{T\beta}{V_1(x_4(k))}(-A), \\ 0 \end{bmatrix} \quad x_1(k) > 0$$

$$\frac{\partial f_2}{\partial \mathbf{x}} = \begin{bmatrix} \frac{T\beta}{V_1(x_4(k))} C_d w x_1(k) \sqrt{\frac{2}{\rho}(x_2(k) - p_e)}, \\ 1 + \frac{T\beta}{V_1(x_4(k))} C_d w x_1(k) \Big(\frac{1}{\rho \sqrt{\frac{2}{\rho}(x_2(k) - p_e)}} \Big), \\ 0, \\ -\frac{T\beta}{V_1^2(x_4(k))} \dot{V}_1(x_4(k)) \Big[C_d w x_1(k) \sqrt{\frac{2}{\rho}(x_2(k) - p_e)} - A x_5(k) \Big], \\ \frac{T\beta}{V_1(x_4(k))}(-A), \\ 0 \end{bmatrix} \quad x_1(k) \leq 0$$

$$\frac{\partial f_3}{\partial \mathbf{x}} = \begin{bmatrix} \frac{T\beta}{V_2(x_4(k))} \Big(- C_d w x_1(k) \sqrt{\frac{2}{\rho}(x_3(k) - p_e)} \Big), \\ 0, \\ 1 + \frac{T\beta}{V_2(x_4(k))} \Bigg(- C_d w x_1(k) \Big(\frac{-1}{\rho \sqrt{\frac{2}{\rho}(x_3(k) - p_e)}} \Big) \Bigg), \\ -\frac{T\beta}{V_2^2(x_4(k))} \dot{V}_2(x_4(k)) \Big[- C_d w x_1(k) \sqrt{\frac{2}{\rho}(x_3(k) - p_e)} + A x_5(k) \Big], \\ \frac{T\beta}{V_2(x_4(k))} A, \\ 0 \end{bmatrix} \quad x_1(k) > 0$$

$$\frac{\partial f_3}{\partial \mathbf{x}} = \begin{bmatrix} \frac{T\beta}{V_2(x_4(k))}\Big(- C_d w x_1(k)\sqrt{\frac{2}{\rho}(p_s - x_3(k))}\Big), \\ 0, \\ 1 + \frac{T\beta}{V_2(x_4(k))}\Bigg(- C_d w x_1(k)\Big(\frac{-1}{\rho\sqrt{\frac{2}{\rho}(p_s - x_3(k))}}\Big)\Bigg), \\ -\frac{T\beta}{V_2^2(x_4(k))}\dot{V}_2(x_4(k))\Big[- C_d w x_1(k)\sqrt{\frac{2}{\rho}(p_s - x_3(k))} + A x_5(k)\Big], \\ \frac{T\beta}{V_2(x_4(k))}(A), \\ 0 \end{bmatrix} \quad x_1(k) \leq 0$$

$$\frac{\partial f_4}{\partial \mathbf{x}} = [0, \quad 0, \quad 0, \quad 1, \quad T, \quad 0]$$

$$\frac{\partial f_5}{\partial \mathbf{x}} = [0, \quad \frac{T}{m_a}A, \quad -\frac{T}{m_a}A, \quad 0, \quad \Big(-T\frac{dF_c}{dx_5(k)} + 1\Big), \quad 0]$$

$$\frac{\partial f_6}{\partial \mathbf{x}} = [-\omega_n^2 T, \quad 0, \quad 0, \quad 0, \quad 0, \quad (-2d_m\omega_n T + 1)]$$

$\frac{dF_c}{dx_5(k)}$ is the first order derivative of the friction model with respect to the actuator velocity, $x_5(k)$, and is given in equation (4.20). Since the friction is piecewise continuous, $\frac{dF_c}{dx_5(k)}$ is defined only on the continuous portions of the friction model.

$$\frac{dF_c}{dx_5(k)} = \begin{cases} -\frac{(f_{st} - f_{sl})}{\alpha}e^{-\frac{|x_5(k)|}{\alpha}}\text{sgn}(x_5(k)) + d & |x_5(k)| > v_o \\ 0 & |x_5(k)| \leq v_o \end{cases} \tag{4.20}$$

$\mathbf{H}$ changes when different possible measurement combinations are chosen. If the measurement is the actuator displacement, x, then H is a (1×6) matrix

$$\mathbf{H} = [0 \quad 0 \quad 0 \quad 1 \quad 0 \quad 0] \tag{4.21}$$

If the measurements are p_1 and p_2 then H is a (2×6) matrix as

$$\mathbf{H} = \begin{bmatrix} 0 & 1 & 0 & 0 & 0 & 0 \\ 0 & 0 & 1 & 0 & 0 & 0 \end{bmatrix} \tag{4.22}$$

If the measurements are x_a, p_1 and p_2 then $\mathbf{H}$ is a (3×6) matrix as

$$\mathbf{H} = \begin{bmatrix} 0 & 0 & 0 & 1 & 0 & 0 \\ 0 & 1 & 0 & 0 & 0 & 0 \\ 0 & 0 & 1 & 0 & 0 & 0 \end{bmatrix} \tag{4.23}$$

Assume the noises $w_i\,(i = 1, \quad , 6)$ are independent of each other, the covariance matrices of $\mathbf{W}$ and $\mathbf{V}$ are unity matrices.

4.4 Residual Error Generation and Fault Detection

By applying the EKF estimator to the hydraulic system, a sequence of estimated state vectors, $\{\hat{\mathbf{x}}_i^+ \mid i = 1, \ldots, k\}$, is available. The basic algorithm is to compare at each sampling time, k, the estimated state vector, $\hat{\mathbf{x}}_k^+$, with the measured state vector, $\mathbf{z}_k$, to compute the estimation residual vector, $\mathbf{e}_k$.

$$\mathbf{e}_k = \mathbf{z}_k - \mathbf{H}\hat{\mathbf{x}}_k^+ \tag{4.24}$$

Under normal operating condition, outputs of the EKF estimator should closely converge to the actual system states at each sampling time. However, due to the uncertainties in modeling, the residual errors, $\mathbf{e}_k$, are maintained at relatively low levels but can not be eliminated when the system is healthy. Thus, the residual errors under normal conditions reflect the estimation errors. When a fault occurs, the system's dynamic features change. Theoretically, a discrepancy lies between the faulty system and the EKF estimator which is designed based on the healthy system. Due to this discrepancy, the estimation of the EKF on specific system states diverges from the measured state trajectories. By tracing the variation of the residual errors, a fault

can be detected. Meanwhile, by observing the pattern of the residual errors, different faults can be identified.

Residual errors are further processed after the experiments by applying the moving average method to the error sequences. Extra noises in the residual errors that are caused by system vibration can thus be reduced and the main statistic characteristics are more significant. The moving average of the errors (MAE), e_a, is calculated from $e_a = \frac{\sum_{i=k-n}^{k} e_i}{n}$, where the size of the data window, n, is chosen as 4000 (sampled at 1000Hz) considering the working bandwidth of the actuator.

4.5 Initial Conditions

In the absence of any data at initial time $k = 0$, choices for the initial state vector, $\hat{\mathbf{x}}_0^+$, and the covariance matrix, $\hat{\mathbf{P}}_0^+$, can be accordingly set to the expected values (Haykin, 2001). In practice, $\hat{\mathbf{P}}_0^+$ can be set to a sufficiently positive-definite matrix that is diagonally salient. In this research, $\hat{\mathbf{P}}_0^+$ is set to be a diagonal matrix with $\hat{\mathbf{P}}_0^+[i,i] = 10^4$. The initial vector can be arbitrarily chosen. However, basic physical rules have to be complied with - the initial values of the chamber pressures should be within the range of $[p_e, p_s]$. Therefore, the initial vector applied in this research is $\hat{\mathbf{x}}_0^+ = [\,0\,\text{m},\ 6.8 \times 10^6\,\text{Pa},\ 6.8 \times 10^6\,\text{Pa},\ 0\,\text{m},\ 0\,\text{m/s},\ 0\,\text{m/s}\,]^{\text{T}}$, in which the chamber pressures are reasonably set to be the mean of p_e and p_s.

Chapter 5

Leakage Fault Detection in the Absence of External Load

In this chapter, experiments are carried out on the test rig to investigate the performance of the proposed FDI scheme. Both open-loop and closed-loop configurations are tested in the experiments. In open-loop configuration, only sinusoidal input signals are applied to the test rig. While in closed-loop configuration, which is more practical to industrial applications, both sinusoidal and pseudo-random position references are tested.

The experiments focus on leakage faults in the actuator. Both internal and external leakages, as mentioned in the previous section, are individually set in the experiments. For each leakage fault, two levels of leakage are tested.

The sampling frequency for the experiments is 1000 Hz. This frequency has been tested to be the lowest applicable sampling frequency for EKF to effectively converge to the system model. The actuator displacement, the cylinder pressures at chamber 1 and 2 and the spool displacement are measured online. However, only the measurements of the actuator displacement and the chamber pressures are used as the inputs to EKF. Together with the system input u, the EKF estimator required four inputs.

The process noise covariance matrix, which is determined empirically with sufficient consideration on modeling uncertainties and simulation errors, is shown below:

$$\mathbf{Q} = \begin{bmatrix} 10^{-20} & & & & & \\ & 10^{4} & & & & \\ & & 10^{4} & & & \\ & & & 10^{-6} & & \\ & & & & 10^{-6} & \\ & & & & & 10^{-20} \end{bmatrix}$$

It is assumed that the noise characteristics of different system states are independent of each other. The measurement noise variances are determined as 10^{-4} m for the actuator displacement, and 10^{6} Pa for the chamber pressures, i.e. the matrix $\mathbf{R}$ is given as the following: $\mathbf{R} = diag[\,10^{-4} \quad 10^{6} \quad 10^{6}\,]$. In all the experiments, the actuator displacement, and the chamber pressures are measured; therefore, equation 4.23 is applied.

5.1 Open-Loop Tests

In this section, the sinusoidal inputs, $u = 3.0\sin(\pi t + 0.1)$, are applied to the test rig. In each experiment, the actuator is moved to an initial position prior to the experiment. The purpose of this initial positioning is to prevent the actuator from running out of its stroke. Each experiment lasts for 40 seconds and a fault is manually initiated on the test rig at the $18th$ second. Since the system runs in open-loop configuration, no correction effect is expected when the actuator keeps drifting towards one end due to the leakage on that side. The configuration of the EKF

estimator is shown in Figure 5.1 where it can be seen that the residual errors are direct subtraction of the actual measurements and their estimates.

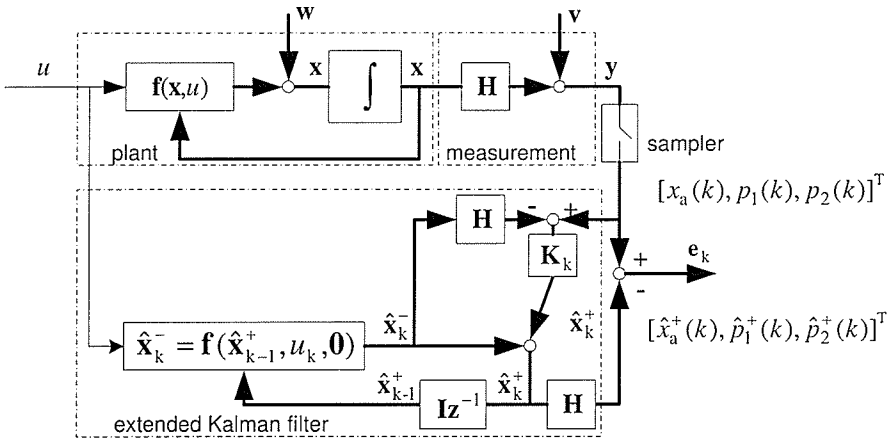

Figure 5.1: Test rig and extended Kalman filter in open-loop configuration.

5.1.1 External Leakage Fault Detection

Leakage Fault at Chamber 1

Experimental results are shown in Figures 5.2 to 5.5. It can be observed that the actuator keeps shifting towards chamber 1 after the leakage occurred. This is obviously due to the leakage at chamber 1 which reduces the power to push the piston towards chamber 2.

Leakages are measured and recorded. Different levels of leakage can be obtained by manually tuning the opening of corresponding needle valve, which are shown in Figure 2.5 and 2.6. In the experiments, two levels of leakage (Low and High) are generated and tested. Since the leakage flow is essentially dependent on the pressure difference, constant leakage flow is impossible for the system. The concept of leakage

coefficient (LC) is introduced to evaluate the leakage and different models have been developed to describe the leakage flow as shown in the following equations.

$$\begin{cases} q_{il} = k_{il}(p_1 - p_2) \\ q_{el1} = k_{el1}(p_1 - p_e) \\ q_{el2} = k_{el2}(p_2 - p_e) \end{cases} \tag{5.1}$$

and

$$\begin{cases} q_{il} = k_{il}\sqrt{(p_1 - p_2)} \\ q_{el1} = k_{el1}\sqrt{(p_1 - p_e)} \\ q_{el2} = k_{el2}\sqrt{(p_2 - p_e)} \end{cases} \tag{5.2}$$

where constants k_{il}, k_{el1} and k_{el2} are the corresponding LCs. Equation (5.1) assumes that the leakages are proportional to the pressure difference while equation (5.2) assumes that the leakages are proportional to the square root of the pressure difference.

From the actual measurement of the leakage flow, k_{el1} is available using equation (5.3) when the linear model, which is represented in equation (5.1), is applied:

$$k_{el1} = \frac{1}{10^3 \cdot 60} \cdot \frac{q_{el1}}{(p_1 - p_e)} = 1.67 \times 10^{-5} \cdot \frac{q_{el1}}{(p_1 - p_e)} \tag{5.3}$$

in which the leakage flow q_{el1} is in liter per minute (l/min) and the chamber pressures are in Pascal (Pa). The leakage and the corresponding LC are shown in Figure 5.6b. However the plot of k_{el1} is still very noisy in Figure 5.6 due to the measurement noise and the oscillation of the system. The mean of the LC with lower leakage is $k_{el1} = 1.59 \times 10^{-12}\,(\mathrm{m}^3/\mathrm{s} \cdot \mathrm{Pa})$ and the standard deviation is $\sigma_{el1} = 3.79 \times 10^{-13}\,(\mathrm{m}^3/\mathrm{s} \cdot \mathrm{Pa})$.

When the square-root model is applied, k_{el1} is obtained using equation (5.4). The mean of the LC with lower leakage is $k_{el1} = 3.87 \times 10^{-9}\,(\mathrm{m}^3/\mathrm{s} \cdot \mathrm{Pa})$ and the standard

deviation is $\sigma_{el1} = 8.03 \times 10^{-10}\,(\mathrm{m}^3/\mathrm{s} \cdot \mathrm{Pa})$.

$$k_{el1} = \frac{1}{10^3 \cdot 60} \cdot \frac{q_{el1}}{\sqrt{(p_1 - p_e)}} = 1.67 \times 10^{-5} \cdot \frac{q_{el1}}{\sqrt{(p_1 - p_e)}} \tag{5.4}$$

The plot of the corresponding LC is shown in Figure 5.6a. It can be seen the LC obtained from the square-root model is slightly less fluctuated than the linear model. However, due to the difference of the models, the two plots are incomparable. An index of indicating how intensive the fluctuation can be defined by comparing the ratio of σ_{el1} and k_{el1} since the mean and the standard deviation from both models are available, as shown in the following equation.

$$\frac{\sigma_{el1}}{k_{el1}} \times 100\% \tag{5.5}$$

For k_{el1}, this index is 23.8% with the linear model and 20.7% with the square-root model. Therefore the square-root model is more applicable for leakage estimation and it will be used for later experimental data in this study.

Referring to Figures 5.4 and 5.5, it can be seen that the chamber pressures change radically when the leakage is set at the $18th$ second. However, the EKF estimator can only closely trace the variation of the pressure at chamber 2. The estimation of the pressure at chamber 1 obviously diverges from the actual measurement. The plots for the moving average of the residual errors show that the residual error of the pressure at chamber 1 increases rapidly and is then stabilized at a higher level, whereas the moving average of the residual error at chamber 2 does not change much even after the leakage is set. This difference clearly indicates the occurrence of the leakage at chamber 1.

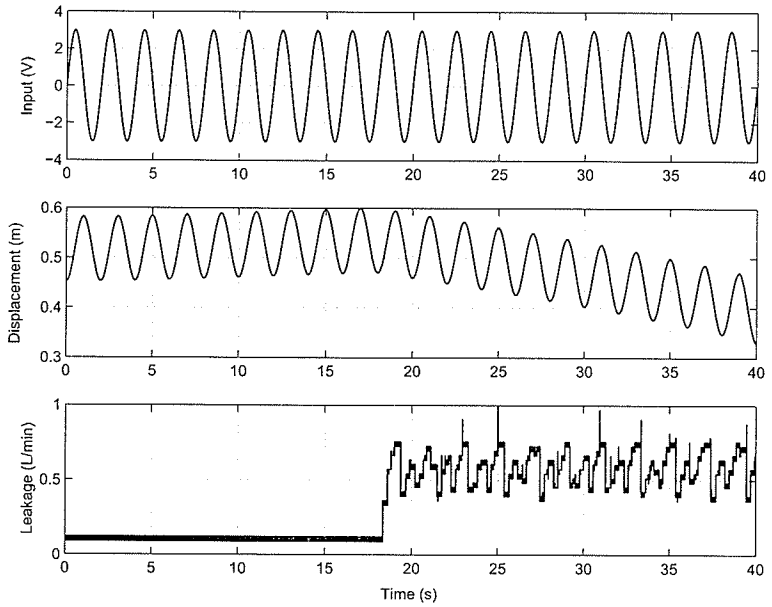

Figure 5.2: Valve input, actuator displacement and leakage at chamber 1.

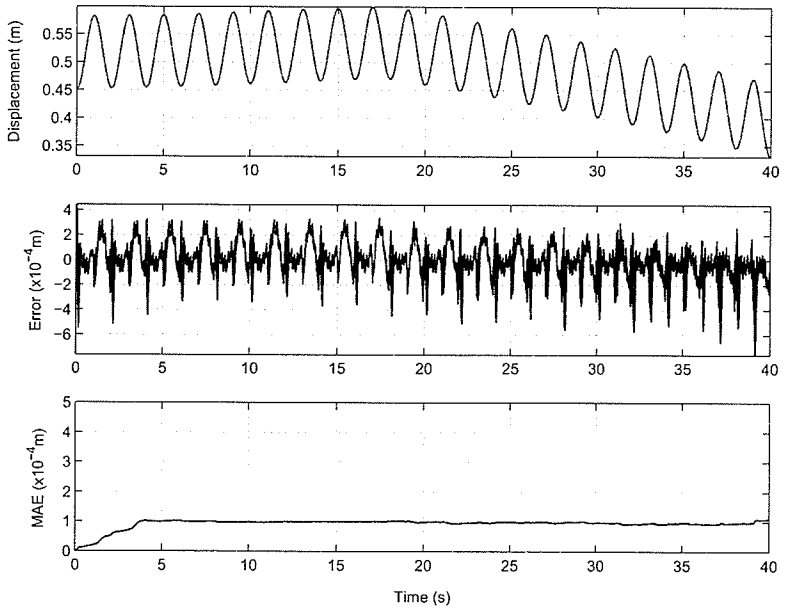

Figure 5.3: Measured and overlapped estimated actuator displacements, residual error, and MAE.

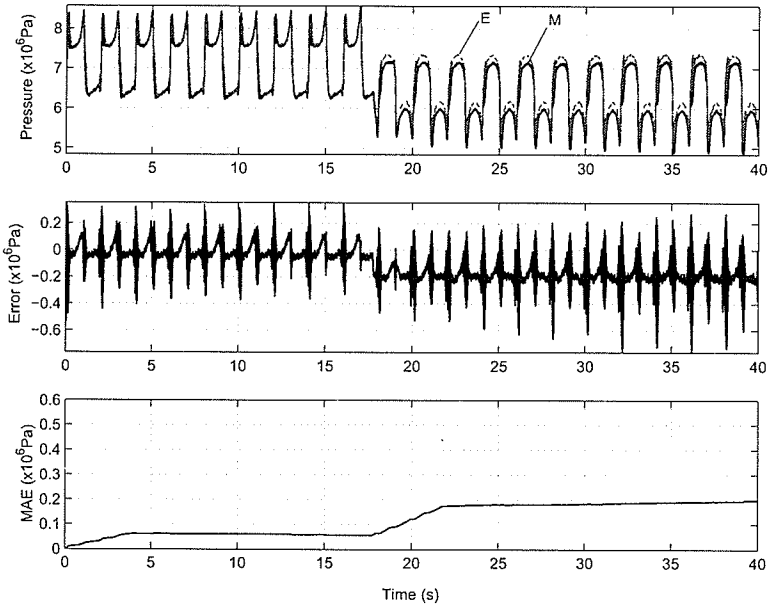

Figure 5.4: Measured (M) and estimated (E) pressures at chamber 1, residual error, and MAE. Estimated pressure follows the measured closely when there is no leakage.

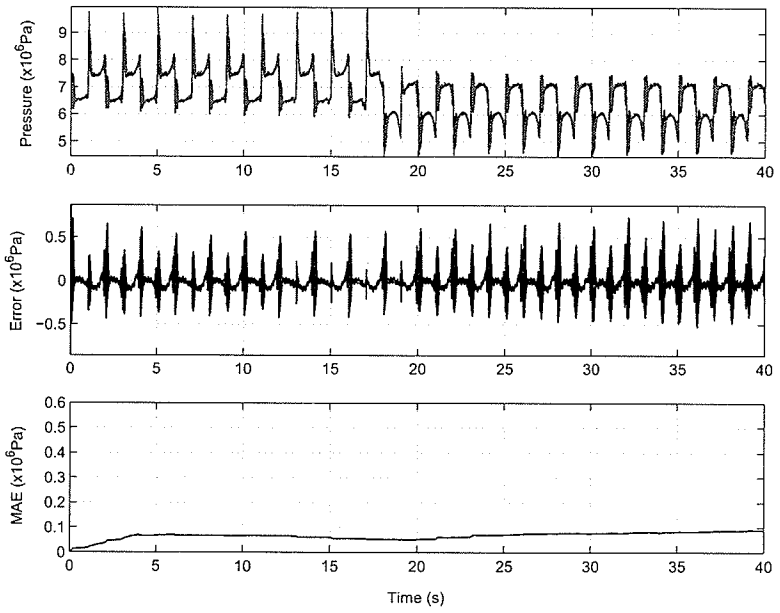

Figure 5.5: Measured and overlapped estimated pressures at chamber 2, residual error and MAE.

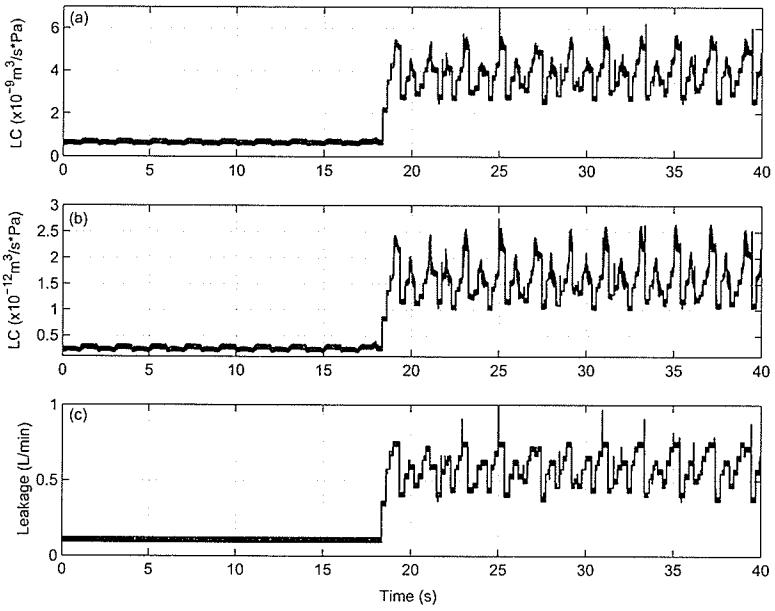

Figure 5.6: Leakage and the leakage coefficient at chamber 1.

Leakage Fault at Chamber 2

Considering the symmetric structure of the actuator, the performance of the proposed FDI scheme with leakage at chamber 2 is expected to be similar to that at chamber 1. Experiments verified this prediction. Figure 5.7 shows the plot of the leakage and corresponding k_{el2} at chamber 2. The mean value of the leakage coefficient is $\bar{k}_{el2} = 4.04 \times 10^{-9}\,(\mathrm{m}^3/\mathrm{s} \cdot \mathrm{Pa})$ and the standard variance is $\sigma_{el1} = 7.03 \times 10^{-10}\,(\mathrm{m}^3/\mathrm{s} \cdot \mathrm{Pa})$. Similar to the calculation of k_{el1} in section 5.1.1, the coefficient k_{el2} is estimated as the following:

$$k_{el2} = \frac{1}{10^3 \cdot 60} \cdot \frac{q_{el2}}{\sqrt{(p_2 - p_e)}} = 1.67 \times 10^{-5} \cdot \frac{q_{el2}}{\sqrt{(p_2 - p_e)}} \tag{5.6}$$

Figures 5.8 to 5.11 show the experimental results related to the low leakage fault at chamber 2. In Figure 5.8, it can be seen that the actuator keeps shifting towards

chamber 2 due to the leakage on the same side. It is also clearly seen from Figures 5.10 and 5.11 that the moving average of the residual error of the pressure at chamber 2 increases from 10^5 to 2×10^5 (Pa) and remains at this level after the leakage is created, while the residual error at chamber 1 does not change significantly even after the fault has occurred. Therefore the EKF estimator clearly identifies the occurrence of chamber leakage faults through the increase of residual error at the faulty chamber.

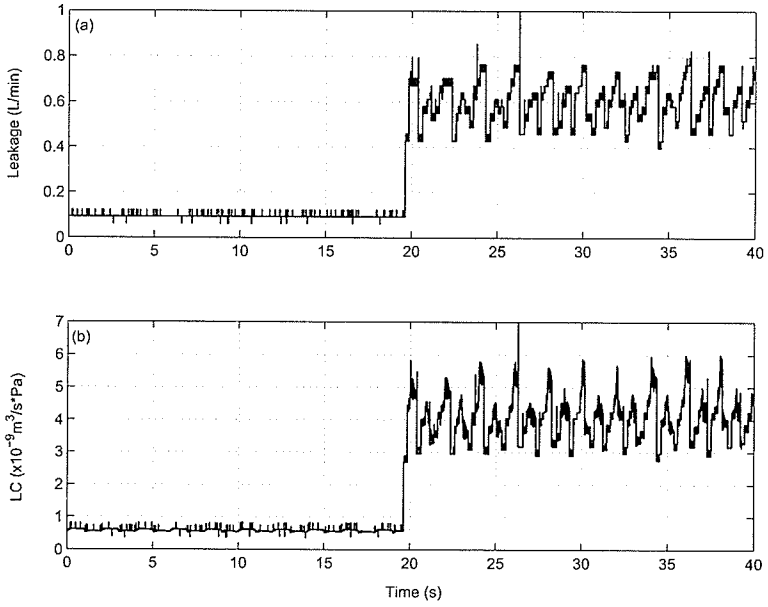

Figure 5.7: Leakage and the leakage coefficient at chamber 2.

5.1.2 Internal Leakage Fault Detection

Different from the external leakage faults at the actuator chambers, the internal leakage occurs on the piston seal. The leakage flow thus moves from higher-pressure side to lower-pressure side of the actuator when the system is running. This leakage is introduced by adjusting the needle valve mounted on the bypass that connects the

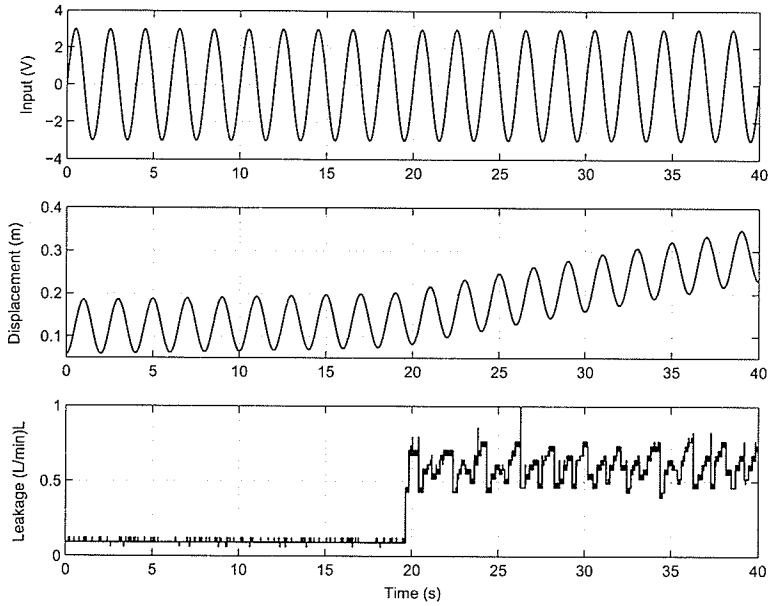

Figure 5.8: Valve input signal, measured actuator displacement and leakage at chamber 2.

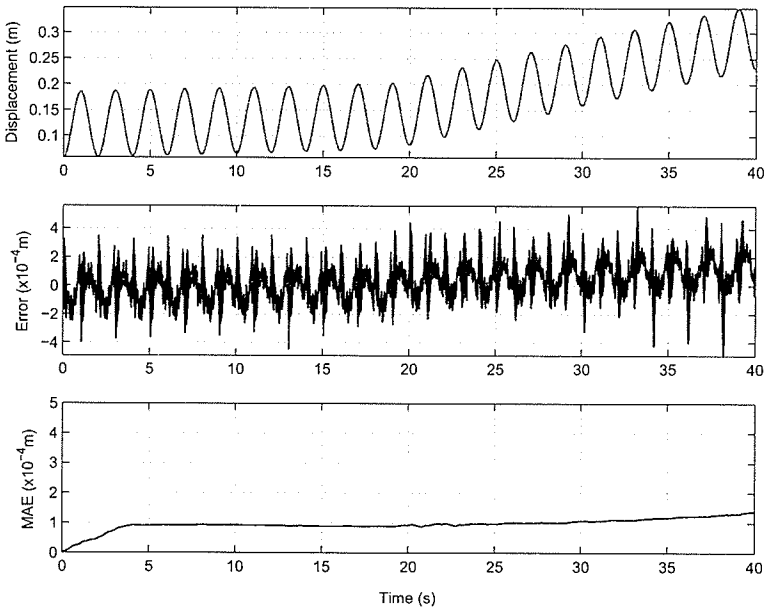

Figure 5.9: Measured and overlapped estimated actuator displacements, residual error and MAE.

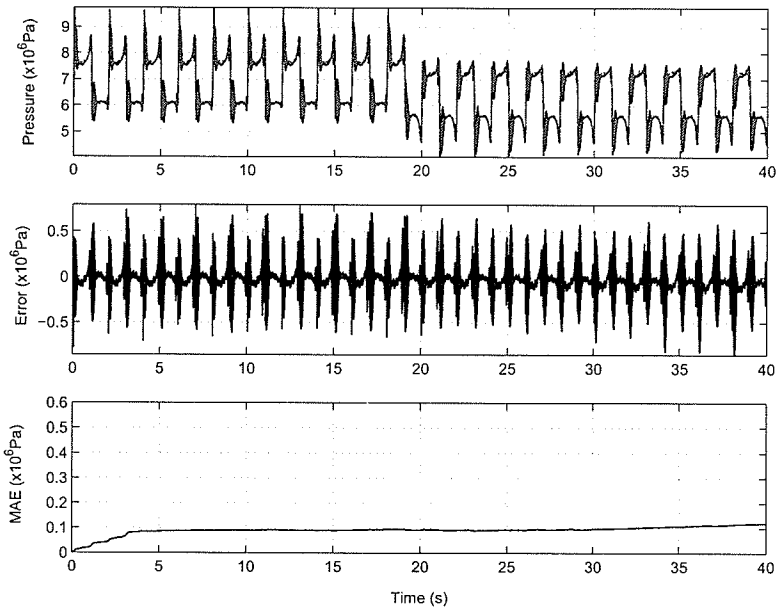

Figure 5.10: Measured and overlapped estimated pressures at chamber 1, residual error, and MAE.

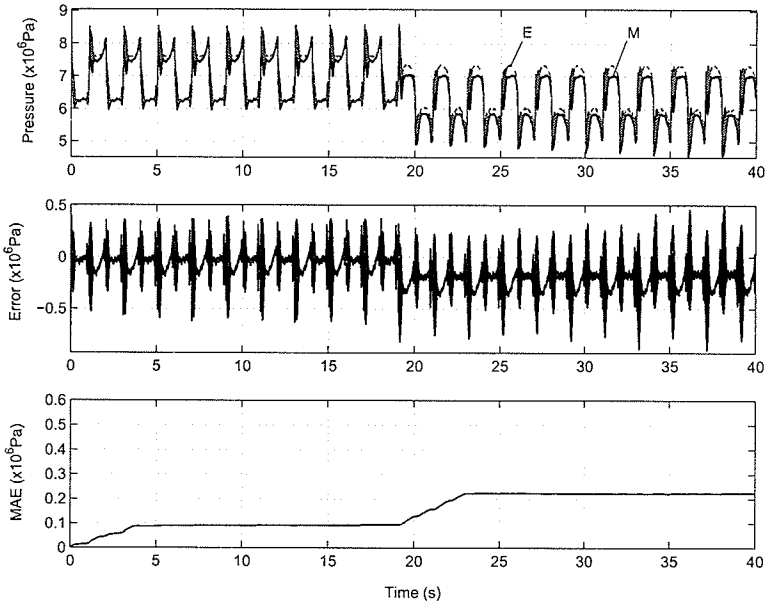

Figure 5.11: Measured (M) and estimated (E) pressures at chamber 2, error and MAE (estimated pressure closely follows the measured when there is no leakage).

two chambers, which is shown in Figure 2.6a. Similar to that in previous sections, the estimation of k_{il} is obtained by applying the square-root model.

$$k_{il} = \frac{1}{10^3 \cdot 60} \cdot \frac{q_{il}}{\sqrt{|(p_1 - p_2)|}} = 1.67 \times 10^{-5} \cdot \frac{q_{il}}{\sqrt{|(p_1 - p_2)|}} \tag{5.7}$$

Figure 5.12 shows plots of the leakage and corresponding k_{il}. The mean of the leakage coefficient is obtained as $\bar{k}_{il} = 1.11 \times 10^{-8}\,(\mathrm{m}^3/\mathrm{s} \cdot \mathrm{Pa})$, and the standard deviation is $\sigma_{il} = 2.60 \times 10^{-9}\,(\mathrm{m}^3/\mathrm{s} \cdot \mathrm{Pa})$.

The valve input and actuator displacement are shown in Figure 5.13. Comparing the plot of leakage in the same figure, it can be seen that the amplitude of the actuator displacement is reduced due to the internal leakage.

Generally, internal leakage damps the movement of the actuator and significantly affects the residual error of the actuator displacement (Figure 5.14). This is different from the residual errors with external leakage faults (Figures 5.3 and 5.9). Exploring the experimental results shown in Figures 5.15 and 5.16, it can be observed that the residual error of the chamber pressures both increase.

5.1.3 Fault Detection with Different Level of Leakages

By applying different level of leakages on the test rig, the variation of the residual errors related to the change of leakage flows can be obtained. Table 5.1 shows the leakage faults applied to the actuator.

Experimental results show that EKF is sensitive to the parameter change and the amount of leakage. A minimum external leakage flow of 0.154 l/min is detected. Figures 5.17 and 5.18 show two levels of leakage at chamber 1 and variation of corresponding MAE of the chamber pressure p_1. With the increase of the leakage flow

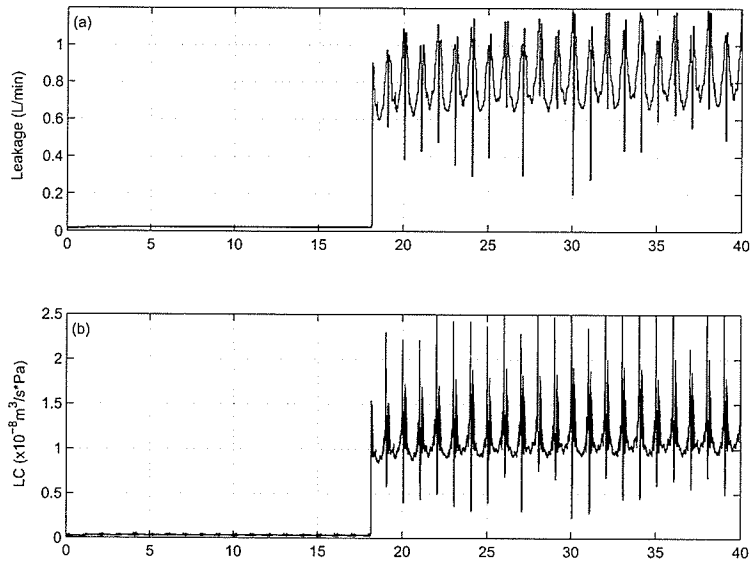

Figure 5.12: Internal leakage and leakage coefficient.

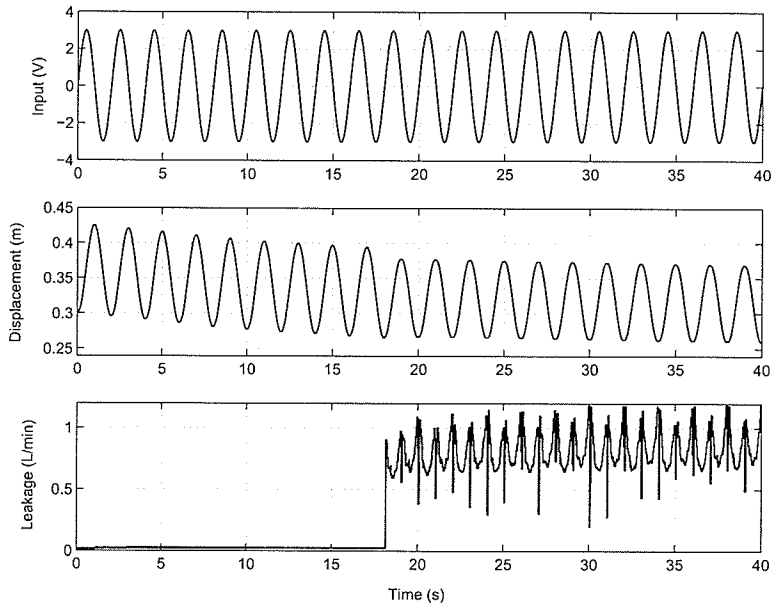

Figure 5.13: Input signal, measured actuator displacement and internal leakage.

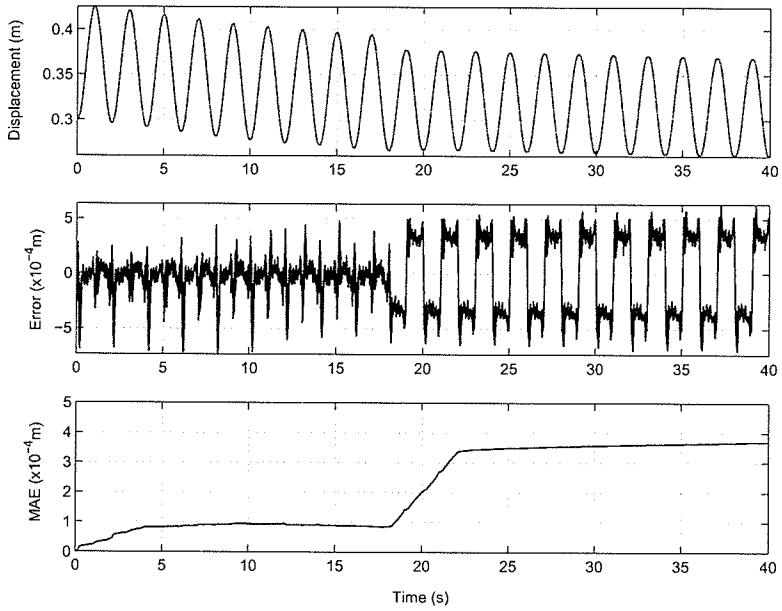

Figure 5.14: Measured and overlapped estimated actuator displacements, residual error and MAE.

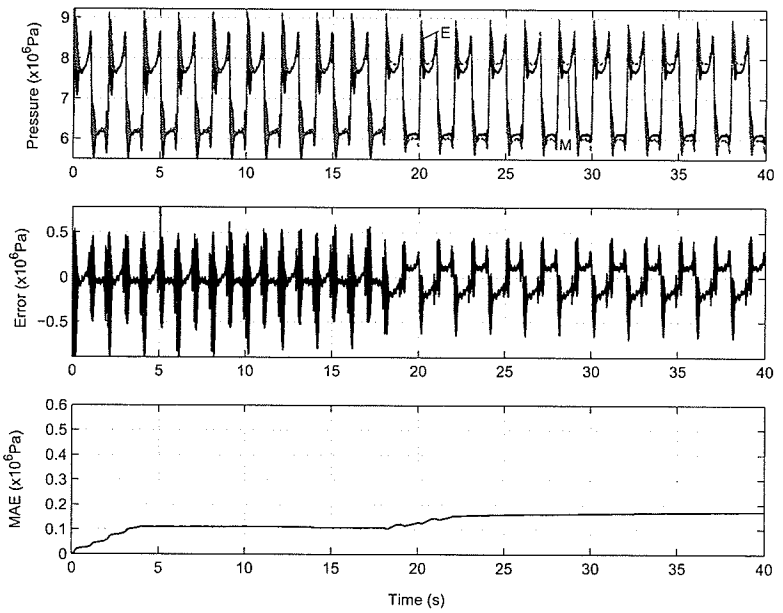

Figure 5.15: Measured (M) and estimated (E) pressures at chamber 1, residual error and MAE (estimated pressure closely follows the measured when there is no leakage).

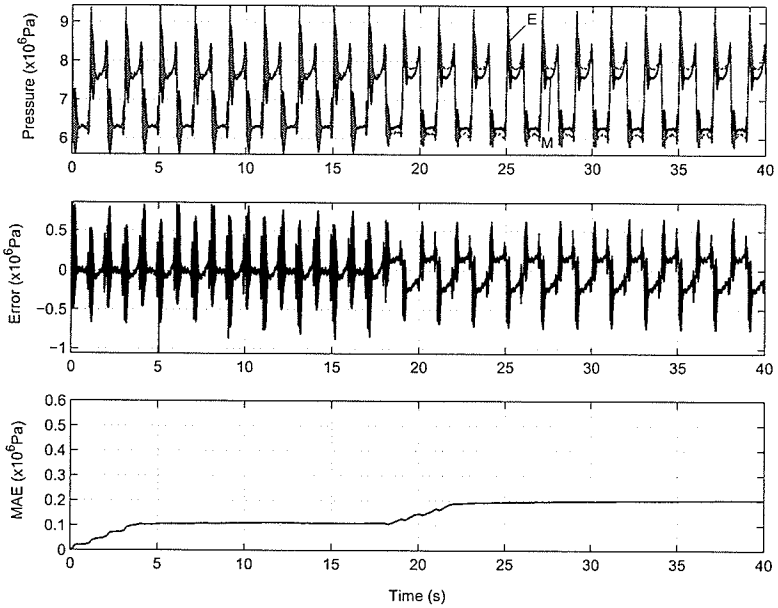

Figure 5.16: Measured (M) and estimated (E) pressures at chamber 2, residual error and MAE (estimated pressure closely follows the measured when there is no leakage).

at chamber 1, residual error of the chamber pressure accordingly increases after the occurrence of the leakage (Figure 5.14). The results shown in Figures 5.20, 5.22 and 5.23 illustrate consistent conclusion with the presence of leakage at chamber 2 and internal leakage.

What is noticeable in the results is the pattern of variations of the residual error corresponding to different leakage faults. Table 5.1 shows these patterns as well. When different leakage occurs at chamber 1, the MAE of the pressure at chamber 1 increases much more aggressively than that at the other chamber. For leakage at chamber 2, the MAE of pressure at chamber 2 increases. When the internal (crossport) leakage is initiated, MAEs of both chamber pressures increase. Therefore each leakage fault has a unique variation pattern and all three patterns are different

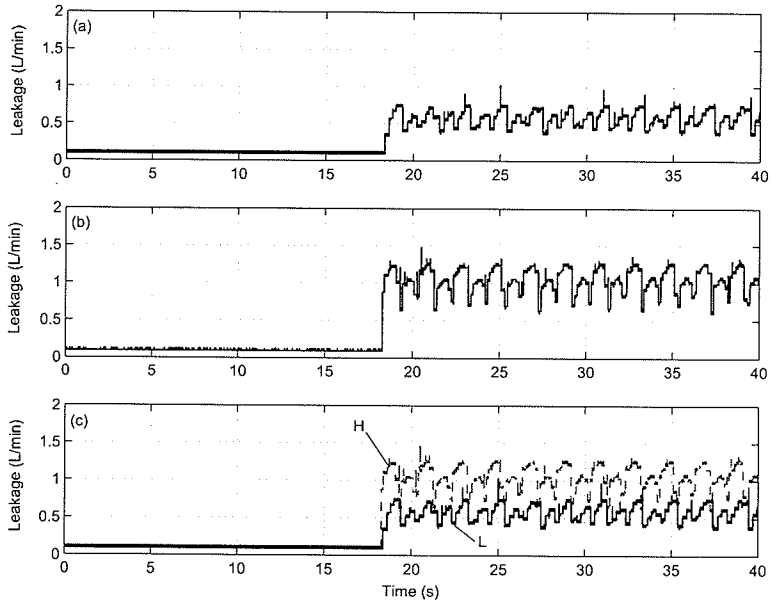

Figure 5.17: Low (L) and high (H) leakages at chamber 1. (a): low leakage; (b): high leakage; (c): comparison of (a) and (b).

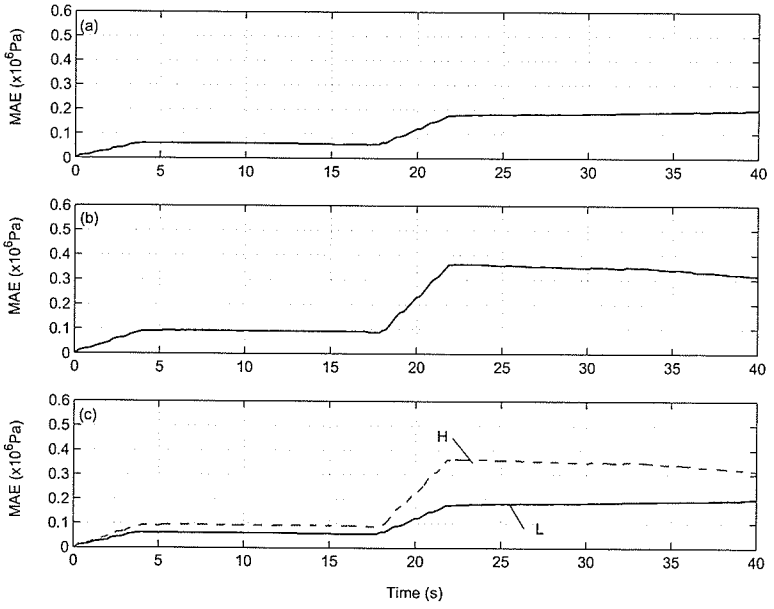

Figure 5.18: MAEs of chamber 1 pressure with low and high leakages at chamber 1. (a): MAE with low leakage; (b): MAE with high leakage; (c): comparison of (a) and (b).

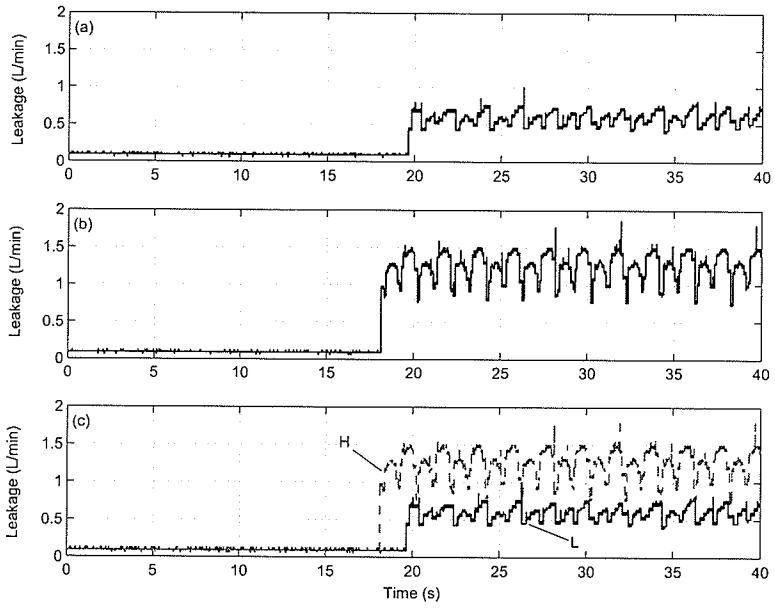

Figure 5.19: Low (L) and high (H) leakages at chamber 2. (a): low leakage; (b): high leakage; (c): comparison of (a) and (b).

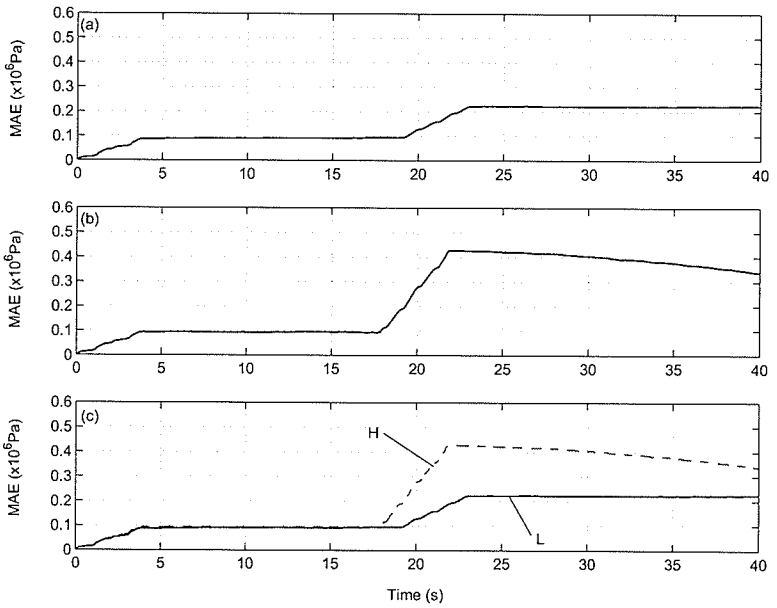

Figure 5.20: MAEs of chamber 2 pressure with low and high leakages at chamber 2. (a): MAE with low leakage; (b): MAE with high leakage; (c): comparison of (a) and (b).

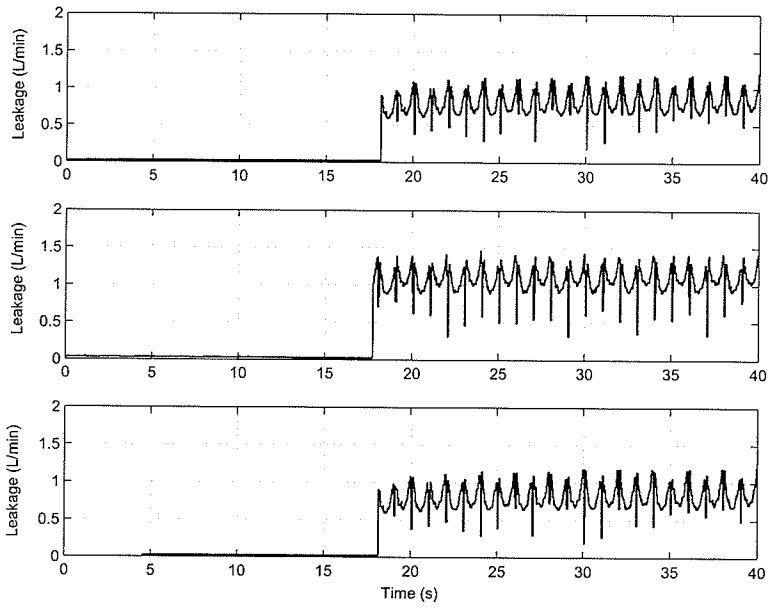
Leakage (L/min)
Leakage (L/min)
Leakage (L/min)
Time (s)

Table 5.1: Leakage faults parameters and chamber pressure MAEs in open-loop configuration.

Location of leakage	Chamber 1		Chamber 2		crossport leakage	
Leakage level	Low	High	Low	High	Low	High
Mean of LC $(m^3/s \cdot Pa) \times 10^{-9}$	3.87	7.67	4.04	9.50	11.10	14.43
Standard deviation $(m^3/s \cdot Pa) \times 10^{-10}$	8.03	14.04	7.03	16.26	26.00	30.90
MAE of Chamber 1 (Pa) $\times 10^6$	0.19	0.34	0.10	0.15	0.16	0.22
MAE of Chamber 2 (Pa) $\times 10^6$	0.08	0.11	0.21	0.40	0.20	0.26

from each other so that the leakage faults can be identified by observing the variation of residual errors.

Also interesting is that, in Table 5.1, it clearly shows that the MAE at the faulty chamber increases proportionally with the increase of leakage fault, while for the internal (crossport) leakage, MAE of both chamber pressures increase proportionally.

5.2 Closed-Loop Tests

Based on the tests in open-loop configuration, more tests are carried out in closed-loop configuration to investigate the performance of the FDI scheme with control systems, which is the normal operation in actual applications. A proportional controller is employed in this phase to regulate the motion of the actuator.

The experiments are conducted using two types of references: sinusoidal signal and pseudorandom signal. The sinusoidal signal is characterized with amplitude of

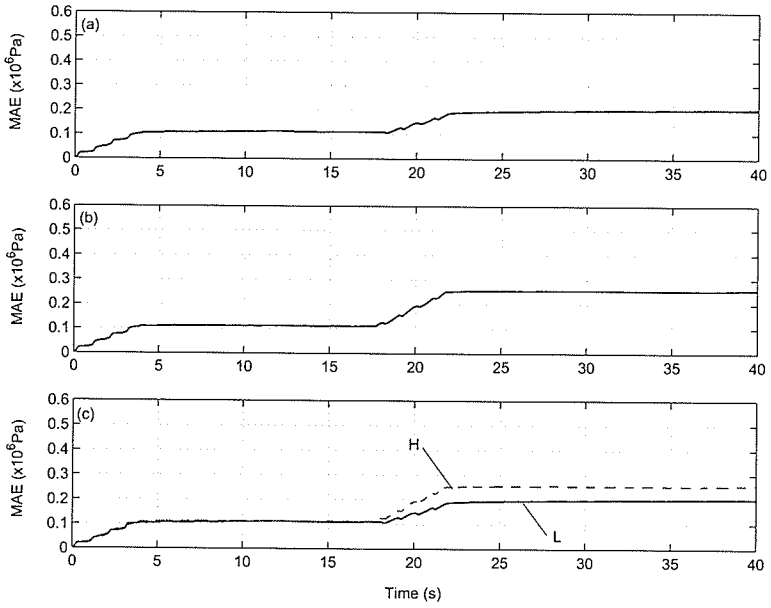

Figure 5.23: MAEs of chamber 2 pressure with low and high internal leakages. (a): MAE with low leakage; (b): MAE with high leakage; (c): comparison of (a) and (b).

0.2m and period of 2 seconds and the pseudorandom signal is generated with a region of [0.05m, 0.5m] and each random value is held for 2 seconds. Each pseudorandom test applies a unique input sequence.

The proportional controller is implemented by the PC. With a unity feedback of the actuator displacement and a DC gain of 50, the controller shows satisfactory steady-state responses. The block diagram of the system with controller is shown in Figure 5.24.

To fully investigate the performance of the proposed FDI scheme, aforementioned reference signals are applied to the test rig. All the parameters are kept the same as those for open-loop configuration to guarantee consistency with the open-loop results. Since the system is in closed-loop configuration, it can be seen from Figure 5.24 that

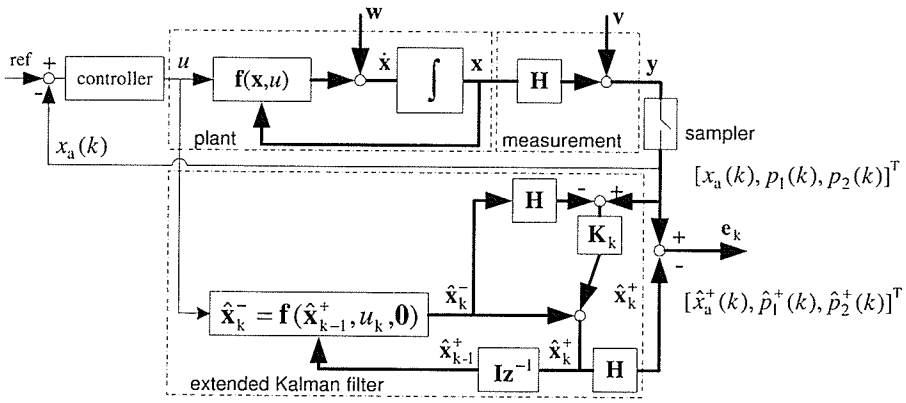

Figure 5.24: Test rig and the extended Kalman filter in closed-loop configuration.

the EKF acceptes the valve control signal u rather than the reference signal r, as its input.

5.2.1 Sinusoidal References

The experimental results are shown in Figures 5.25 to 5.28. Experiments show that the conclusions are consistent with those obtained in open-loop configuration even though the tests are carried out under closed-loop control scheme.

Table 5.2 presents the specifications of the leakage faults set to the test rig in closed-loop configuration as well as the variation of moving average errors.

5.2.2 Pseudorandom References

The pseudo random reference sequence simulates the working condition for a class of applications, in which series of simple "position-hold" operations are repeated continuously. This is common in off-highway machinery and the control surfaces of airplanes. With this reference sequence, the control signal delivered to the servovalve is similar to what is shown in the subplot for input, Figure 5.29. It is seen from

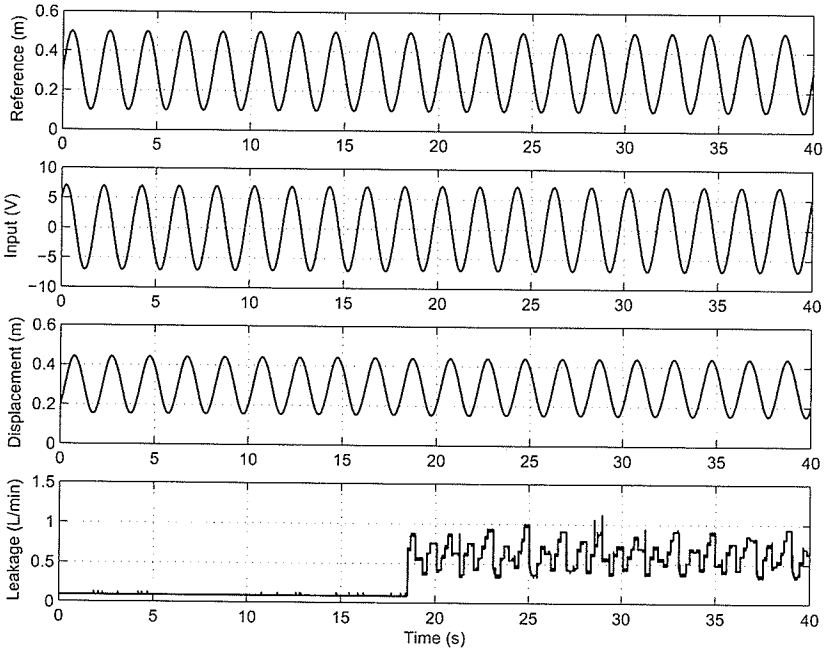

Figure 5.25: Reference signal, servovalve inputs, actuator displacement and leakage at chamber 1.

Table 5.2: Leakage fault parameters and chamber pressure MAEs in closed-loop configuration.

Location of leakage	Chamber 1		Chamber 2		Internal leakage	
Leakage level	Low	High	Low	High	Low	High
Mean of LC $(m^3/s \cdot Pa) \times 10^{-9}$	4.18	7.31	6.06	10.07	10.12	12.28
Standard deviation $(m^3/s \cdot Pa) \times 10^{-10}$	12.70	15.43	15.34	20.60	23.60	24.10
MAE of Chamber 1 $(Pa) \times 10^6$	0.24	0.38	0.17	0.20	0.20	0.29
MAE of Chamber 2 $(Pa) \times 10^6$	0.19	0.25	0.32	0.49	0.25	0.31

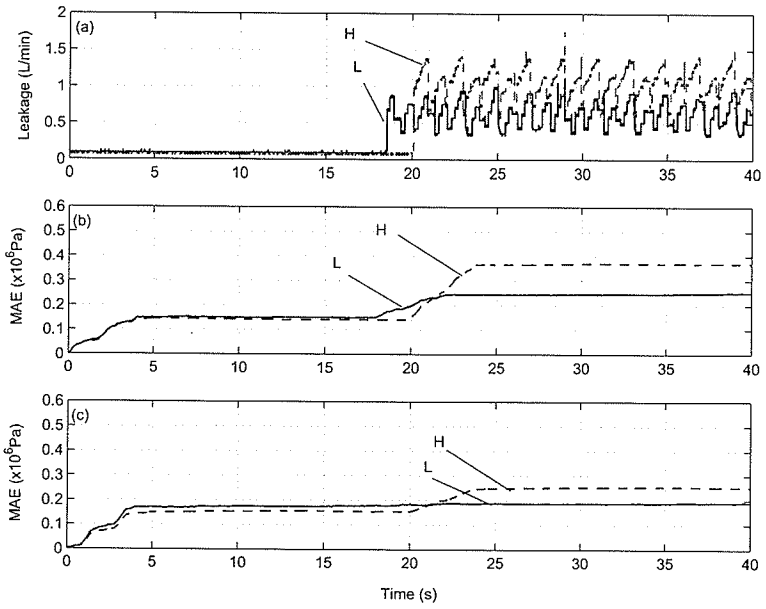

Figure 5.26: Leakages at chamber 1 and MAEs of chamber pressures. (a): low and high leakages; (b): MAEs of chamber 1 pressure; (c): MAEs of chamber 2 pressure.

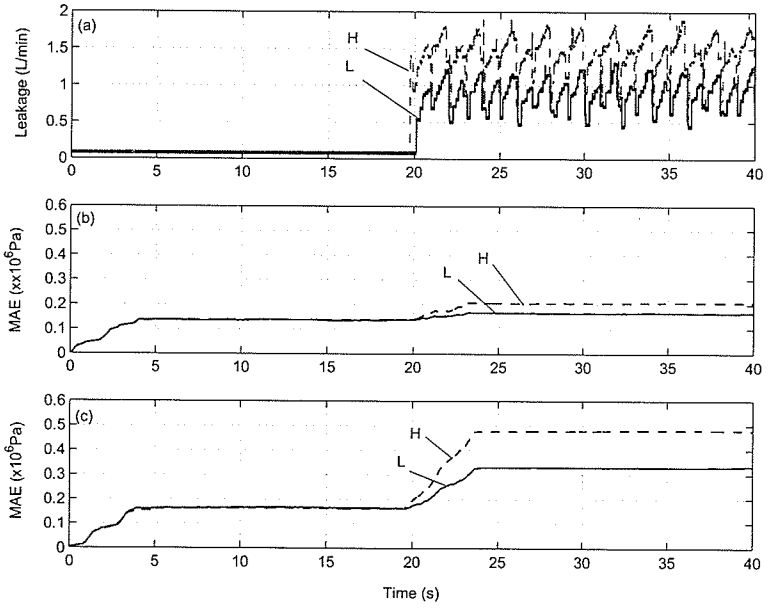

Figure 5.27: Leakages at chamber 2 and MAEs of chamber pressures. (a): low and high leakages; (b): MAEs of chamber 1 pressure; (c): MAEs of chamber 2 pressure.

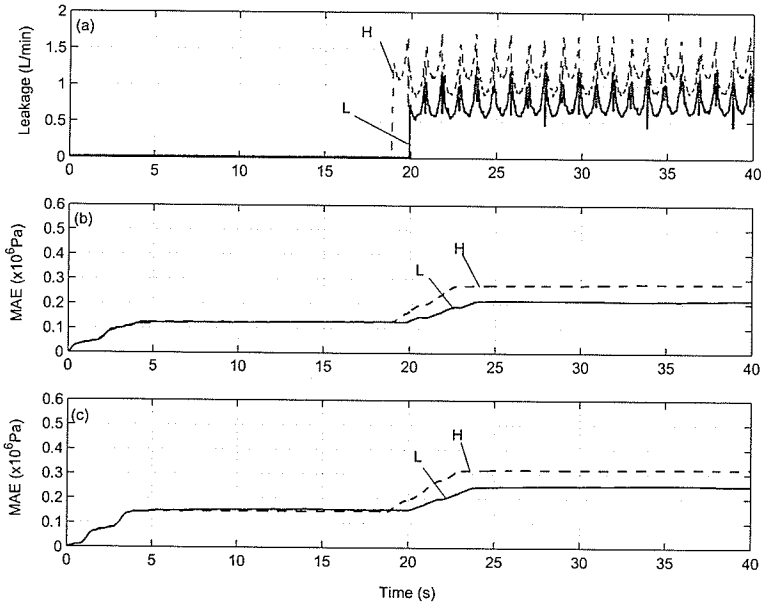

Figure 5.28: Internal leakages and MAEs of chamber pressures. (a): low and high leakages; (b): MAEs of chamber 1 pressure; (c) MAEs of chamber 2 pressure.

Figures 5.29 to 5.32 that the residual errors are not as smooth and constant as those obtained in sinusoidal test when low leakage occurs at chamber 1. This is mainly due to the discontinuity of the control signal and the significant variance of leakage flow. Nevertheless, the increase of residual errors still illustrates the occurrence of the leakage. The moving average error of the pressure at chamber 1 increases in Figure 5.31 though the fluctuation is more noticeable due to random excitation. Most of the moving average values exceeds 2×10^5 Pa after the leakage occurrs at the 18th second, while the moving average of the residual error on the other side stays below 2×10^5 Pa. The identification patterns for different leakages still exist when the plots of the residual errors are investigated. This is consistent with previous conclusions.

When different leakage levels are applied to the actuator, the residual errors show

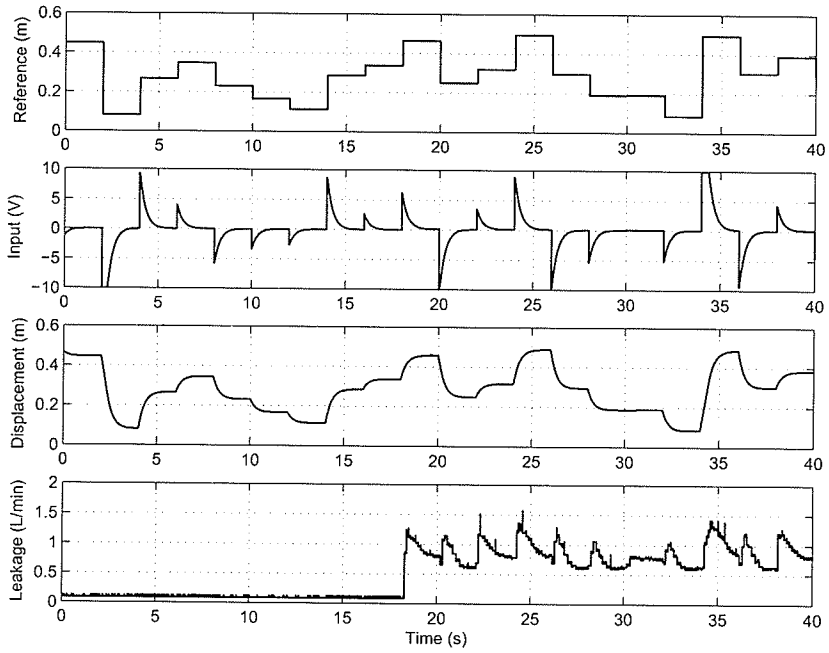

Figure 5.29: Reference signal, servovalve inputs, actuator displacement and leakage at chamber 1.

their sensitivities to the variation of leakage flow. Figures 5.33 to 5.39 show the variation of residual errors with different leakage levels. Observe the leakage flows shown in Figures 5.33, 5.35 and 5.37, it can be seen that due to the pseudorandom reference inputs, the leakage flows are pulsive. Furthermore, the leakage flows do not increase accordingly even though the leakage coefficients have significantly increased.

As a result, the difference between the MAE of chamber pressures is not significant and constant ranges for MAEs are hard to obtain. However, when the plots of MAEs are compared with corresponding leakage flows, it can be concluded that higher leakage flows cause larger increases in residual errors. For instance, the difference between the low and high leakage flow in Figure 5.33 are significant between the 20th and the 35th second. The increase of MAE with high leakage is consequently

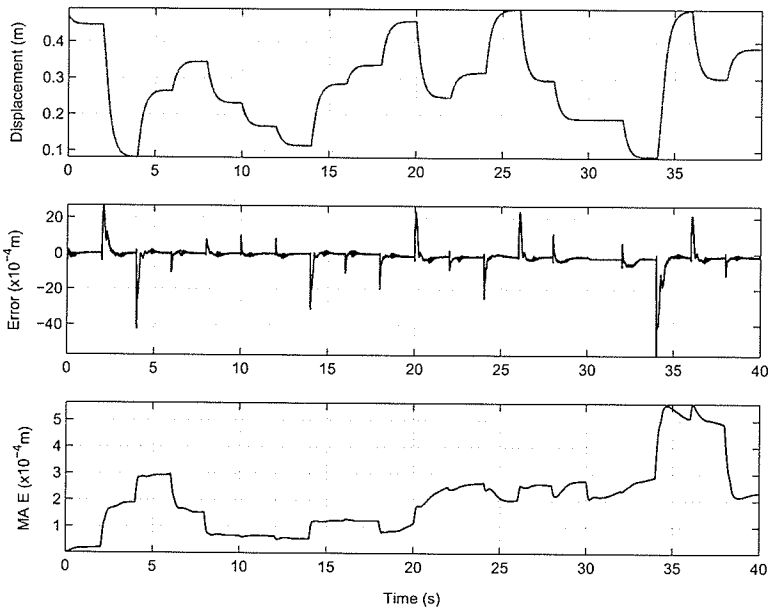

Figure 5.30: Measured and overlapped estimated actuator displacements and MAE with leakage at chamber 1.

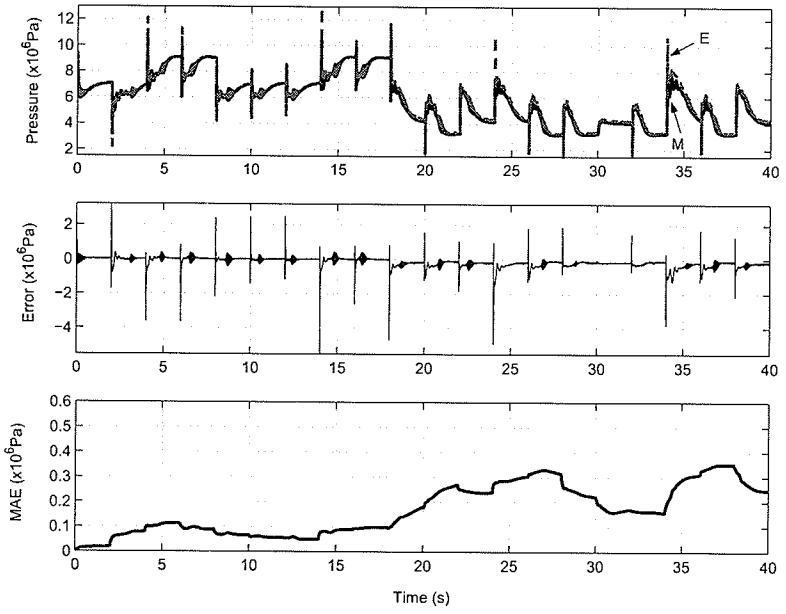

Figure 5.31: Measured (M) and estimated (E) chamber 1 pressures, residual error and MAE with leakage at chamber 1 (Estimated pressure closely follows the measured when there is no leakage.

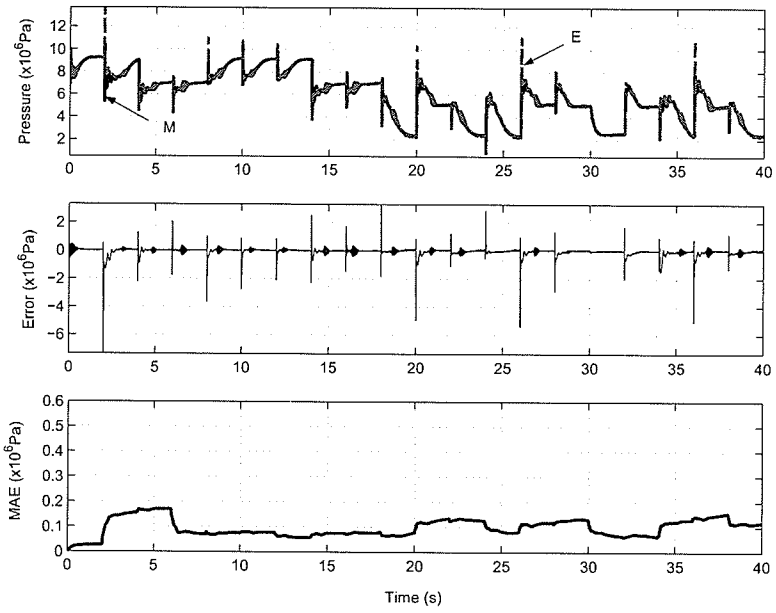

Figure 5.32: Measured (M) and estimated (E) chamber 2 pressures, residual error and MAE with leakage at chamber 2.

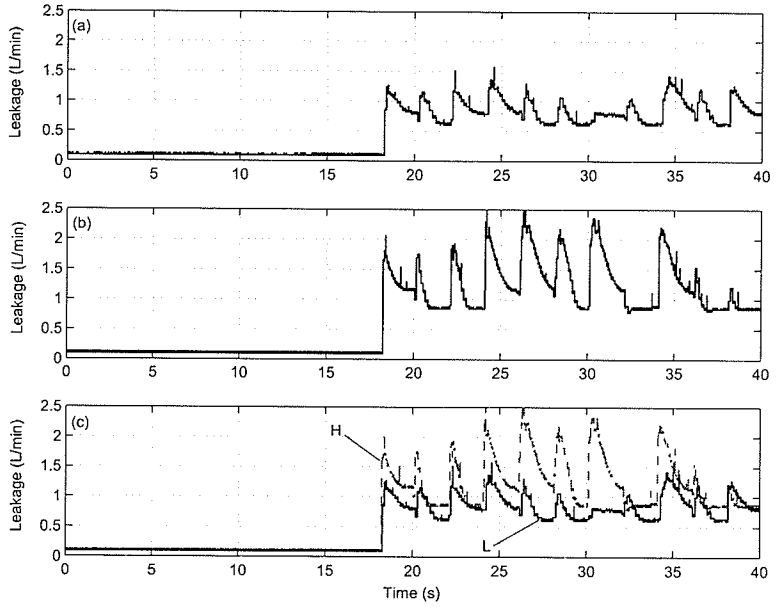

Figure 5.33: Low (L) and high (H) leakages at chamber 1. (a): low leakage; (b): high leakage; (c): comparison of (a) and (b).

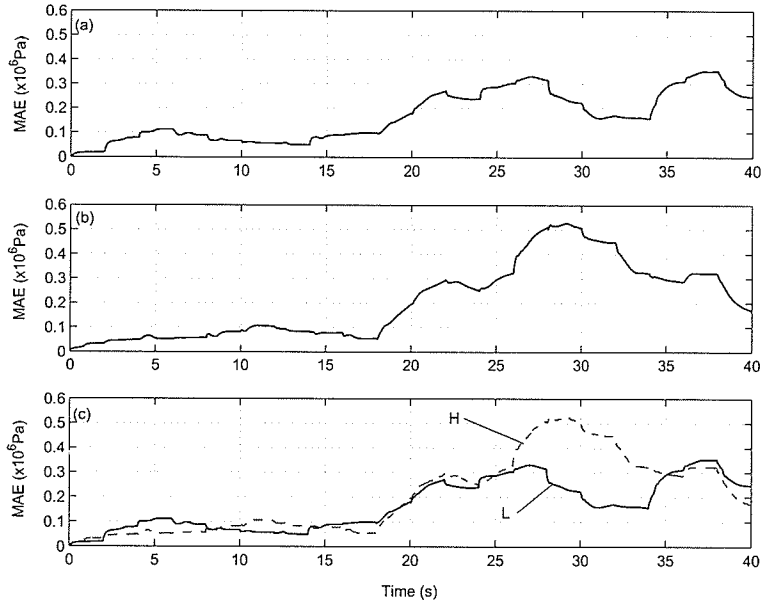

Figure 5.34: MAEs of chamber 1 pressure with low (L) and high (H) leakages at chamber 1. (a): MAE with low leakage; (b): MAE with high leakage; (c): comparison of (a) and (b).

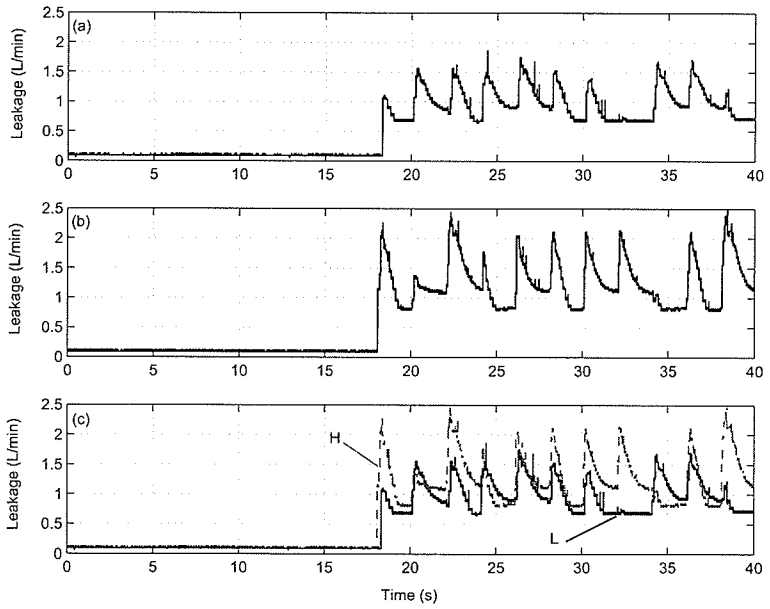

Figure 5.35: Low (L) and high (H) leakages at chamber 2. (a): low leakage; (b): high leakage; (c): comparison of (a) and (b).

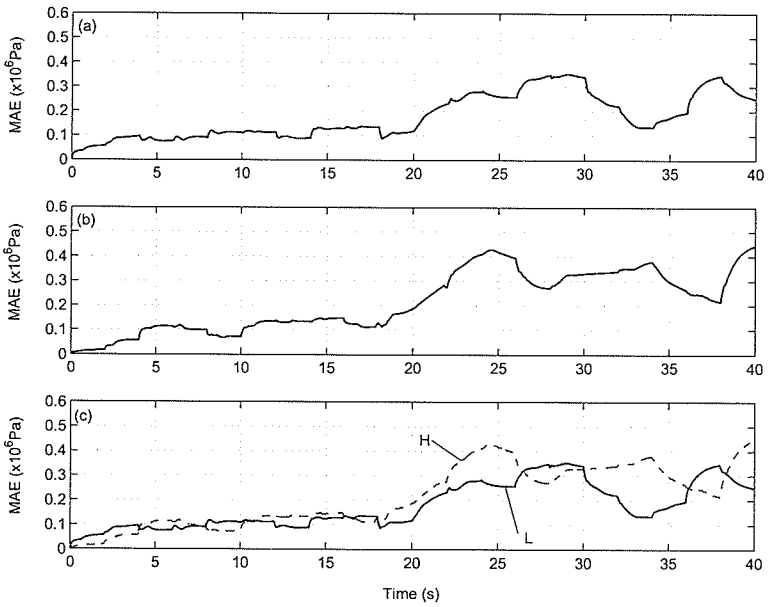

Figure 5.36: MAEs of chamber 2 pressure with low (L) and high (H) leakages at chamber 2. (a): MAE with low leakage; (b): MAE with high leakage; (c): comparison of (a) and (b).

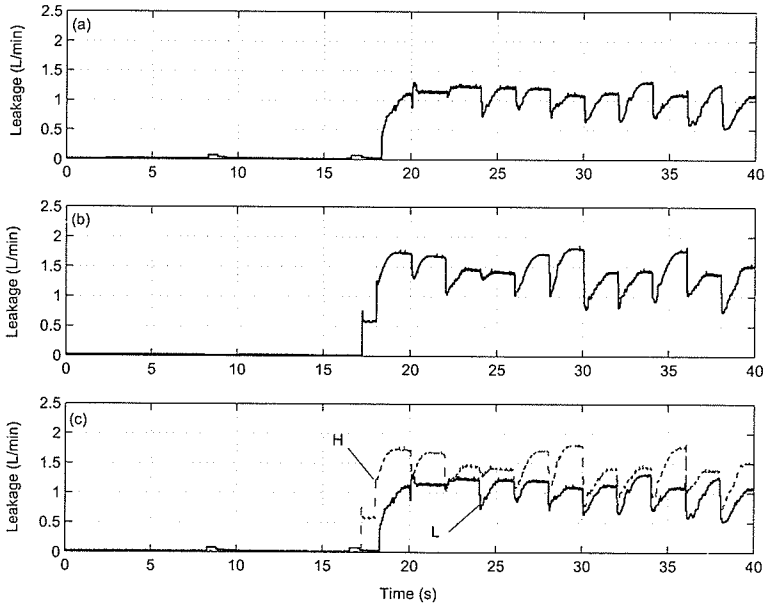

Figure 5.37: Low (L) and high (H) internal leakages. (a): low leakage; (b): high leakage; (c): comparison of (a) and (b).

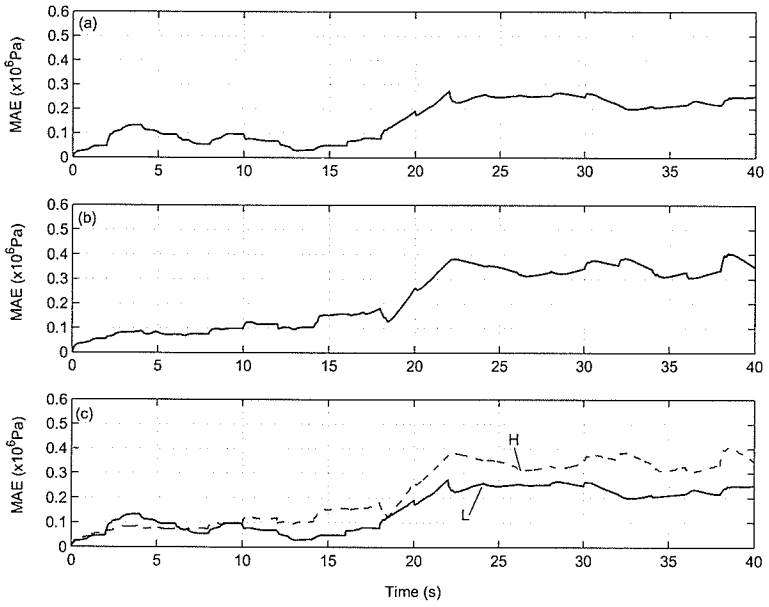

Figure 5.38: MAEs of chamber 1 pressure with low (L) and high (H) internal leakages. Subplot (a): MAE with low leakage; (b): MAE with high leakage; (c): comparison of (a) and (b).

very significant during the same period. This is also verified by the following plots for leakage at chamber 2 and crossport leakage. The specifications of different leakage levels are shown in Table 5.3:

Table 5.3: Leakage fault parameters in closed-loop configuration with pseudorandom references.

Location of leakage	Chamber 1		Chamber 2		Internal leakage	
Leakage level	Low	High	Low	High	Low	High
Mean of LC $(m^3/s \cdot Pa) \times 10^{-9}$	6.83	12.69	8.45	12.52	13.42	15.54
Standard deviation $(m^3/s \cdot Pa) \times 10^{-10}$	10.19	20.20	14.58	20.40	18.70	21.50

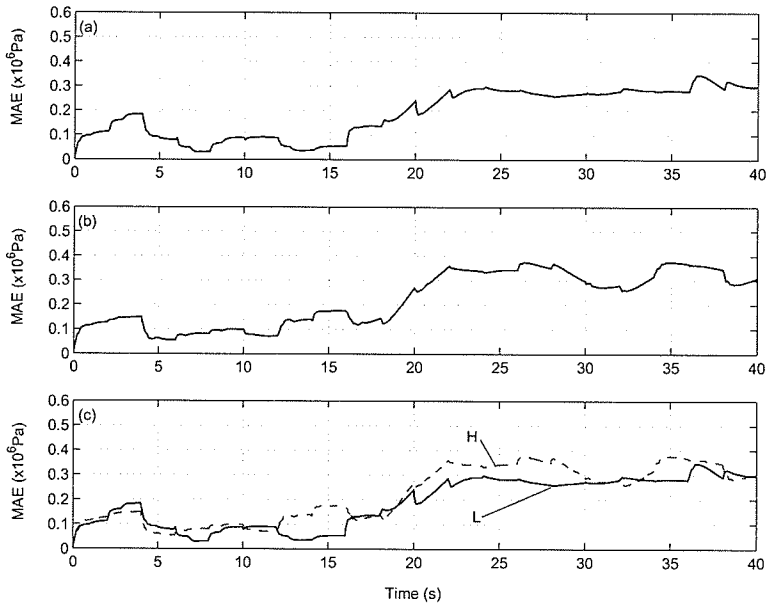

Figure 5.39: MAEs of chamber 2 pressure with low (L) and high (H) internal leakages. (a): MAE with low leakage; (b): MAE with high leakage; (c): comparison of (a) and (b).

5.3 Summary of Test Results

Experiments show that, with only three low-cost measurements, i.e., the actuator displacement and the line pressures, the constructed EKF-based fault detector is experimentally shown to successfully identify types and distinguish levels, of external as well as internal individual leakage faults in the actuator. No specific assumptions about the models for the leakage faults have been made. It is shown that according to the residual errors obtained by monitoring the chamber pressures only, different patterns can be obtained, which can be used to detect leakage faults at the early stage. Particularly, it is observed that the magnitude of the change of the residual errors, caused by the leakage faults, increase proportionally with the increase of fault levels.

This is significant since it allows the progress of the leakage flows to be monitored.

Chapter 6

Leakage Fault Detection and Isolation Subject to External Load

In Chapter 2 to 5, the modeling of a class of electrohydraulic actuation system and corresponding estimating scheme were introduced. An appropriate scheme for leakage fault detection and isolation based on EKF theory was developed and tested on an experimental setup. However, the actuation system was only tested in unloaded mode. When external load exists, the system characteristics change due to the disturbance of external load and experiments verified that the FDI scheme based on unloaded system modeling does not converge when external load exists. On the other hand, most actuation systems inevitably interact with the environment such as the air flow on the aircraft control surface and the dynamic load on the boom or stick of an excavator.

Meanwhile, the actuator friction is always an important factor that has to be handled carefully. Due to its nonlinearity, appropriate modeling of the friction is difficult and subject to change with component wear and parameter drifting. Some researchers have shown various approaches to determine the parameters of certain friction model (Chinniah et al; 2003). However, it is impossible to precisely measure

the friction and set up the friction model for each individual actuator. Therefore online estimation of friction has apparent advantage in dealing with the nonlinearities caused by friction.

In Chapter 2, the friction was seperately modeled and was combined with system modeling. In this chapter, the friction and external load are regarded as time-varying parameters of the actuation system and are modeled together as an expanded state variable of the system. Corresponding leakage detection scheme is developed and shown in this chapter.

6.1 Environmental Setup

To simulate the external load, the environment is approximated as an elastic body with a large modulus of elasticity. On the test rig, a stiff coil spring is employed for this purpose (see Figure 6.1). The coil spring, with a modulus of 6×10^5 N/m, can generate up to 6000 N when compressed by 1 cm. A force sensor [0~22,000N (5000lb)] is mounted at the end of the actuator rod to instantly measure the external force. Detailed modeling of the environment or the spring is avoided as the environment is expected to be estimated and recognized by the FDI scheme.

Figure 6.2 shows the experimental setup. The coil spring is installed on the track of the rod at certain position so that when the rod extends it presses on the spring. The spring is then compressed and generates a reactive force. Varying load is thus obtained at different positions when the compression of the spring.

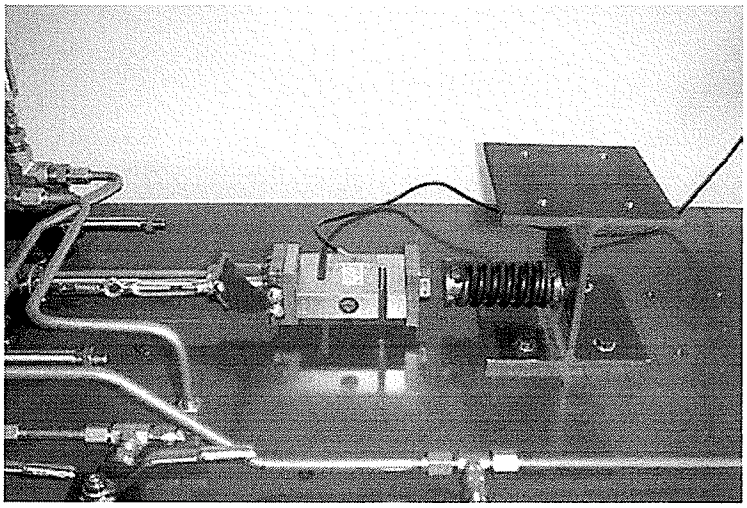

Figure 6.1: Coil spring environment simulator.

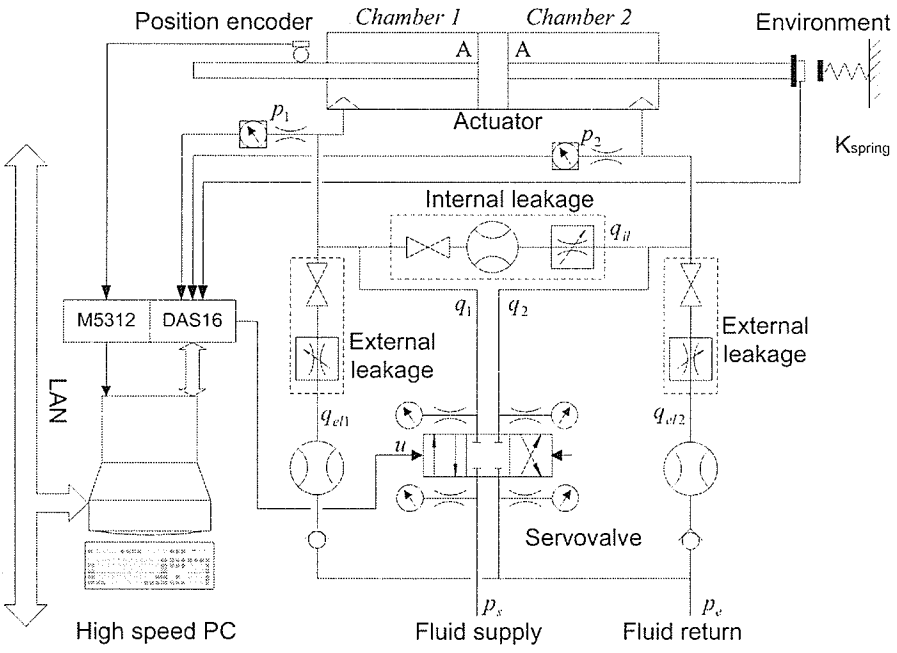

Figure 6.2: Hydraulic test station with a spring-like environment.

6.2 Modeling of External Load

An actuator working in actual applications deals with varying loads that are unpredictable. Attempts have been made to model this operating condition and researches that consider load for real-time control and estimation have been reported in the literature. Lin (1996) showed a RLS estimator with torque observer in an induction motor controller design. The torque observer implemented inverse dynamics of the motor to observe the torque, while the key parameter of the observer was obtained from an EKF. More direct application of EKF in load estimation has been reported by Beineke et al (1997) in whose paper the load condition was described by deterministic characteristics. The torque of a motor drive was directly regarded as an expanded system state in the EKF and the estimation of friction and loading torque was reported to be successful. Zavarehi et al (1999) showed the possibility of estimating some immeasurable key-parameters of a servovalve.

As a statistical method, EKF is based on Bayesian estimation. All system states are considered to be random variables due to the disturbance of white noises and are estimated based on previous estimates and updates of the measurements. On the other hand, the dynamic model of the system regulates the evolution of system states and characterizes the conditional estimation, shown in the following equation:

$$\hat{\mathbf{x}}_k^+ = E[\mathbf{x}_k|\mathbf{z}_1 \cdots \mathbf{z}_k] \tag{6.1}$$

where $\hat{\mathbf{x}}_k^+$ is the *a posteriori* estimate at time instance k, $E[\cdot]$ represents the expectation, $\mathbf{x}_k$ is the system state at time instance k, and $\mathbf{z}_i$ $(i = 1 \ldots k)$ are the updates of measurements. When a system parameter, θ, is included in this model, it is regarded

as a random walk with certain mean (expectation) but deteriorated by noise. Ideally, the parameter is time invariant so that it can be expressed by the following differential equation with noise that can be characterized as a random variable:

$$\frac{d\theta}{dt} = 0 + q(t) \tag{6.2}$$

where $q(t)$ represents the density of the white noise. It can be seen from this equation that the EKF is indifferent to the system states and the parameters so the formulation of them is identical. Furthermore, the corresponding covariance in the Kalman filter algorithm serves as a design parameter to describe how fast the parameter is expected to vary. The bigger this variance is, the better time-varying parameters are tracked but the constant parameters are noisier (Beineke et al, 1997).

6.3 Modified System Model and FDI Scheme

6.3.1 System Model

The system model for the actuation system is represented by the flow equations described in Chapter 2. These equations are referred again for convenience:

$$\begin{cases} q_1 = C_d w x_{sp} \sqrt{\frac{2}{\rho}(p_s - p_1)} \\ q_2 = C_d w x_{sp} \sqrt{\frac{2}{\rho}(p_2 - p_e)} \end{cases} \quad x_{sp} > 0 \tag{6.3}$$

$$\begin{cases} q_1 = C_d w x_{sp} \sqrt{\frac{2}{\rho}(p_1 - p_e)} \\ q_2 = C_d w x_{sp} \sqrt{\frac{2}{\rho}(p_s - p_2)} \end{cases} \quad x_{sp} < 0 \tag{6.4}$$

Without considering the servovalve leakages in the healthy system, we have

$$\begin{cases} q_1 = A\dot{x}_a + \frac{1}{\beta} V_1(x_a)\dot{p}_1 \\ q_2 = A\dot{x}_a - \frac{1}{\beta} V_2(x_a)\dot{p}_2 \end{cases} \tag{6.5}$$

where

$$\begin{cases} V_1(x_a) = V_1^0 + A(x_a - X_{min}) \\ V_2(x_a) = V_2^0 + A(X_{max} - x_a) \end{cases} \tag{6.6}$$

and the dynamic equation of the servovalve is given as

$$u = \frac{1}{k_{sp}\omega_n^2}\ddot{x}_{sp} + \frac{d_m}{k_{sp}\omega_n}\dot{x}_{sp} + \frac{1}{k_{sp}}x_{sp} \tag{6.7}$$

Equations (6.3) to (6.7) describe the dynamics of the hydraulic system. To include the external force in the system modeling, consider Figure 6.2 and equation (2.10), then the following equation is obtained:

$$f_a = (p_1 - p_2)A = m_a\ddot{x}_a + F_c + F_r \tag{6.8}$$

where, as defined before, f_a is the actuator force generated by the pressure difference between the two chambers. F_c is the friction and F_r is the external resistance force. For actual applications, F_c and F_r are unknown but bounded values when the system is working under normal operation condition, so that the effective load (disturbance) for the actuator, including friction and external load, can be given as $F_e = F_c + F_r$. This external disturbance is characterized as a stochastic process in the actuator model and equation (6.8) is rewritten as:

$$f_a = m_a\ddot{x}_a + F_e \tag{6.9}$$

When the external load varies, it implies that the mean of this stochastic process varies. Furthermore, if the external load F_r does not exist, equation (6.9) becomes equation (2.10) and the estimation of external load reflects the actuator friction.

6.3.2 FDI Scheme Development

System Re-modeling

Similar to the analysis in Chapter 4, this system is regarded as a stochastic process contaminated with process noise $\mathbf{w}_\xi$ and measurement noise $\mathbf{v}$, which can be shown as

$$\begin{cases} \dot{\boldsymbol{\xi}} = \mathbf{f}(\boldsymbol{\xi},\, u) + \mathbf{w}_\xi \\ \mathbf{y} = \mathbf{h}(\boldsymbol{\xi}, \mathbf{v}) \end{cases} \tag{6.10}$$

where u is the input signal and $\mathbf{y}$ is the measurement array. Choosing the actuator displacement and its velocity, the chamber pressures, the displacement of the valve spool and its velocity, the state vector is $\boldsymbol{\xi}$=$[\, x_{sp}, p_1, p_2, x_a, \dot{x}_a, \dot{x}_{sp}\,]^{\mathrm{T}}$. Correspondingly, the state space model of the actuation system is formulated as:

$$\begin{cases} \dot{\xi}_1 = \xi_6 + w_1 \\ \dot{\xi}_2 = \begin{cases} \frac{\beta}{V_1(\xi_4)}[C_d w \xi_1 \sqrt{\frac{2}{\rho}(p_s - \xi_2)} - A\xi_5] + w_2 & \xi_1 > 0 \\ \frac{\beta}{V_1(\xi_4)}[C_d w \xi_1 \sqrt{\frac{2}{\rho}(\xi_2 - p_e)} - A\xi_5] + w_2 & \xi_1 < 0 \end{cases} \\ \dot{\xi}_3 = \begin{cases} \frac{\beta}{V_2(\xi_4)}[-C_d w \xi_1 \sqrt{\frac{2}{\rho}(\xi_3 - p_e)} + A\xi_5] + w_3 & \xi_1 > 0 \\ \frac{\beta}{V_2(\xi_4)}[-C_d w \xi_1 \sqrt{\frac{2}{\rho}(p_s - \xi_3)} + A\xi_5] + w_3 & \xi_1 < 0 \end{cases} \\ \dot{\xi}_4 = \xi_5 + w_4 \\ \dot{\xi}_5 = \frac{1}{m_a}(A\xi_2 - A\xi_3 - F_e) + w_5 \\ \dot{\xi}_6 = -2d_m\omega_n\xi_6 - \omega_n^2\xi_1 + k_{sp}\omega_n^2 u + w_6 \end{cases} \tag{6.11}$$

To further estimate the unknown external resistance, F_e is also formulated as a special state. EKF regards this parameter as a random variable so that the stochastic

process in equation (6.10) is expanded as the following system:

$$\begin{cases} \begin{bmatrix} \dot{\boldsymbol{\xi}} \\ \dot{\boldsymbol{\theta}} \end{bmatrix} = \begin{bmatrix} \mathbf{f}(\boldsymbol{\xi}, u) \\ \mathbf{0} \end{bmatrix} + \begin{bmatrix} \mathbf{w}_{\xi} \\ \mathbf{w}_{\theta} \end{bmatrix} \\ \mathbf{y} = \mathbf{h}(\boldsymbol{\xi}, \mathbf{v}) \end{cases} \tag{6.12}$$

where $\boldsymbol{\theta}$=$[F_e]$ represents possible parameter array being estimated and $\mathbf{w}_{\theta}$ is the corresponding noise array. Following the formulation of equation (6.12), an expanded state vector can be defined in a general form as $\mathbf{x} = [\,\boldsymbol{\xi}\ \boldsymbol{\theta}\,]^{\mathrm{T}} = [\,x_{sp},\, p_1,\, p_2,\, x_a,\, \dot{x}_a,\, \dot{x}_{sp},\, F_e\,]^{\mathrm{T}}$ and the corresponding noise array can be rewritten as:

$$\mathbf{w} = [\,\mathbf{w}_{\xi}\ \mathbf{w}_{\theta}\,]^{\mathrm{T}} = [\,w_1,\, w_2,\, w_3,\, w_4,\, w_5,\, w_6,\, w_7\,]^{\mathrm{T}}$$

The state space model of the expanded system is then discretized using forward difference method, as shown in the following equations:

$$x_1(k+1) = Tx_6(k) + x_1(k) + w_1(k) \tag{6.13}$$

$$x_2(k+1) = \begin{cases} \frac{T\beta}{V_1(x_4(k))}[C_d w x_1(k)\sqrt{\frac{2}{\rho}(p_s - x_2(k))} - Ax_5(k)] & \\ +x_2(k) + w_2(k) & x_1(k) > 0 \\ \frac{T\beta}{V_1(x_4(k))}[C_d w x_1(k)\sqrt{\frac{2}{\rho}(x_2(k) - p_e)} - Ax_5(k)] & \\ +x_2(k) + w_2(k) & x_1(k) \le 0 \end{cases} \tag{6.14}$$

$$x_3(k+1) = \begin{cases} \frac{T\beta}{V_2(x_4(k))}[-C_d w x_1(k)\sqrt{\frac{2}{\rho}(x_3(k) - p_e)} + Ax_5(k)] & \\ +x_3(k) + w_3(k) & x_1(k) > 0 \\ \frac{T\beta}{V_2(x_4(k))}[-C_d w x_1(k)\sqrt{\frac{2}{\rho}(p_s - x_3(k))} + Ax_5(k)] & \\ +x_3(k) + w_3(k) & x_1(k) \le 0 \end{cases} \tag{6.15}$$

$$x_4(k+1) = Tx_5(k) + x_4(k) + w_4(k) \tag{6.16}$$

$$x_5(k+1) = \frac{T}{m_a}(Ax_2(k) - Ax_3(k) - x_7(k)) + x_5(k) + w_5(k) \tag{6.17}$$

$$x_6(k+1) = T[-2d_m\omega_n x_6(k) - \omega_n^2 x_1(k) + k_{sp}\omega_n^2 u(k+1)] + x_6(k) + w_6(k) \tag{6.18}$$

$$x_7(k+1) = x_7(k) + w_7(k) \tag{6.19}$$

where T represents the sampling interval,i.e., sampling time is KT.

Jacobian Matrices

Based on the discrete model represented by equation (6.12) to (6.19), the FDI scheme is constructed. Similar to the procedure discussed in Chapter 4, to apply EKF algorithm to the aforementioned space model, the Jacobian matrices **A**, **W**, **H** and **V** are required. Knowing the sampling time, T, matrix **A** is obtained from equation (4.11) as

$$\mathbf{A} = \frac{\partial \mathbf{f}}{\partial \mathbf{x}} = \left[\frac{\partial f_1}{\partial \mathbf{x}}, \frac{\partial f_2}{\partial \mathbf{x}}, \frac{\partial f_3}{\partial \mathbf{x}}, \frac{\partial f_4}{\partial \mathbf{x}}, \frac{\partial f_5}{\partial \mathbf{x}}, \frac{\partial f_6}{\partial \mathbf{x}}, \frac{\partial f_7}{\partial \mathbf{x}}\right]^{\mathrm{T}} \tag{6.20}$$

where

$$\frac{\partial f_1}{\partial \mathbf{x}} = [1, \quad 0, \quad 0, \quad 0, \quad 0, \quad T, \quad 0],$$

$$\frac{\partial f_2}{\partial \mathbf{x}} = \begin{bmatrix} \frac{T\beta}{V_1(x_4(k))} C_d w x_1(k)\sqrt{\frac{2}{\rho}(p_s - x_2(k))}, \\ 1 + \frac{T\beta}{V_1(x_4(k))} C_d w x_1(k)\left(\frac{-1}{\rho\sqrt{\frac{2}{\rho}(p_s - x_2(k))}}\right), \\ 0, \\ -\frac{T\beta}{V_1^2(x_4(k))}\dot{V}_1(x_4(k))\left[C_d w x_1(k)\sqrt{\frac{2}{\rho}(p_s - x_2(k))} - Ax_5(k)\right], \\ \frac{T\beta}{V_1(x_4(k))}(-A), \\ 0, \quad 0 \end{bmatrix} \qquad x_1(k) > 0$$

$$\frac{\partial f_2}{\partial \mathbf{x}} = \begin{bmatrix} \frac{T\beta}{V_1(x_4(k))} C_d w x_1(k) \sqrt{\frac{2}{\rho}(x_2(k) - p_e)}, \\ 1 + \frac{T\beta}{V_1(x_4(k))} C_d w x_1(k) \Big(\frac{1}{\rho \sqrt{\frac{2}{\rho}(x_2(k) - p_e)}} \Big), \\ 0, \\ -\frac{T\beta}{V_1^2(x_4(k))} \dot{V}_1(x_4(k)) \Big[C_d w x_1(k) \sqrt{\frac{2}{\rho}(x_2(k) - p_e)} - A x_5(k) \Big], \\ \frac{T\beta}{V_1(x_4(k))}(-A), \\ 0, \quad 0 \end{bmatrix} \qquad x_1(k) \leq 0$$

$$\frac{\partial f_3}{\partial \mathbf{x}} = \begin{bmatrix} \frac{T\beta}{V_2(x_4(k))} \Big[- C_d w x_1(k) \sqrt{\frac{2}{\rho}(x_3(k) - p_e)} \Big], \\ 0, \\ 1 + \frac{T\beta}{V_2(x_4(k))} \Big[- C_d w x_1(k) \Big(\frac{-1}{\rho \sqrt{\frac{2}{\rho}(x_3(k) - p_e)}} \Big) \Big], \\ -\frac{T\beta}{V_2^2(x_4(k))} \dot{V}_2(x_4(k)) \Big[- C_d w x_1(k) \sqrt{\frac{2}{\rho}(x_3(k) - p_e)} + A x_5(k) \Big], \\ \frac{T\beta}{V_2(x_4(k))} A, \\ 0, \quad 0 \end{bmatrix} \qquad x_1(k) > 0$$

$$\frac{\partial f_3}{\partial \mathbf{x}} = \begin{bmatrix} \frac{T\beta}{V_2(x_4(k))} \Big(- C_d w x_1(k) \sqrt{\frac{2}{\rho}(p_s - x_3(k))} \Big), \\ 0, \\ 1 + \frac{T\beta}{V_2(x_4(k))} \Big[- C_d w x_1(k) \Big(\frac{-1}{\rho \sqrt{\frac{2}{\rho}(p_s - x_3(k))}} \Big) \Big], \\ -\frac{T\beta}{V_2^2(x_4(k))} \dot{V}_2(x_4(k)) \Big[- C_d w x_1(k) \sqrt{\frac{2}{\rho}(p_s - x_3(k))} + A x_5(k) \Big], \\ \frac{T\beta}{V_2(x_4(k))}(A), \\ 0, \quad 0 \end{bmatrix} \qquad x_1(k) \leq 0$$

$$\frac{\partial f_4}{\partial \mathbf{x}} = [0, \quad 0, \quad 0, \quad 1, \quad T, \quad 0, \quad 0]$$

$$\frac{\partial f_5}{\partial \mathbf{x}} = [0, \quad \frac{T}{m_a} A, \quad -\frac{T}{m_a} A, \quad 0, \quad 1, \quad 0, \quad -\frac{T}{m_a}]$$

$$\frac{\partial f_6}{\partial \mathbf{x}} = [-\omega_n^2 T \quad 0, \quad 0, \quad 0, \quad 0, \quad (-2 d_m \omega_n T + 1), \quad 0]$$

$$\frac{\partial f_7}{\partial \mathbf{x}} = [0, \quad 0, \quad 0, \quad 0, \quad 0, \quad 0, \quad 1]$$

The EKF generates a sequence of estimated state vector, $\hat{\mathbf{x}}_k^+$, given the measurements, $\mathbf{y}_k$, at each sampling time. Selected elements of the estimated state vector are then compared with the corresponding measurements to compute the state residual error, $\mathbf{e}_k$. Choosing the measurements as $\mathbf{y}_k = [x_a(k),\ p_1(k),\ p_2(k)]^{\mathrm{T}}$; we have

$$\mathbf{H}_k = \begin{bmatrix} 0 & 0 & 0 & 1 & 0 & 0 \\ 0 & 1 & 0 & 0 & 0 & 0 \\ 0 & 0 & 1 & 0 & 0 & 0 \end{bmatrix} \tag{6.21}$$

Noise Matrices

Similar to the assumptions in Chapter 4, covariance matrices $\mathbf{Q}_k$ and $\mathbf{R}_k$ are considered to be stationary, white and Gaussian. Furthermore, it is assumed that the noise characteristics of different system state variables are independent of each other. Thus, both $\mathbf{Q}_k$ and $\mathbf{R}_k$ are diagonal, and the values of their elements should be estimated prior to the experiment. Finally, it can be concluded from the assumptions of the noise vectors that the Jacobian matrices of $\mathbf{W}_k$ and $\mathbf{V}_k$ are unity matrices.

System Configuration and Residual Error Generation

Since the hydraulic actuator interacts with external load, it is necessary to apply a closed-loop control scheme to guarantee the actuation system works in normal operating condition. Therefore, the configuration of the proposed system is similar to the closed-loop configuration that has been employed in Section 5.2, shown in Figure 5.24. The measurements of the actuator displacement, x_a, and the chamber pressures, p_1 and p_2, are sampled and delivered to the expanded EKF along with the control

signal, u. By observing the variation of the moving average of the residual errors, $\mathbf{e}_k$, pertaining to the chamber pressures only, leakage faults are identified. Note that although the measurement of actuator displacement is not included in the pattern recognition, it is essential for the EKF to avoid biased estimation.

Under normal operating conditions, the actuation system interacts with varying external loads. The estimates of EKF closely converge to the system states since the effect of the environmental resistance is considered in system modeling. By applying the same residual generating scheme described in Section 4.4, leakage faults can be detected and identified.

Chapter 7

Simulation Analysis and Experimental Results

With the development of the parameter estimation model, a FDI scheme towards online hydraulic actuator leakage fault detection under varying load was proposed in Chapter 6. Choosing the chamber pressures and the actuator displacement as the input for the EKF, this FDI scheme is consistent with the unloaded scheme discussed in Chapter 4. The FDI scheme will be validated by exhaustive simulation and then tested by experiments in this Chapter. Due to the existence of external load, only closed-loop control is implemented on the test rig. Two types of input signals, the sinusoidal and the pseudorandom are applied to the proposed FDI scheme. With the presence of external spring load, the proposed FDI scheme is shown to effectively detect leakage faults both in simulations and experiments.

7.1 Simulation Studies

Simulation of the proposed FDI scheme will be elaborated in this section. The external leakage at each cylinder chamber and the internal leakage between the chambers are considered.

7.1.1 Leakage Faults Detection with Sinusoidal Input

In the simulation, the environmental load is modeled by a linear spring. This is consistent with the actual experimental setting. A virtual spring with a modulus of 2×10^4 N/m is simulated and set to be placed in front of the actuator at the position of 0.22 m. The simulation program tracks the external resistance generated by this virtual spring and records the system states, as well as the simulated leakages. Each simulation test lasts for 60 seconds during which different leakage faults are introduced into the healthy system at the $20\,th$ second. The sinusoidal position references are formulated by the following function: $r(t) = 0.3+0.2\times\sin(\pi t+0.1)$ where t represents the simulation time.

Estimation of Effective Actuator Friction

With the development of FDI scheme in Chapter 6, all external disturbances are regarded as load, including the effective actuator friction. However, the actuator friction is inherent and is always present. When no external load is applied to the actuator, it can be observed from equation (6.9), i.e., $F_e = F_c$ and

$$f_a = m_a\ddot{x}_a + F_c \tag{7.1}$$

Equation (7.1) indicates that the dynamic actuator friction can be theoretically estimated by the FDI scheme. This is verified by simulation. Figure 7.1 shows the plot of actuation force in the presence of only actuator friction. With above analysis, we know this plot actually shows the estimation of simulated actuator friction.

In Figure 7.1, friction is the only external resistance and the actuation force is mainly used to overcome the friction. The second plot shows the simulated friction.

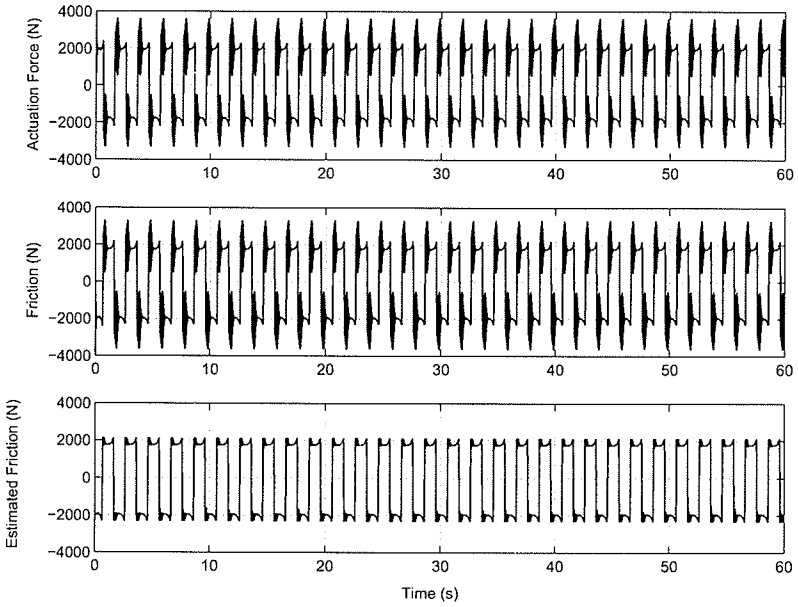

Figure 7.1: Actuation force, simulated friction and estimated friction force.

It can be seen that the estimated friction closely matches the simulated friction that is calculated by the simulation program [see equation (2.13)]. Therefore the dynamic actuator friction can be accurately estimated by running the system unloaded. This verifies the effectiveness of estimating nonlinear external load using the expanded EKF.

Leakage at Chamber 1

Starting from this section, all simulations are conducted in the presence of loading that is generated by a spring model. Figures 7.2 to 7.6 show the simulation results of the leakage at chamber 1. The reference and the valve control signals are shown in Figure 7.2. A leakage coefficient of 2×10^{-12} ($m^3/s \cdot Pa$) is set and the corresponding leakage is shown in Figure 7.3. The simulated and estimated actuator displacements,

which are close to each other, are also shown in this figure. It can be seen from the subplot of MAE that the residual error significantly increases after the occurrence of leakage.

The trajectories of the chamber pressures are shown in Figure 7.4 and 7.5. The residual error of the pressure at chamber 1 significantly increases from the normal level after the occurrence of leakage. Meanwhile, it can be seen that the residual error of the pressure at chamber 2 also slightly increases after the leakage. Considering the parameters of the system and the FDI scheme are kept the same as unloaded mode modeling, this is due to the modification of system modeling. However, pattern of MAE variation under leakage at chamber 1 is still consistent with the conclusion obtained in Chapter 5.

The estimation of the external force is shown in Figure 7.6. The upper plot shows the calculated external force by summing up the friction force and the virtual spring force. The simulated environmental resistance force ranges up to 1500N. This figure shows that the estimated environmental force perfectly matches the calculated values used in the simulation.

Leakage at Chamber 2

The simulation results of the leakage at chamber 2 are shown in Figures 7.7, 7.8 and 7.9. With a leakage coefficient of $2 \times 10^{-12}\,(\mathrm{m}^3/\mathrm{s} \cdot \mathrm{Pa})$, the leakage introduced to the actuation system is shown in Figure 7.7. The corresponding chamber pressures are shown in Figures 7.8 and 7.9, from which it can be seen that the residual error of the pressure at chamber 2 increases significantly, while the residual error at chamber 1 only increase slightly. This trend is consistent with that of the previous simulation

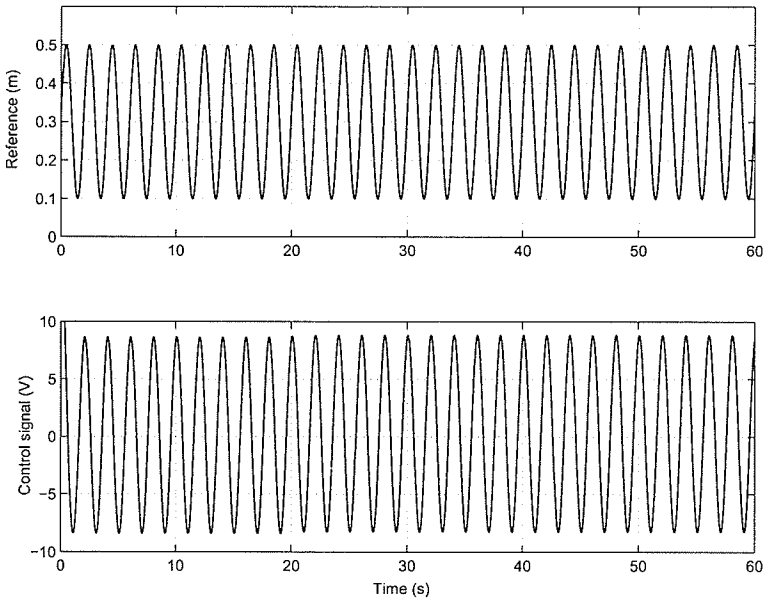

Figure 7.2: Position references for actuator and control signals for servovalve.

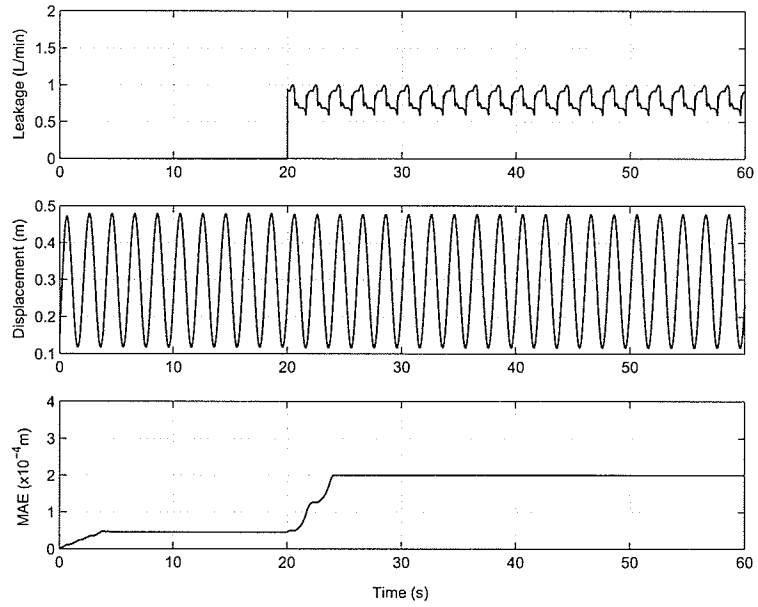

Figure 7.3: Leakage at chamber 1, simulated and overlapped estimated actuator displacements and MAE.

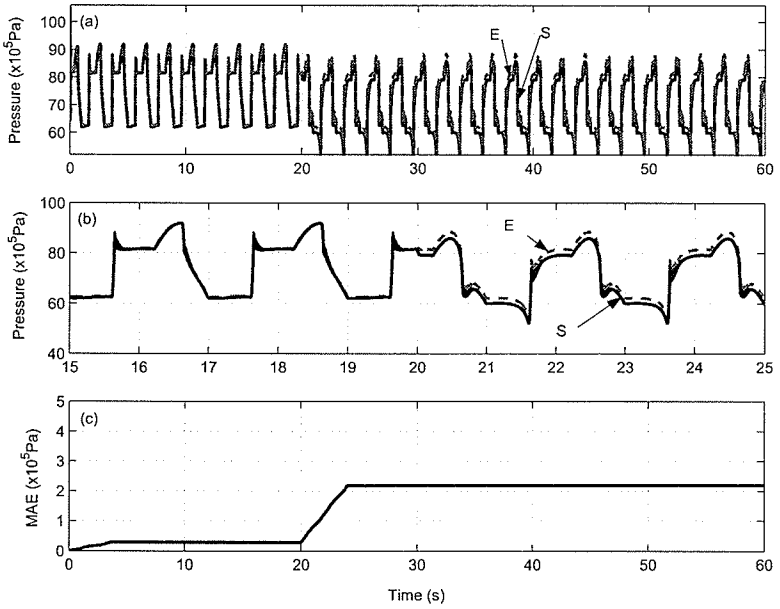

Figure 7.4: Simulated (S) and estimated (E) chamber 1 pressure, closeup plots and MAE.

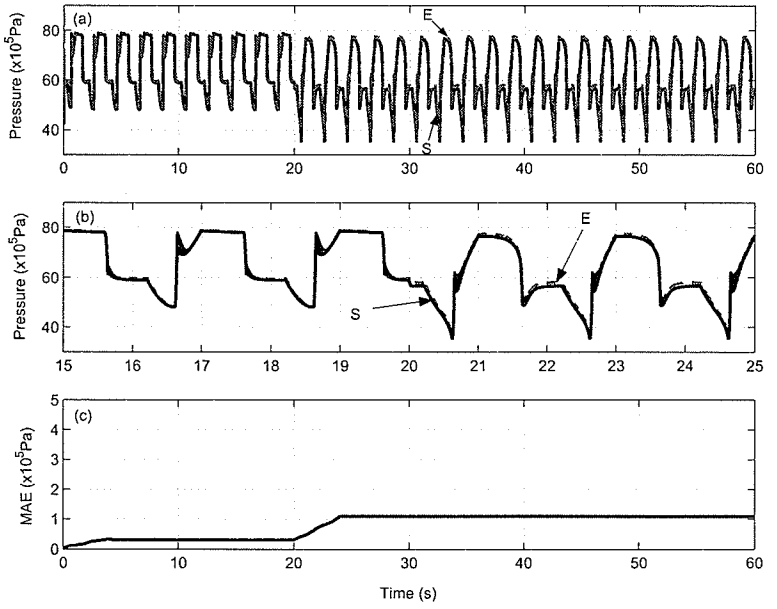

Figure 7.5: Simulated (S) and estimated (E) chamber 2 pressure, closeup plots and MAE.

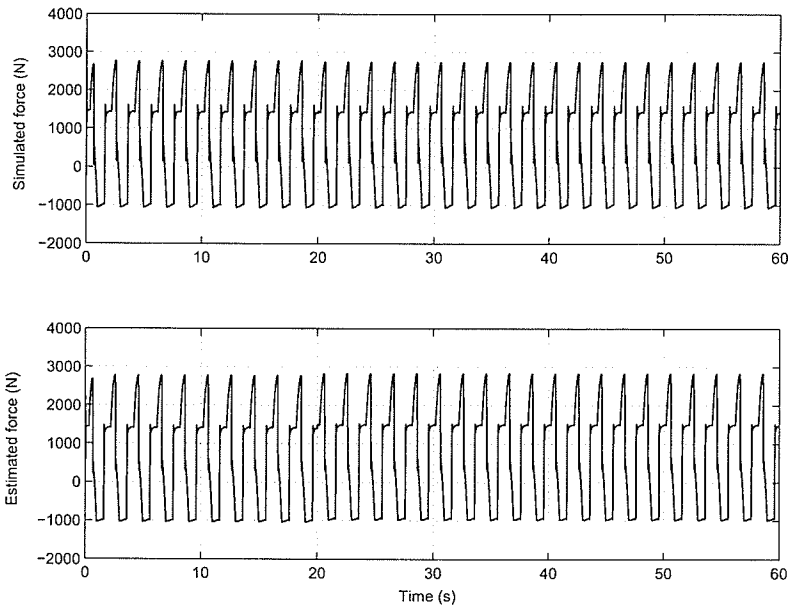

Figure 7.6: Simulated and estimated external force.

and experiments in unloaded mode.

Internal Leakage

The simulation results of the internal leakage are shown in Figures 7.10 to 7.12. A leakage coefficient of $4 \times 10^{-12} (\mathrm{m}^3/\mathrm{s} \cdot \mathrm{Pa})$ is applied. The leakage is bi-directional (featured by positive flow and negative flow) according to the direction of the movement of the actuator and it is also noted that, in Figures 7.10, the leakage on the extension stroke is greater than that of the retraction stroke, which is due to the existence of the external load. The chamber pressures are shown in Figures 7.11 and 7.12. The increase of the MAEs indicates the occurrence of the internal leakage and the increase at both chambers identifies the internal leakage from the external leakages.

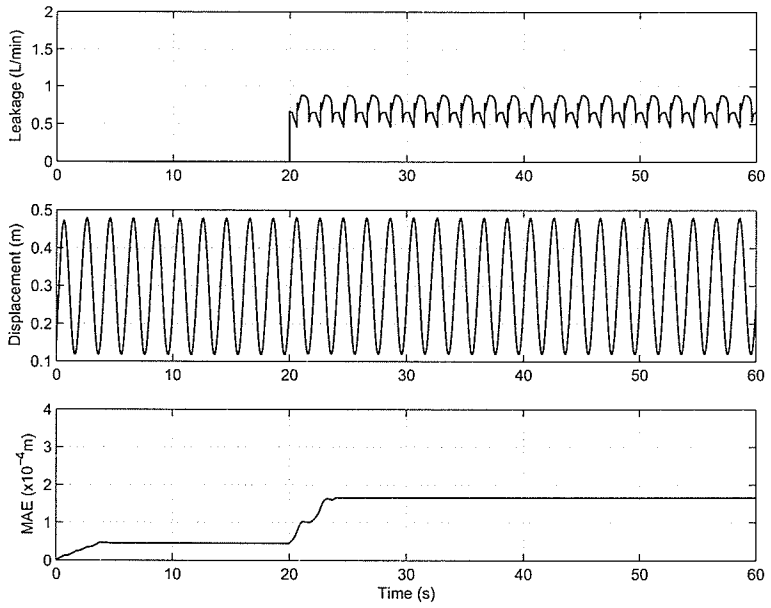

Figure 7.7: Leakage at chamber 2, simulated and overlapped estimated actuator displacements and MAE.

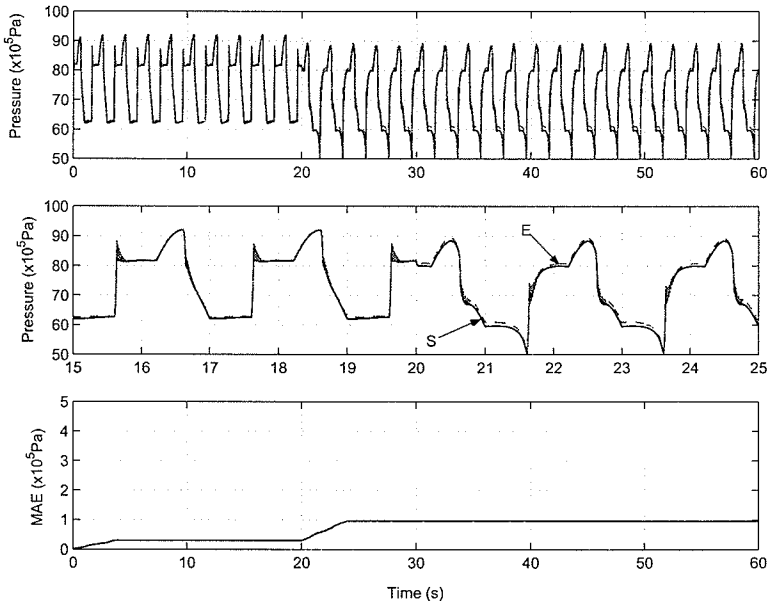

Figure 7.8: Simulated (S) and estimated (E) chamber 1 pressure, closeup plots and MAE.

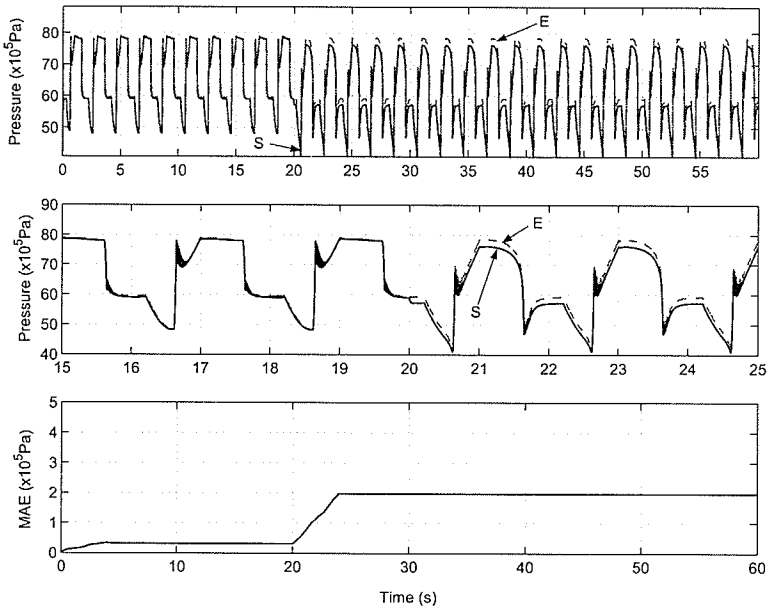

Figure 7.9: Simulated (S) and estimated (E) chamber 2 pressure, closeup plots and MAE.

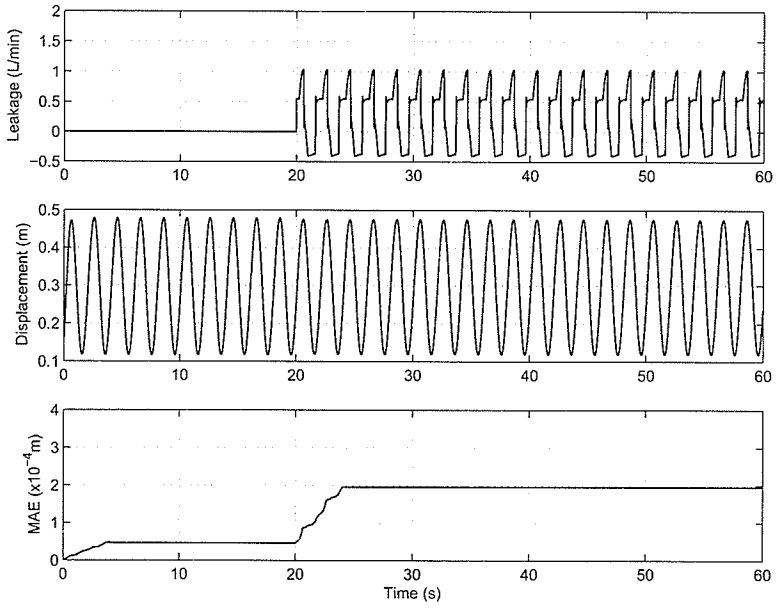

Figure 7.10: Internal (cross-port) leakage, simulated and overlapped estimated actuator displacements and MAE.

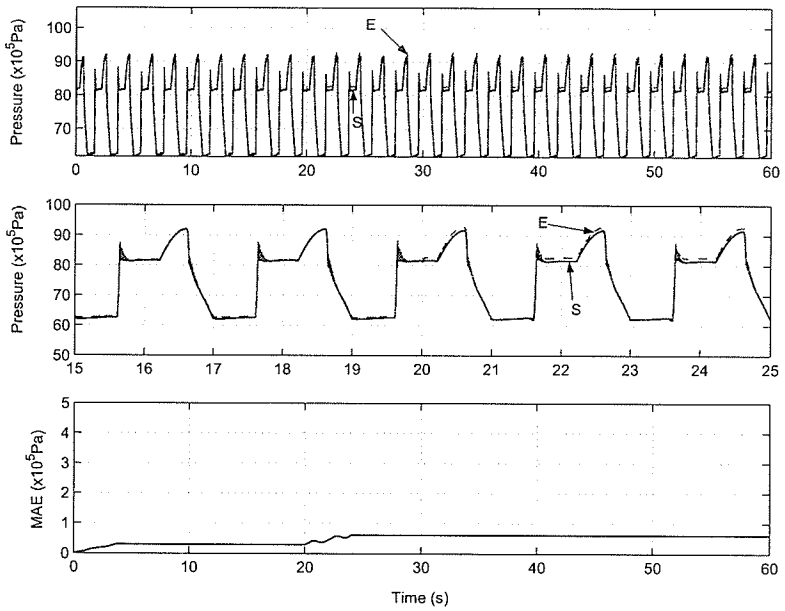

Figure 7.11: Simulated (S) and estimated (E) chamber 1 pressure, closeup plots and MAE.

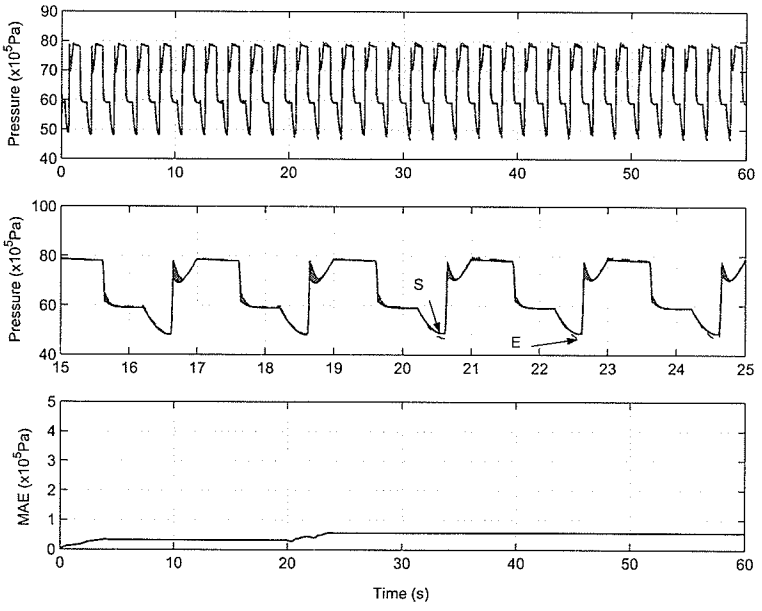

Figure 7.12: Simulated (S) and estimated (E) chamber 2 pressure, closeup plots and MAE.

Different Leakage Levels

The sensitivity of the proposed FDI scheme is tested by simulation. Three levels of leakage are simulated with the occurrence of different type of leakage faults. Figure 7.13 shows that three leakages, with leakage coefficients $2 \times 10^{-12}\,(\mathrm{m}^3/\mathrm{s} \cdot \mathrm{Pa})$, $4 \times 10^{-12}\,(\mathrm{m}^3/\mathrm{s} \cdot \mathrm{Pa})$, and $6 \times 10^{-12}\,(\mathrm{m}^3/\mathrm{s} \cdot \mathrm{Pa})$, are introduced in chamber 1 and consequently, the residual errors of the chamber pressures change. Although the MAE of the pressure at chamber 2 increases proportionally with the increase of leakage, the variation of the residual error at chamber 1 is much more significant. The leakage fault at chamber 1 is obviously featured by the increase of MAE at chamber 1. Comparatively, the variation of MAE with the presence of leakage at chamber 2 is shown in Figure 7.14, in which it can be seen that the residual error at chamber 2 increased more significantly than that of chamber 1. As a result, the difference of MAEs between chambers tells the occurrence of leakage. When the internal leakage is considered, Figure 7.15 shows that the residual errors in both of the chambers equally increased though the magnitudes are relatively small due to the small internal leakage flows. The leakage coefficients applied in the internal leakage simulation are $4 \times 10^{-12}\,(\mathrm{m}^3/\mathrm{s} \cdot \mathrm{Pa})$, $6 \times 10^{-12}\,(\mathrm{m}^3/\mathrm{s} \cdot \mathrm{Pa})$, and $8 \times 10^{-12}\,(\mathrm{m}^3/\mathrm{s} \cdot \mathrm{Pa})$.

The above simulation studies show that the FDI scheme, which is based on the modified model, is effective in leakage detecting and identifying with sinusoidal input signals. The simulation results show that the change of residual errors is consistent to previous conclusion.

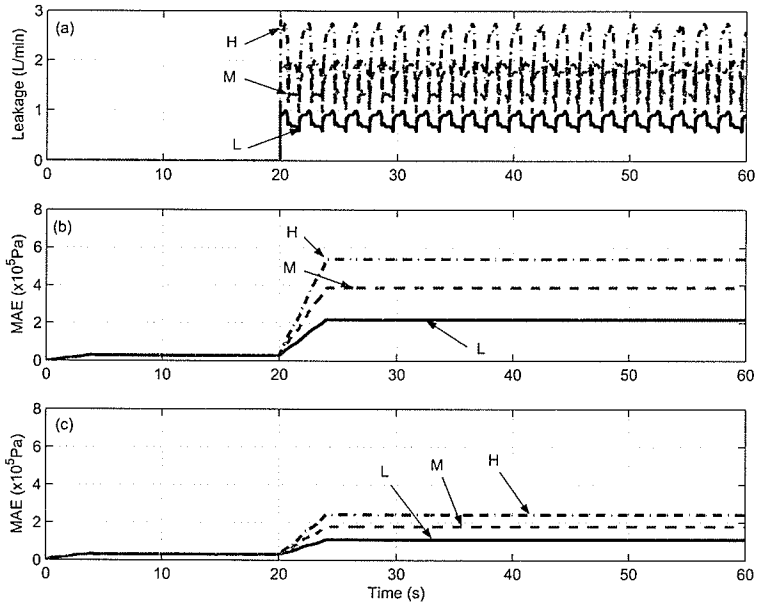

Figure 7.13: Leakages at chamber 1 and MAEs of the chamber pressures. (a) Low (L), medium (M) and high (H) leakages; (b) MAEs at chamber 1; (c) MAEs at chamber 2.

7.1.2 Leakage Faults with Pseudorandom Input

Pseudorandom reference signals are designed to simulate the normal operation conditions for most of applications. The magnitude of the input signal varies randomly between [0.1m, 0.5m] and the duration of the inputs is also considered to be a random variable, which changes between [0.2s, 4.0s]. External and internal leakages are tested and the simulation results are shown in this section.

Leakage at Chamber 1

The reference and the valve control inputs of the test are shown in Figure 7.16. With the change of the reference signals, the control input reached the maximum of ± 10 volts. As a result, severe fluctuation of the leakage is observed in Figure 7.17

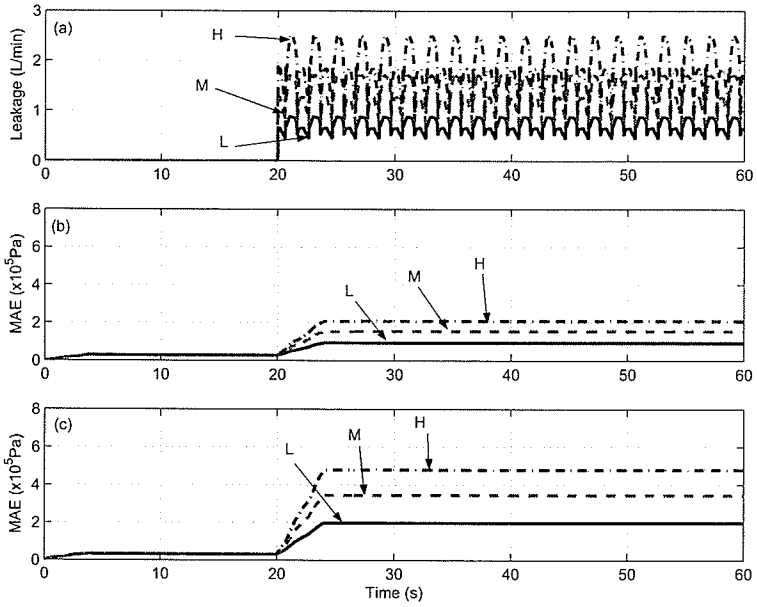

Figure 7.14: Leakages at chamber 2 and MAEs of the chamber pressures. (a) Low (L), medium (M) and high (dashed-dot) leakages; b) MAEs at chamber 1; c) MAEs at chamber 2.

with a leakage coefficient of 2×10^{-12} ($m^3/s \cdot Pa$).

The pressures at chambers 1 and 2 are shown in Figures 7.18 and 7.19. Variation of the moving average of the residual errors indicates the same trend in residual errors with the presence of leakage as that of the sinusoidal input signals. This further verifies the effectiveness of the proposed FDI scheme.

Different Level of Leakage

Two different levels of leakages, with the leakage coefficients of 2×10^{-12} ($m^3/s \cdot Pa$) and 6×10^{-12} ($m^3/s \cdot Pa$), are applied to the simulation tests. Figures 7.20, 7.21 and 7.22 show the simulated leakage and the MAE of both chamber pressures with the presence of leakages at chambers 1, 2 and internal leakage.

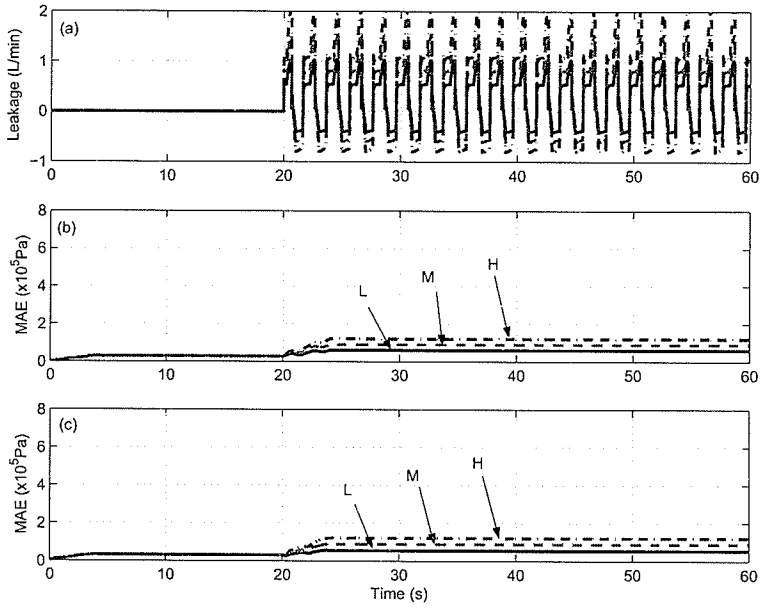

Figure 7.15: Internal leakages and MAEs of the chamber pressures. (a) Low (L), medium (M) and high (H) leakages; (b) MAEs at chamber 1; (c) MAEs at chamber 2.

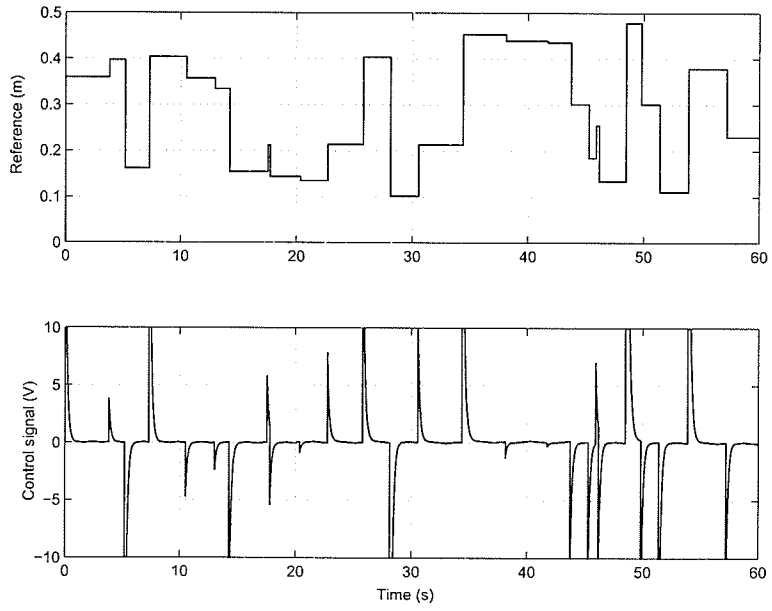

Figure 7.16: Reference inputs and servovalve control signals.

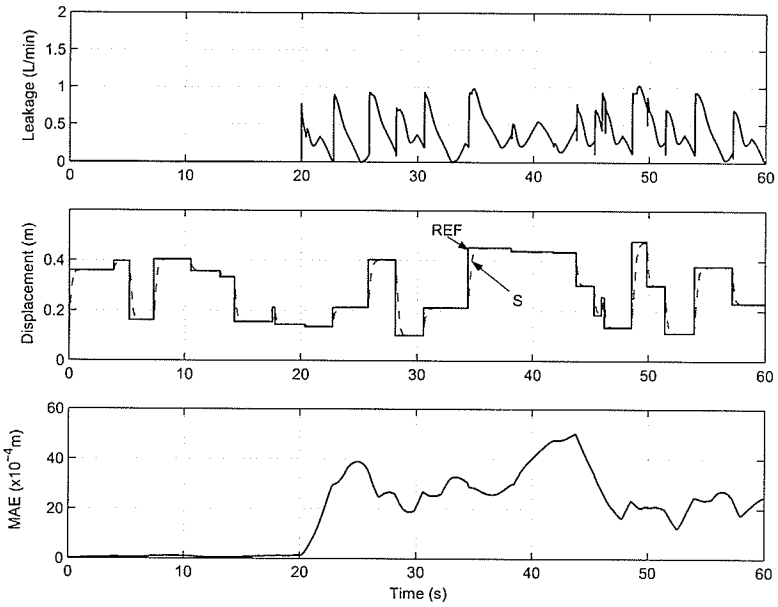

Figure 7.17: Leakage at chamber 1, reference and simulated ram displacement (S) and MAE.

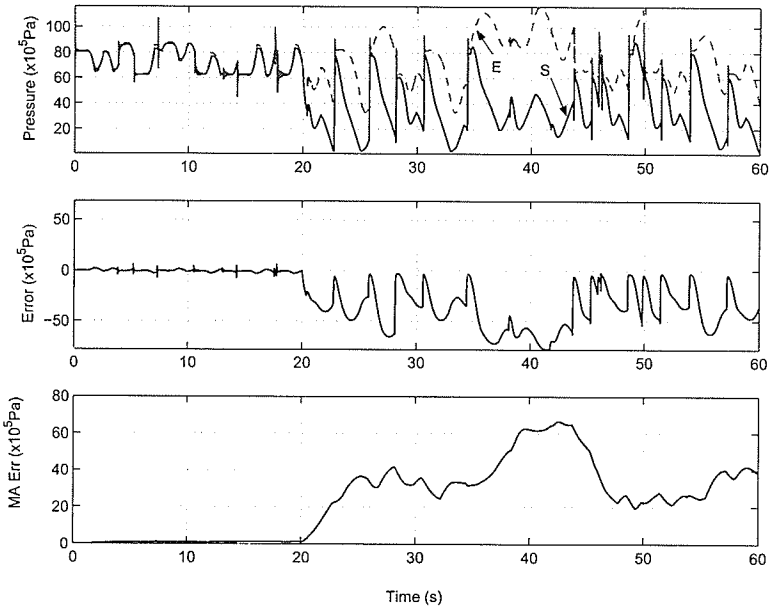

Figure 7.18: Simulated (S) and estimated (E) chamber 1 pressure, residual error and MAE.

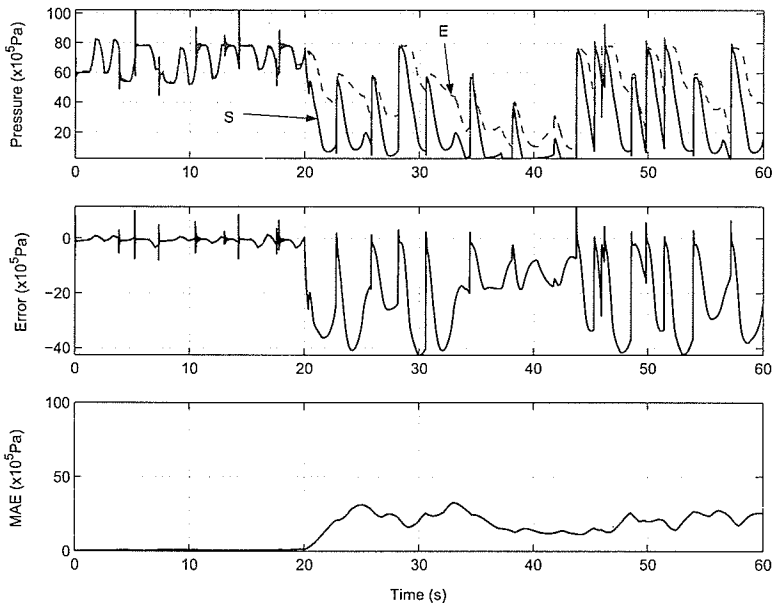

Figure 7.19: Simulated (S) and estimated (E) chamber 2 pressure, residual error and MAE.

Although the leakage and the residual errors fluctuate more due to the randomness of the input signal, it is still obvious that the changes of the residual errors are consistent with previous conclusion.

7.2 Experimental Results

Experiments using sinusoidal and pseudorandom references are carried out on the test rig in this section. A spring with the stiffness of K_{spring} (shown in Figure 6.2), which generates reacting force against the actuator, is fixed in front of the actuator to simulate the environment. The actuator engages the environment at the position of 0.176 m within its extension stroke so that the load of the actuator varies, depending on the depth the actuator compressing the spring, from zero to a certain amount.

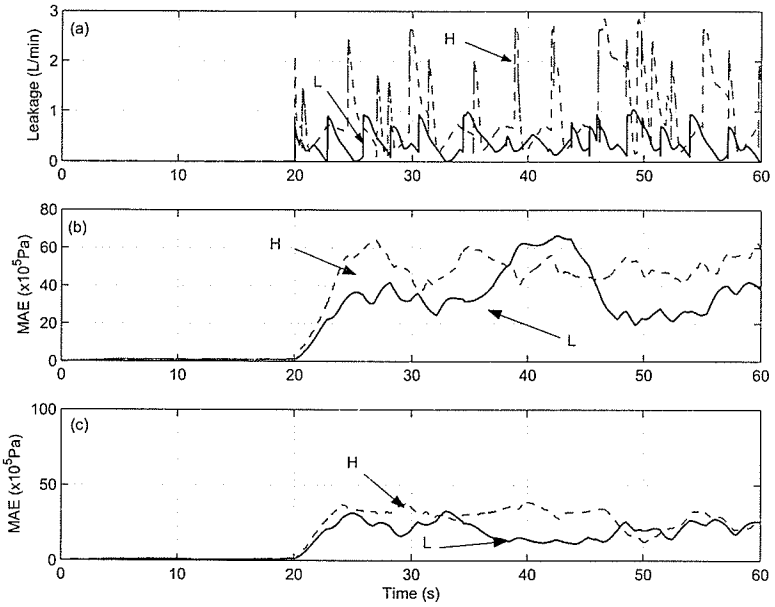

Figure 7.20: Low (L) and high (H) leakage at chamber 1, MAE of pressures at chamber 1 and chamber 2.

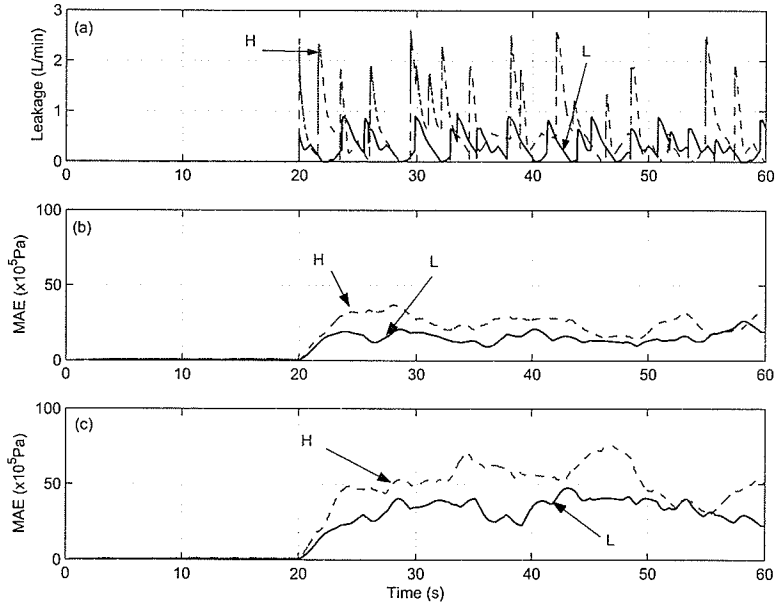

Figure 7.21: Low (L) and high (H) leakage at chamber 2, MAE of pressures at chamber 1 and chamber 2.

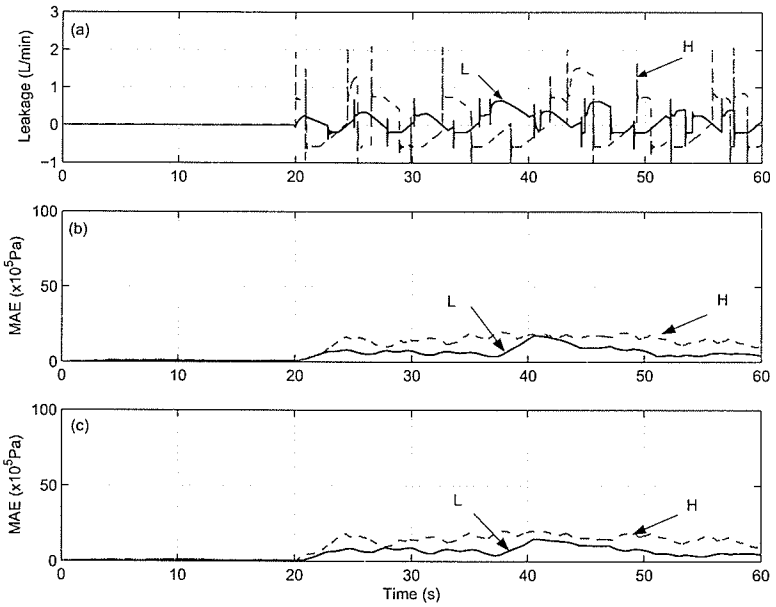

Figure 7.22: Low (L) and high (H) internal leakage, MAE of pressures at chamber 1 and chamber 2.

Only closed-loop control is applied to the experiments. Two sets of position reference signals, the sinusoidal and the pseudorandom, are applied to the system. The leakage faults are introduced to the test rig at $\approx 20\,\mathrm{s}$ of each test and are kept until the end of the test.

The parameters of the test rig, used in the EKF model, have been summarized in Table 2.1, Chapter 2. Besides these parameters, the stiffness of the environment is represented by a coil spring with its elastic modulus, $K_{spring} = 6.0 \times 10^5\,(\mathrm{N/m})$.

Simulation in previous sections has shown that the friction can be estimated in normal conditions. Alternatively, estimation of critical parameters of the friction can be made using the EKF (see Chinniah et al, 2003). Extra experiments in this section will also show that with the proposed FDI scheme, the friction can be estimated

offline in unloaded mode.

The initial state vector, $\hat{\mathbf{x}}_0^+$, and the covariance matrix, $\hat{\mathbf{P}}_0^+$, are set according to section 4.5. Since the extended state is included in the model, $\hat{\mathbf{P}}_0^+$ is a 7×7 matrix and $\hat{\mathbf{x}}_0^+ = [0,\, 6.8 \times 10^6,\, 6.8 \times 10^6,\, 0,\, 0,\, 0,\, 0]^{\mathrm{T}}$.

In order to produce a good convergence rate, the covariance matrices, $\mathbf{Q}_k$ and $\mathbf{R}_k$, are selected based on the combination of system noise analysis, modeling uncertainties and comparison between the simulation and experimental results. Similar to Chapter 5, the matrix $\mathbf{Q}$ is chosen as $\mathbf{Q} = diag[\,10^{-20},\, 10^4,\, 10^4,\, 10^{-6},\, 10^{-4},\, 10^{-20},\, 10^2\,]$ and the matrix $\mathbf{R}$ is given as $\mathbf{R} = diag[\,10^{-4},\, 10^5,\, 10^5\,]$.

With above parameter settings for the proposed FDI scheme, experiments on external and internal leakages are carried out. Extensive experiments show that leakage of $0.25 \sim 0.35\,\mathrm{L/min}$ is the lowest leakage that can be detected by the proposed FDI scheme. Considering the inherent errors of the flow meter, which is around $0.05 \sim 0.1\,\mathrm{L/min}$ even in healthy mode, and the modeling error, this value is regarded small in leakage detection.

7.2.1 Leakage Faults with Sinusoidal Inputs

Similar to the simulation and previous experiments, the sinusoidal references are given as 0.5Hz with the amplitude between [0.167m, 0.187m], $r(t) = 0.177 + 0.02\sin(\pi t)$ m. Each test lasts for 60 seconds and leakage faults are introduced into the system around the $20th$ second.

Leakage at Chamber 1

Experimental results of the test with leakage fault at chamber 1 are shown in Figures 7.23 to 7.26. Experiments show the leakage (0.32 L/min) in Figure 7.23 is the lowest leakage that can be detected by the proposed FDI scheme. From the actual measurement of the leakage flow in Figure 7.23, the leakage coefficient k_{el1} is estimated using equation (5.4). This equation repeated here for convenience:

$$k_{el1} = \frac{1}{10^3 \cdot 60} \cdot \frac{q_{el1}}{\sqrt{(p_1 - p_e)}} = 1.67 \times 10^{-5} \cdot \frac{q_{el1}}{\sqrt{(p_1 - p_e)}}$$

in which the leakage flow q_{el1} is in liter per minute (L/min) and the chamber pressures are in Pascal (Pa). The mean value of leakage coefficient on lower leakage is: $\bar{k}_{el1} = 7.65 \times 10^{-9}\,(\mathrm{m}^3/\mathrm{s} \cdot \mathrm{Pa})$ and the standard deviation is $\sigma_{el1} = 22.08 \times 10^{-10}\,(\mathrm{m}^3/\mathrm{s} \cdot \mathrm{Pa})$.

Compare Figures 7.24 and 7.25. The variation of MAE of the chamber pressures can be clearly observed. Rather than the increase of the residual error at chamber 1, the residual error at chamber 2 even reduces after the occurrence of leakage at chamber 1.

The estimated external force, F_e, is shown in Figure 7.26, which is close to the calculated actuator force, F_a. The measured environmental force is also shown in the same figure and it ranges between [0, 5000 N]. Since the environmental force is available, the actuator friction can thus be calculated according to equation (6.1). Figure 7.26 shows the friction ranges within [-1000, 2000 N]. It is also clear that the measurement for the friction model parameters are [-2400, 2400 N] in Chapter 3. The difference is caused by the wear of the cylinder after large amount of experiments. It shows that the friction model parameters are time-varying and dynamic estimation of these parameters is necessary. Also interesting is that the asymmetry in the positive

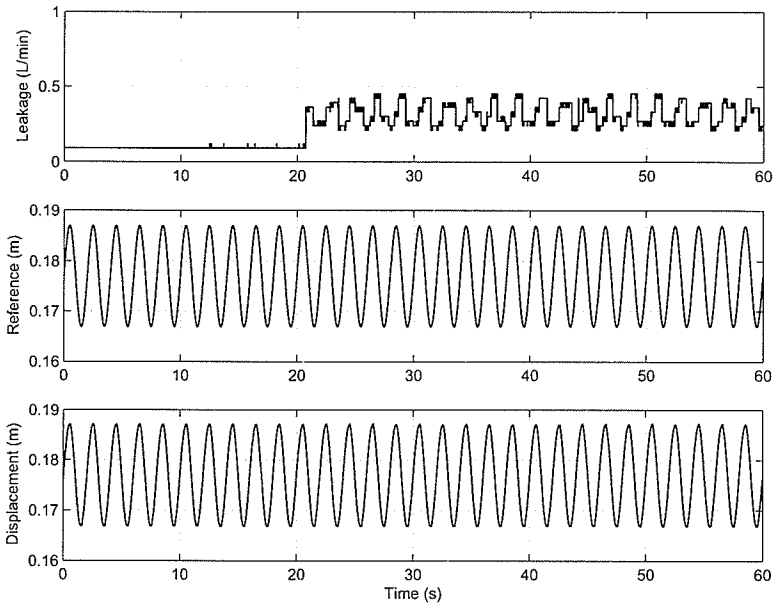

Figure 7.23: Leakage at chamber 1, reference inputs and measured actuator displacement.

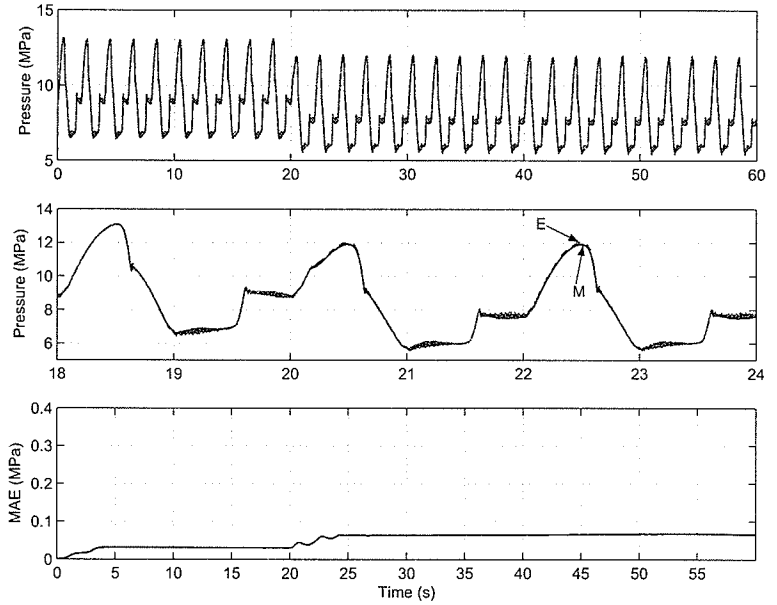

Figure 7.24: Measured (M) and estimated (E) chamber 1 pressure, closeup plots and MAE.

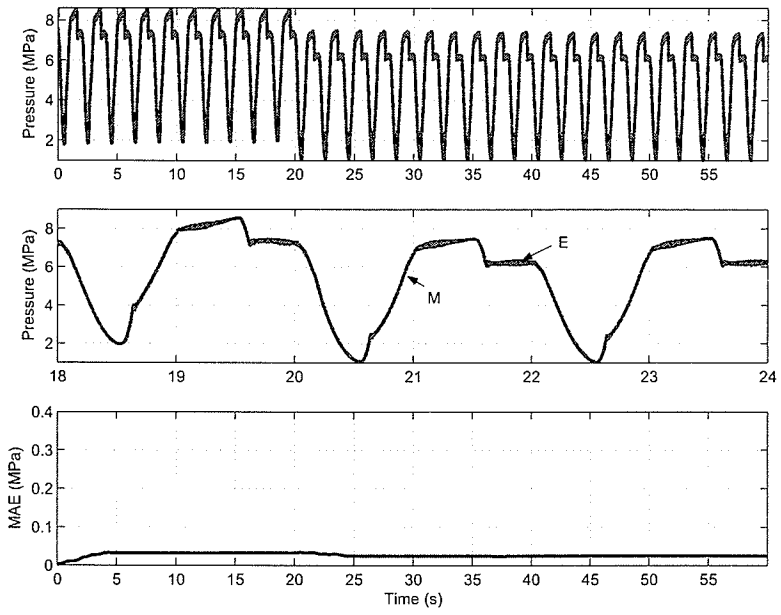

Figure 7.25: Partialy overlapped measured (M) and estimated (E) chamber 2 pressure, closeup plots and MAE.

and negative section of the friction further supports the analysis in Section 3.2 about the drifting of the sinusoidal movement in open-loop configuration.

Leakage at Chamber 2

The test results of leakage at chamber 2 are shown in Figure 7.27. Experiments show the leakage flow of 0.345 L/min is the lowest leakage that can be detected. Similar to the calculation of k_{el1}, the coefficient k_{el2} is estimated as follows:

$$k_{el2} = \frac{1}{10^3 \cdot 60} \cdot \frac{q_{el2}}{\sqrt{(p_2 - p_e)}} = 1.67 \times 10^{-5} \cdot \frac{q_{el2}}{\sqrt{(p_2 - p_e)}}$$

The mean value of the leakage coefficient on lower leakage flow is $\bar{k}_{el2} = 10.68 \times 10^{-9}$ ($m^3/s \cdot Pa$) and the standard variance is $\sigma_{el2} = 31.30 \times 10^{-13}$ ($m^3/s \cdot Pa$). The residual error of the pressure at chamber 2 increases after the occurrence of the leakage

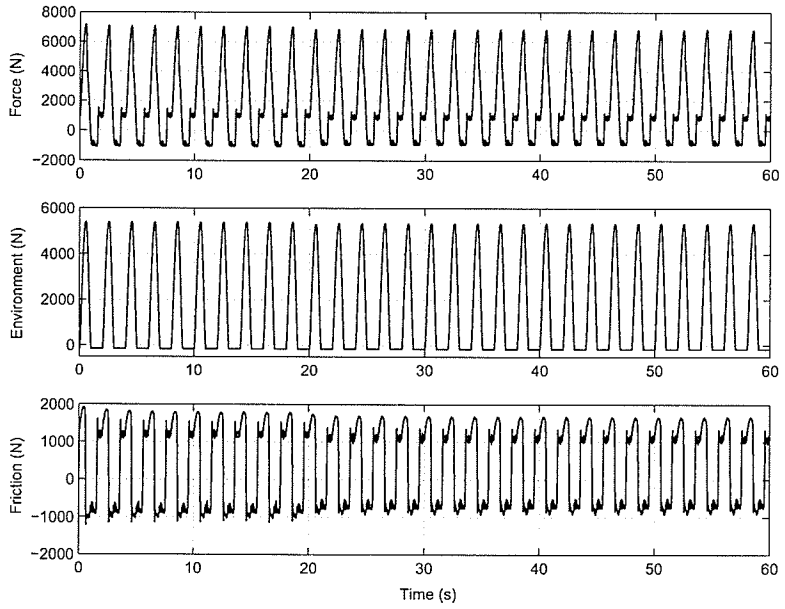

Figure 7.26: Estimated external force, measured environmental force and estimated effective actuator friction.

at the same chamber while the residual error at the other chamber keeps intact.

Internal Leakage

The leakage is shown in Figure 7.28. On average, the leakage is 0.255 L/min, but this is only a rough estimation of the leakage due to the oscillation caused by the external resistance. Since the flow meter is indifferent to the direction of the flow, only positive readings are obtained in the experiments for internal leakage. However, it can be observed that the leakage is much higher when the actuator extends than when it retracts. The external resistance plays a main role on this asymmetry.

Similar to that in previous sections, the estimation of k_{il} is obtained by applying

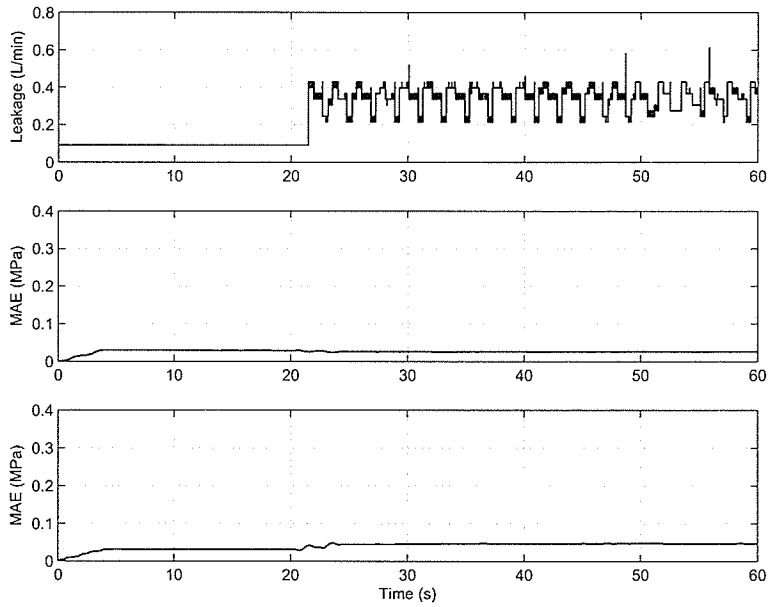

Figure 7.27: Leakage at chamber 2 and MAE of pressures at chamber 1 and chamber 2.

a nonlinear square-root model.

$$k_{il} = \frac{1}{10^3 \cdot 60} \cdot \frac{q_{il}}{\sqrt{|(p_1 - p_2)|}} = 1.67 \times 10^{-5} \cdot \frac{q_{il}}{\sqrt{|(p_1 - p_2)|}}$$

The mean value of the leakage coefficient on lower leakage, $\bar{k}_{il} = 8.65 \times 10^{-9} (\mathrm{m}^3/\mathrm{s} \cdot \mathrm{Pa})$, is obtained and the standard deviation is $\sigma_{il} = 33.22 \times 10^{-10}\ (\mathrm{m}^3/\mathrm{s} \cdot \mathrm{Pa})$.

Different Level of Leakages

Based on the recognition of minimum leakages of different leakages, multilevel leakages are tested and are shown in Figures 7.29, 7.30 and 7.31. For each type of leakage, three levels of leakages are tested. Figure 7.29 shows different levels of leakages at chamber 1 and Table 7.1 shows the average leakage flow before and after the leakage as well as the variation of the moving average of the chamber pressure

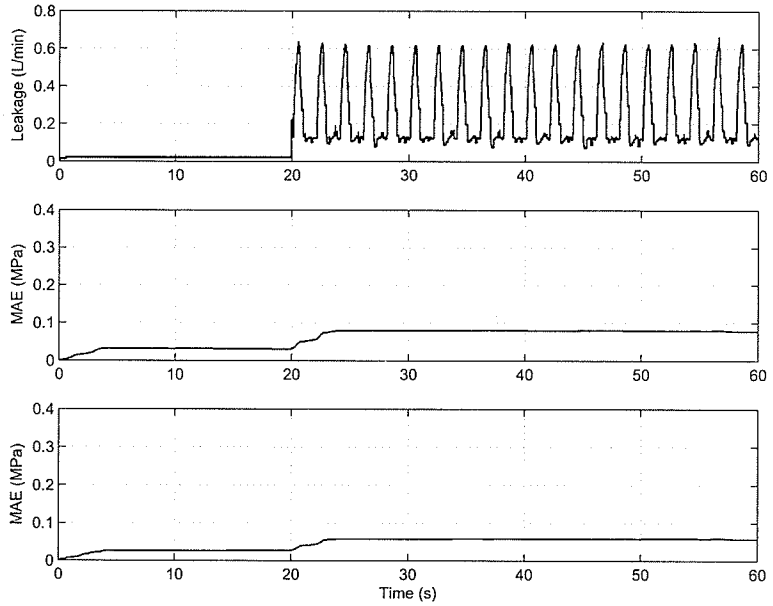

Figure 7.28: Internal leakage, MAE of pressures at chamber 1 and chamber 2.

residuals. From Figure 7.29 it can be seen that, although the fluctuation of the leakage flow increases due to the increase of the bleed valve opening, statistically the leakage increases by observing its arithmetical average values in Table 7.1. Therefore, the MAE at chamber 1 increases proportionally.

Table 7.1: Leakage parameters at chamber 1 and chamber pressure MAEs.

Leakage level	Low		Medium		High	
Faulty status	Before	After	Before	After	Before	After
Average Leakage flow (L/min)	0.09	0.32	0.09	0.46	0.09	0.56
MAE of chamber 1 ($\times 10^5$ Pa)	0.31	0.65	0.30	1.08	0.31	1.33
MAE of chamber 2 ($\times 10^5$ Pa)	0.32	0.25	0.34	0.35	0.36	0.45

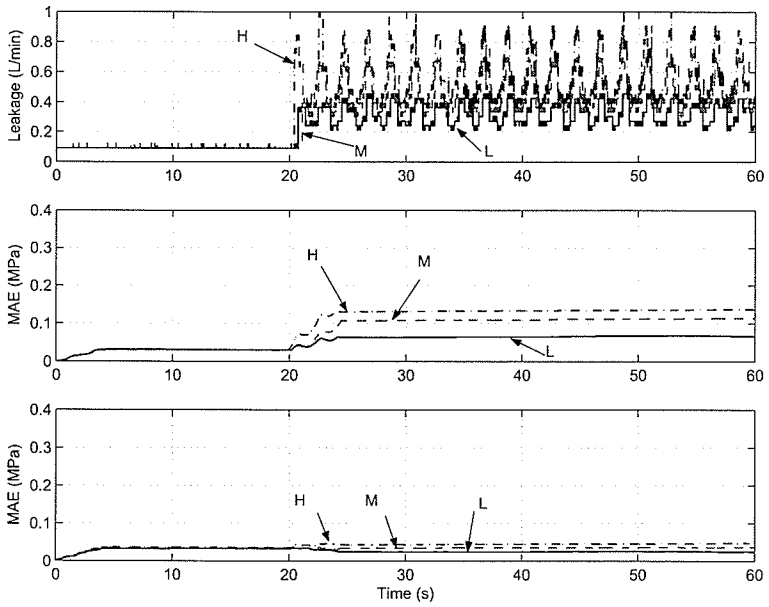

Figure 7.29: Low (L), medium (M) and high (H) leakage at chamber 1, MAE of pressures at chamber 1 and chamber 2.

The leakages at chamber 2 are shown in Figure 7.30, in which the residual error at chamber 2 increases along with the increase of leakage. Corresponding variation of chamber residuals are shown in Table 7.2.

Table 7.2: Leakage parameters at chamber 2 and chamber pressure MAEs.

Leakage level	Low		Medium		High	
Faulty status	Before	After	Before	After	Before	After
Average Leakage flow (L/min)	0.09	0.35	0.09	0.53	0.09	0.68
MAE of chamber 1 ($\times 10^5$ Pa)	0.30	0.26	0.33	0.26	0.34	0.34
MAE of chamber 2 ($\times 10^5$ Pa)	0.31	0.46	0.28	0.93	0.30	1.31

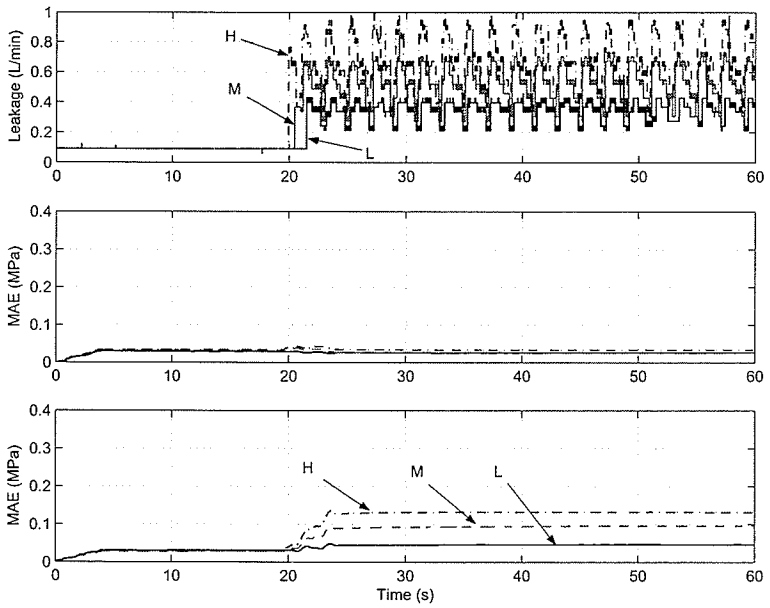

Figure 7.30: Low (L), medium (M) and high (H) leakage at chamber 2, MAEs of pressure at chamber 1 and chamber 2.

Figure 7.31 shows three levels of internal leakage. Corresponding variation of chamber residuals are shown in Table 7.3. It is obvious that with the increase of the opening of the bleeding valve, the leakage in extension stroke increases much more than in retraction stroke.

7.2.2 Leakage Faults with Pseudorandom Inputs

Considering the actual applications of hydraulic actuators, the pseudorandom references are tested with randomly varying magnitude ($0.174 \sim 0.184\,\mathrm{m}$) and duration ($0.2 \sim 4\,\mathrm{s}$) and the duration for each test is 60 seconds.

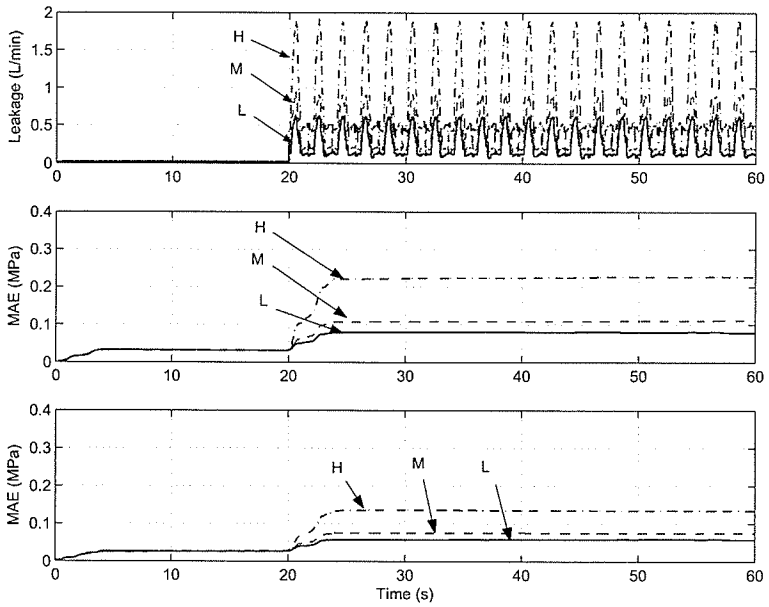

Figure 7.31: Low (L), medium (M) and high (H) internal leakage, MAEs of pressure at chamber 1 and chamber 2.

Table 7.3: Internal leakage parameters and chamber pressure MAEs.

Leakage level	Low		Medium		High	
Faulty status	Before	After	Before	After	Before	After
Average Leakage flow (L/min)	0.02	0.26	0.02	0.38	0.02	0.84
MAE of chamber 1 ($\times 10^5$ Pa)	0.32	0.79	0.32	1.08	0.31	2.23
MAE of chamber 2 ($\times 10^5$ Pa)	0.26	0.58	0.25	0.75	0.27	1.34

Leakage at Chamber 1

Test results for the leakage at chamber 1 are shown in Figures 7.32 to 7.36. With a minimum leakage, 0.32 L/min on average, the test is shown in the following figures.

The variation of the MAE of the chamber pressures is shown in Figures 7.34 and 7.35, in which the MAE at chamber 1 increases accordingly after the occurrence of the leakage.

The estimated external force, F_e, as well as the measurement of the environmental force, are shown in Figure 7.36. The actuator friction is estimated applying equation (6.9). From the plot it can be observed the friction is within the range of [-2400N, 2400N]. This result is consistent to the modeling and previous experiments on determining the friction model.

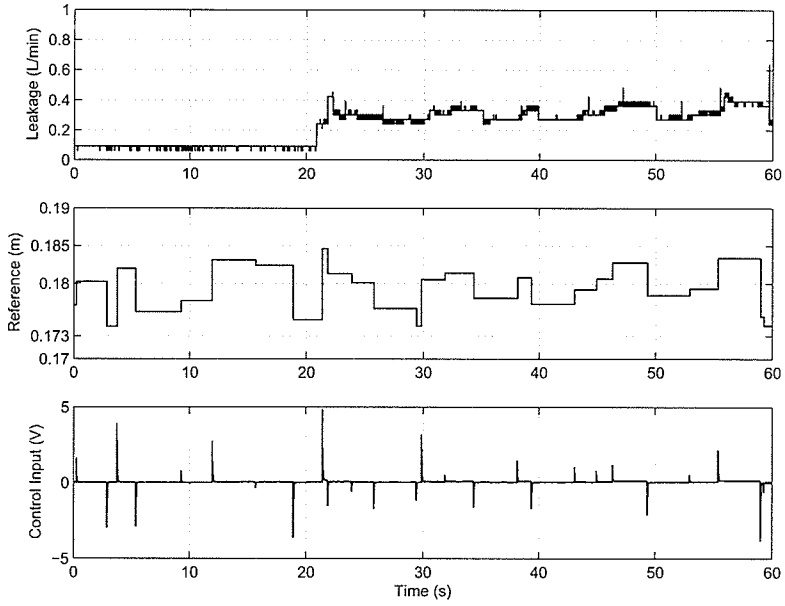

Figure 7.32: Leakage at chamber 1, reference inputs and servovalve control inputs.

Leakage at Chamber 2

Figure 7.37 shows the test of leakage at chamber 2. The moving averages of the residual errors show the increase in the moving average of chamber 2 while the residual

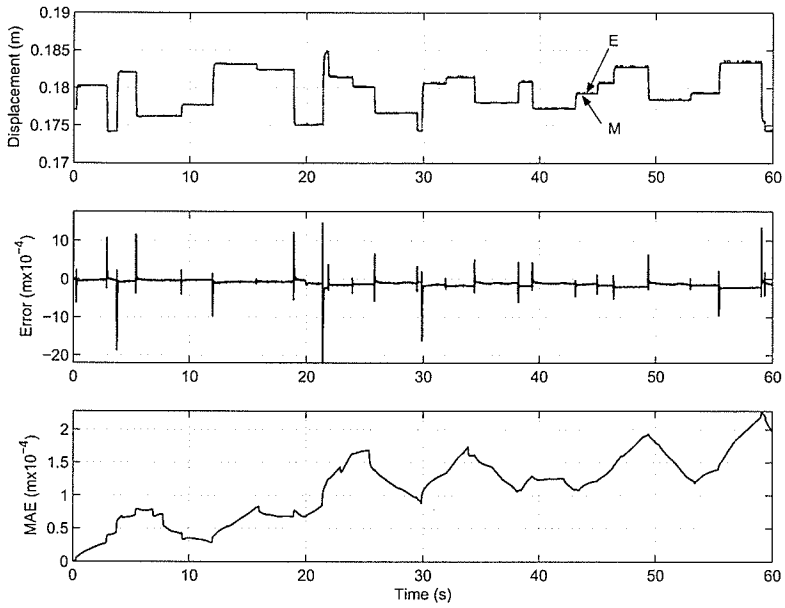

Figure 7.33: Measured (M) and estimated (E) actuator displacements, residual error of the displacement and MAE.

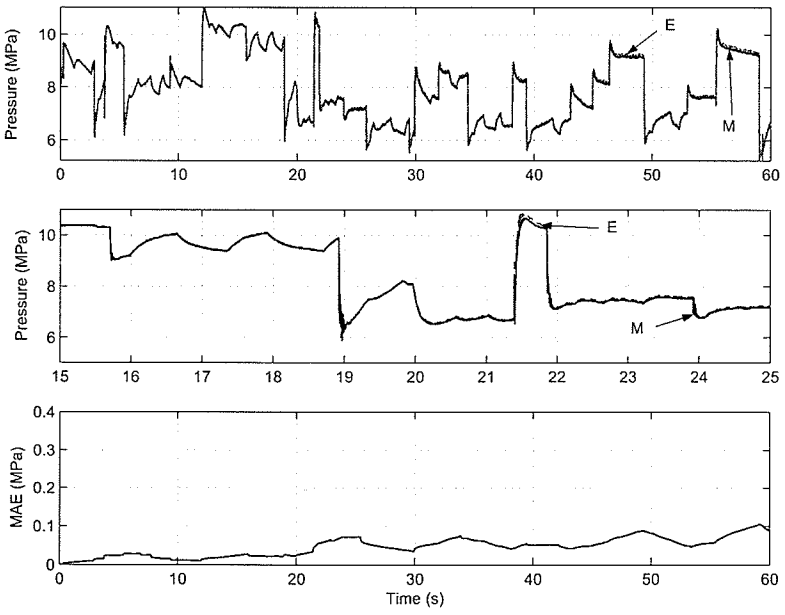

Figure 7.34: Measured (M) and estimated (E) chamber 1 pressure , closeup plots and MAE.

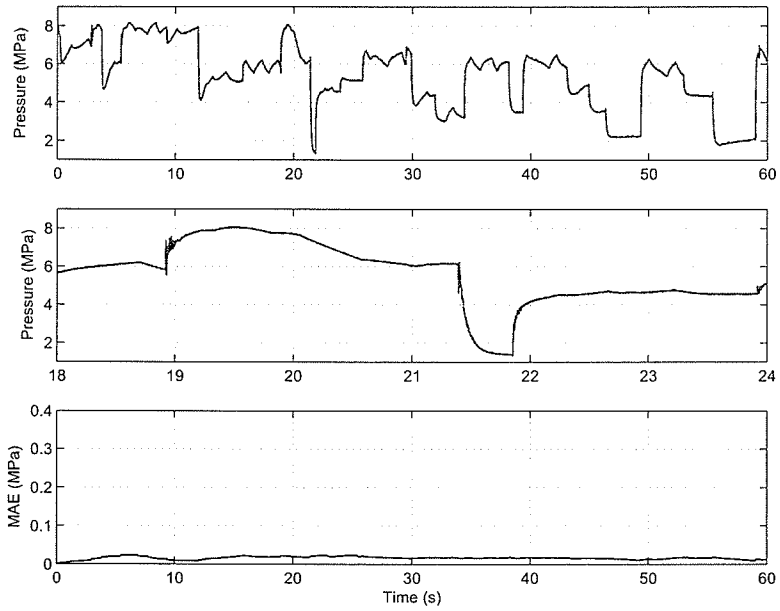

Figure 7.35: Measured (M) and estimated (E) chamber 2 pressure, closeup plots and MAE.

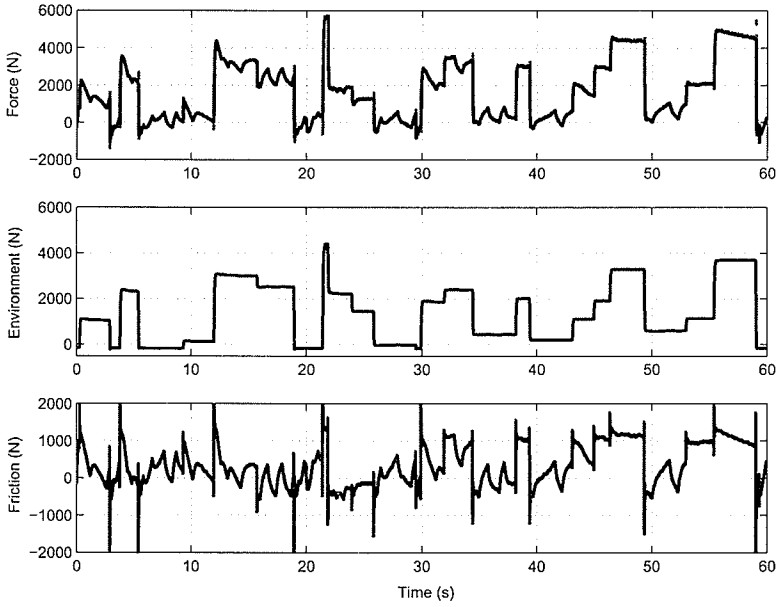

Figure 7.36: Estimated external force, measured environmental resistance (spring force) and estimated friction force.

error in chamber 1 kept at the same level.

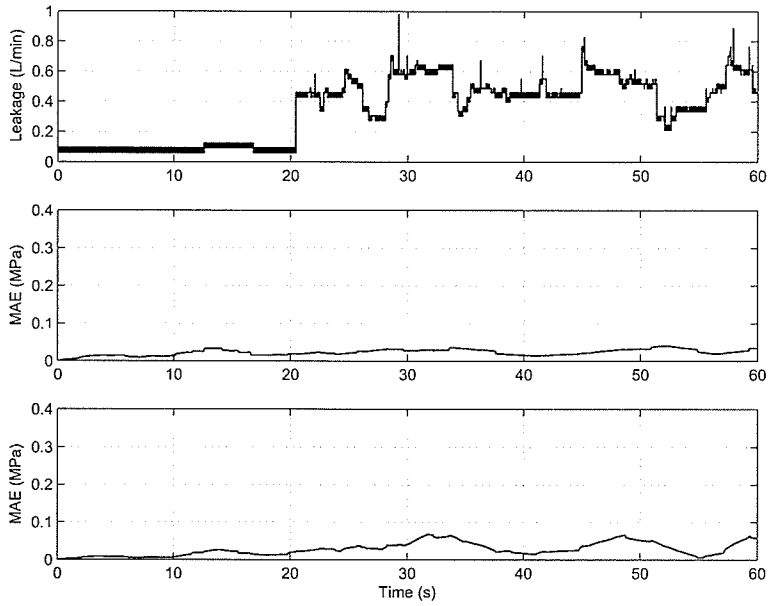

Figure 7.37: Leakage at chamber 2, MAE of pressures at chamber 1 and chamber 2.

Internal Leakage

When the internal leakage is considered, the experiment shows the leakage is more fluctuating and it is hard to characterize the leakage. Accordingly, the moving averages of the residual errors fluctuate more but still increases after the occurrence of leakage, which is shown in Figure 7.38.

Different Level of Leakages

The tests on different levels of leakage are shown in Figures 7.39 to 7.41. Although the trend of the MAEs are deteriorated by the random inputs and the leakage thus oscillates more, the conclusion obtained in Chapter 4 is still applicable.

The above tests clearly show that, in the presence of loading, the actuator leakage

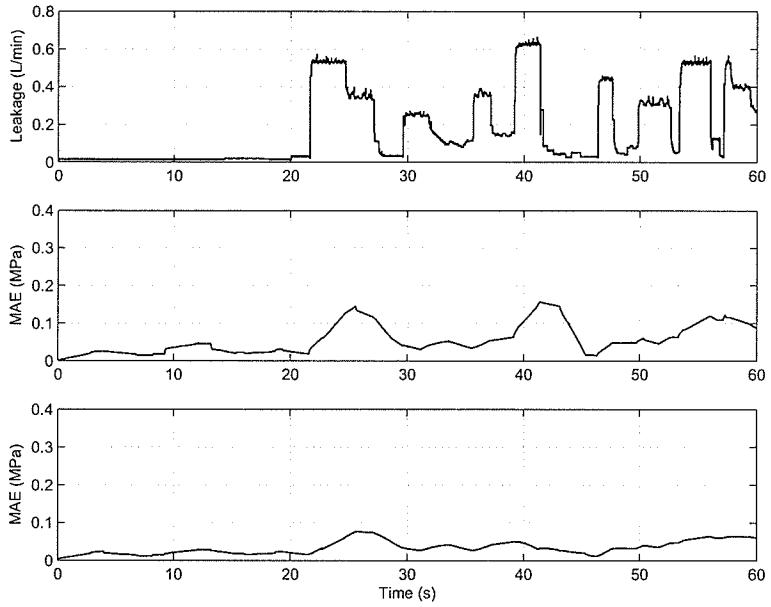

Figure 7.38: Internal leakages, MAE of pressures at chamber 1 and chamber 2.

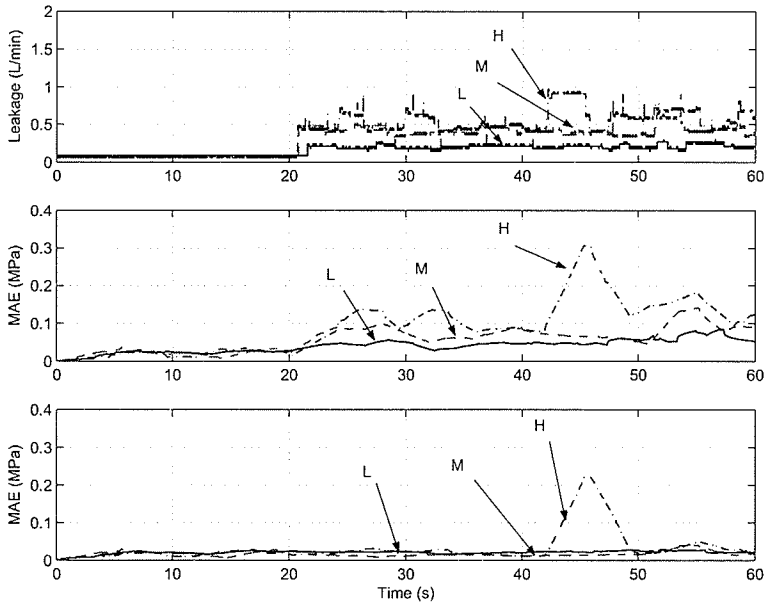

Figure 7.39: Low (L), medium (M) and high (H) leakage at chamber 1, MAE of pressures at chamber 1 and chamber 2.

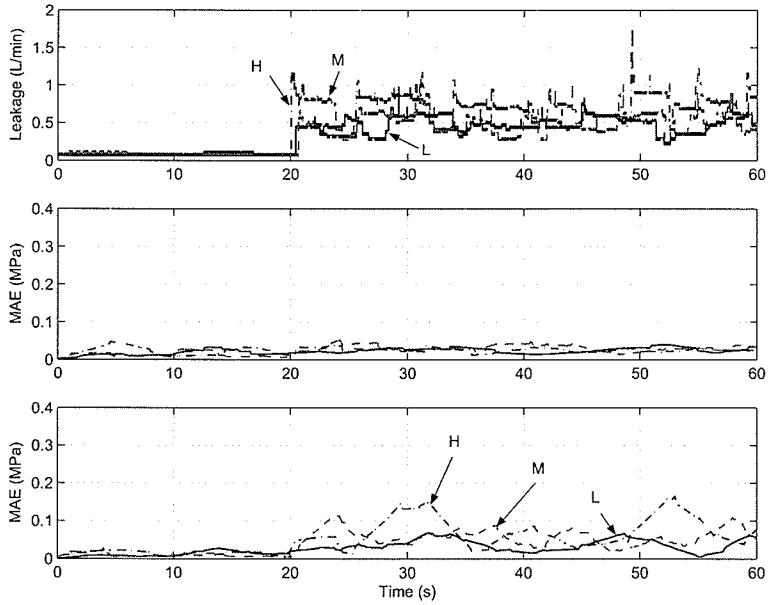

Figure 7.40: Low (L), medium (M) and high (H) leakage at chamber 2, MAE of pressures at chamber 1 and chamber 2.

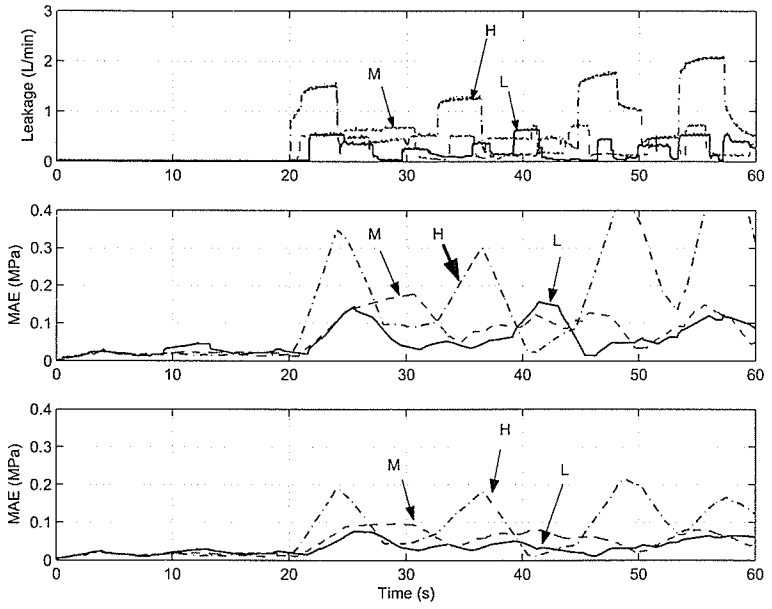

Figure 7.41: Low (L), medium (M) and high (H) internal leakage, MAE of pressures at chamber 1 and chamber 2

can be detected and identified online. By observing the residual error of the chamber pressures one can identify the occurrence of various leakage faults. The increase of the MAE of only one chamber pressure, indicates the occurrence of the external leakage in that chamber, while the increase of the MAE of both chamber pressures indicates the occurrence of internal (cross-port) leakage. However, due to the randomness of the input and the involvement of closed-loop control strategy, the leakage flows are more variable and hard to measure. Consequently, no general average values are available for the moving average errors. On the other hand, it can be observed from Figures 7.39 to 7.41 that the moving average errors increase proportionally when the leakages increase.

Chapter 8

Summary and Contributions

In this research, extended Kalman filter (EKF) based fault detection and isolation (FDI) schemes for hydraulic actuation systems were proposed. The nature of the EKF requires a relatively accurate model of the system under normal operation. If this requirement is satisfied, as shown in this research, the EKF is expected to give good estimation of the observable system states. This conclusion was shown both in simulations and experiments. However, it is difficult to inspect the observability of the hydraulic actuation system due to its nonlinearity; therefore, the theoretical convergence of the algorithm is not determined, though the algorithm converged in all experiments.

An offline actuator leakage fault detection scheme was first developed and both simulations and experiments were carried out to verify the effectiveness of this scheme. Represented by a state space model, the entire actuation system was characterized by six state variables, namely the servovalve solenoid spool displacement and its first derivative, the actuator cylinder chamber pressures, the actuator displacement and the actuator velocity. To more accurately reflect the actual scenario, a velocity dependant friction model (Karnopp) was included in the dynamics of the actuator for

the offline model. Tests with different excitation signals showed that the response of the system model was satisfactory within the bandwidth (up to 10.5 Hz) of normal operations and the maximum simulation error was 10% (chamber pressures).

With a residual generation scheme that compares the actual measurements and the EKF estimation outputs, three types of leakages - external leakage from either side of the actuator and internal leakage between the two chambers of the actuator- were tested. The moving averages of the absolute residual errors were calculated to reflect their trends. By tracking the variation of the residual errors, the leakage faults were detected and identified.

Experiments in open-loop configuration were carried out to test the effectiveness of the EKF based actuator leakage FDI scheme. Sinusoidal inputs were tested to evaluate offline FDI. All the three leakage faults were tested and the FDI strategy was tested with different leakage levels. Experimental results showed that the FDI scheme is able to detect leakages and single actuator leakages can be identified successfully by recognizing the variation pattern of the moving average errors of the chamber pressures. The patterns are indicated by the increase of corresponding moving average error of the chamber pressures, from 10^5 Pa to 1.5×10^5 Pa and higher, proportional to the leakage flow.

The sinusoidal signal test was further conducted in closed-loop configuration. Experiments showed that the proposed FDI strategy can effectively detect and identify the actuator leakage faults in a closed-loop control configuration. The conclusion obtained are consistent with those test results in an open-loop configuration. Therefore, the proposed FDI strategy is suitable for system offline self-test. Additionally,

pseudorandom input tests were also conducted to show the potential of the proposed FDI scheme for online applications. Experiments showed that, with pseudorandom inputs, the EKF estimator still reliably responds to the occurrence of the actuator leakage faults and identifies them.

Finally, experiments showed that, with the increase of the leakage flow, the indicative residual errors increase. This was shown when different levels of leakage were applied to the system. Test results illustrated that the MAE of the residual error of chamber 1 pressure rose up to 1.9×10^5 Pa and 3.4×10^5 Pa with average external leakages of 0.55 L/min and 1.01 L/min at the same chamber. Changes of the MAE of corresponding chamber pressures with external leakages at chamber 2 and internal (crossport) leakages showed similar increases. However, it is difficult to precisely quantitify this increase. This trend can be used to qualitatively evaluate the leakage fault levels in future.

The above tests that were conducted under no-load condition laid the ground for design of the EKF based FDI technique for hydraulic actuators with environmental interactions. The proposed FDI scheme was therefore modified aiming at online fault detection under the more realistic loading condition. The nonlinear system model that includes a comprehensive friction model was improved, and was integrated with modeling of the environment. This modification was based on the consideration of online detection of actuator leakages while the actuation system was loaded with unpredictable resistance. As a result, a method to dynamically estimate the external load was also introduced. Furthermore, actuator friction, modeled as part of the external load in the system, was estimated when the system was running un-loaded,

i.e., a technique for online measuring the actuator friction has been established.

Similar to configurations in the offline mode, with only three measurements, i.e., the actuator displacement and the chamber pressures, the EKF-based fault detector was experimentally shown to successfully identify external and internal leakage faults in the actuator with the existence of external disturbance, which was emulated by a strong coil spring. When working in a fault-free mode, the external load, including the friction, was estimated. Experimental results showed that different patterns obtained were consistent to what had been concluded in offline mode. A minimum leakage of 0.25 to 0.30 L/min was detected using the proposed FDI system.

The approach described in this study can be used towards online condition monitoring of hydraulic systems with respect to actuator leakage faults. Future work should involve the investigation of the stability of the proposed FDI scheme to leakage faults by improving convergence of the key parameter of the EKF - the covariance matrix which should always maintain positive definiteness during the calculation. A possible way to prevent it from degrading into a singular matrix is the computational procedure called square root update (Kaminski, 1971). This was not investigated in this thesis. Furthermore, with the reliable detection of leakage faults and quantified information, fault tolerant control techniques can be applied to improve the performance of hydraulic machinery by re-configuring the controller.

References

[1] Adjallah, K.; Maquin, D. and Ragot, J.; *Nonlinear observer-based fault detection*; Proceedings of the 3rd conference on control applications, 1994, Pages: 1115-1120.

[2] Al-Dabbagh, M., Al-Dabbagh, L.; *Neural networks based algorithm for detecting high impedance faults on power distribution lines*; IJCNN '99 International Joint Conference, Vol. 5, 1999.

[3] Ashton, S.A.; Shields, D.N.; Daley, S.; *Fault detection in pipelines using nonlinear observers*; UKACC International Conference on Control; Vol. 1, 1998, Pages: 135-140.

[4] Beineke, S.; Schutte, F.; Grotstollen, H.; *Online identification of nonlinear mechanics using extended Kalman filters with basis function networks*; 23rd International Conference on Industrial Electronics, Control and Instrumentation; Vol. 1, 1997, Pages: 316-321.

[5] Bonchis, A.; Corke, P.I.; Rye, D.C.; *A pressure-based, velocity independent, friction model for asymmetric hydraulic cylinders*; Proceedings of the IEEE International Conference on Robotics and Automation; Vol. 3, 1999, Pages: 1746-1751.

[6] Borthwick, S.; Durrant-Whyte, H.; *Simultaneous localisation and map building*

for autonomous guided vehicles; Proceedings of the IEEE/RSJ/GI International Conference; Vol. 2, 1994, Pages: 761-768.

[7] Cadman, L.; Tjahjadi, T.; *Efficient Three-Dimensional Metric Object Modeling From Uncalibrated Image Sequences*; Transactions on Systems, Man, and Cybernetics, Part B: Cybernetics; Vol. 34, 2004, Pages: 856-876.

[8] Canudas-de-Wit C.; Olsson, H.; Astrom, K. J.; Lischinsky, P.; *A New Model for Control of Systems with Friction*; IEEE Transactions on Automatic Control; Vol. 40, 1995, Pages: 419-425.

[9] Chinniah Y, Burton, R. and Habibi, S.; *Viscous damping coefficient and effective bulk modulus estimation in a high performance hydrostatic system using extended Kalman filter*; International Journal of Fluid Power; Vol. 4, 2003 Pages: 27-34.

[10] Crowther, W.J.; Edge, K. A.; Atkinson R.M.; and woollons D.J.; *Fault diagnosis of a hydraulic actuator circuit using neural networks - an output vector space classification approach*; Proceedings of the Institution of Mechanical Engineers; Vol. 212, 1998, Pages: 57-68.

[11] Frank, P. M; *Advanced fault detection and isolation schemes using nonlinear and robust observers*; 10th world congress on automatic control; Vol. 3, 1987, Pages: 63-68.

[12] Frank P. M; *On-line fault detection in uncertain nonlinear systems using diagnostic observers: a survey*; International Journal of Systems Science; Vol. 25, 1994, Pages: 2129-2154.

[13] Forest, G. L.; *Visual Inspection of Sea Bottom Structures by an Autonomous Underwater Vehicle*; IEEE Transactions on Systems, Man, And Cybernetics, Part B: Cybernetics; Vol. 31, 2001 Pages: 691-705.

[14] Garcia, E. A. and Frank, P.M.; *Deterministic nonlinear observer-based approaches to fault diagnosis: A survey*; Control Engineering Practice; Vol. 5, 1997, Pages: 663-670.

[15] Gaddouna, B.O.; Ouladsine, M.; *Fault diagnosis in a hydraulic process using unknown input observers*; Proceedings of the IEEE International Conference on Control Applications; 1997, Pages: 490-495.

[16] Gertler, J; *Fault detection and isolation using parity relations*; Control Engineering Practice; Vol. 5, 1997, Pages: 653-661.

[17] Hahn, Jin-Oh; Hur, Jae-Woong; Cho, Young Man; Lee, Kyo Il; *Robust observer-based monitoring of a hydraulic actuator in a vehicle power transmission control system*; Proceedings of the IEEE International Conference on Control Applications; 2001, Pages: 805-810.

[18] He, S.; Sepehri, N., *Online modeling and prediction of a hydraulic force-acting system using neural networks*; Systems, Man, and Cybernetics, 2000 IEEE International Conference; Vol. 4, 2000, Pages: 2667-2672.

[19] Haykin, S., Edited by; *Kalman filtering and neural networks*; John Wiley & Sons, Inc. New York, N.Y. 2001

[21] Isermann, R.; *Estimation of physical parameters for dynamic processes with application to an industrial robot*; International Journal of Control; Vol. 55, 1992, Pages: 1287-1298.

[21] Isermann, R.; *Supervision, fault-detection and fault-diagnosis methods-an introduction*; Control Engineering Practice; Vol. 5, 1997, Pages: 639-652.

[22] Jazwinski, H. A.; *Stochastic processes and filtering theory*; Academic press, 1970.

[23] Kalman, Rudolph Emil;*A New Approach to Linear Filtering and Prediction Problems*; Transactions of the ASME–Journal of Basic Engineering; Vol. 82, 1960, Pages: 35-45.

[24] Kaminski, G. P.; Bryson, E. A., JR.; Schmidt, F. S.; *Discrete square root filtering: a survey of current Techniques*; IEEE Transactions on automatic control; Vol. AC-16, 1971, Pages: 727-736.

[25] Khan, H.; Abou, S. and Sepehri, N.; *Fault detection in electro-hydraulic servo-positioning systems using sequential test of Wald*; Proceedings of the 2002 Canadian conference on electrical & Computer Engineering; 2002, Pages: 1628-1633.

[26] Khoshzaban, M.; Sassani, F.; Lawrence, P.D.; *Online state and parameter estimation of an electrohydraulic valve for intelligent monitoring*; IEEE/ASME International Conference on Advanced Intelligent Mechatronics; 1997, Pages: 141-146.

[27] Krishnaswami V., Rizzoni G.; *A survey of observer based residual generation for FDI*; IFAC Fault Detection, Supervision and Safety for Technical Processes; Espoo, Finland, 1994.

[28] Kwak, B-J.; Yagle, A.E.; Levitt, J.A., *Nonlinear system identification of hydraulic actuator friction dynamics using a finite-state memory model*; IEEE International Conference on Acoustics, Speech, and Signal Processing; Vol. 3, 1999, Pages: 1309-1312.

[29] Laval, L.; M'Sirdi, N.K.; Cadiou, J.-C., *H_∞-force control of a hydraulic servo-actuator with environmental uncertainties*; Proceedings of the IEEE International Conference on Robotics and Automation; Vol. 2, 1996, Pages: 1566-1571.

[30] Le, T.T.; Watton, J. and Pham, D.T.; *Fault classification of fluid power systems using a dynamics feature extraction technique and neural networks*; Proceedings of the Instn Mechanical Engineers; Vol. 212 Part I; 1998, Pages: 87-96.

[31] Lin, F.-J.; *Robust speed-controlled induction-motor drive using EKF and RLS estimators*; IEE Proceedings: Electric Power Applications; Vol. 143, 1996, Pages: 186-192.

[32] Lischinsky, P.; Canudas-de-Wit, C.; Morel, G.; *Friction compensation for an industrial hydraulic robot*; IEEE Control Systems Magazine; Vol. 19, 1999, Pages: 25-32.

[33] Maybeck, S.P.; *Stochastic models, estimation, and control*; Volume 1, Academic press, 1979.

[34] McCormick, A.C., Nandi, A.K., Jack, L.B.; *Application of periodic time-varying autoregressive models to the detection of bearing faults*; Journal of Mechanical Engineering Science, Vol. 212, 1998, Pages: 417-428.

[35] Merrit, H. E.; *Hydraulic Control Systems*, Wiley, New York, 1967.

[36] Niksefat, N. and Sepehri, N.; *A QFT fault-tolerant control for electrohydraulic positioning systems*; IEEE transactions on control systems technology; Vol. 10, 2002, Pages 626-632.

[37] Patton, R.J. and Chen, J.; *Observer-based fault detection and isolation: Robustness and applications*; Control Engineering Practice; Vol. 5, 1997, Pages: 671-682.

[38] Preston, G.J.; Shields, D.N.; Daley, S.; *Application Of A Robust Nonlinear Fault Detection Observer To A Hydraulic System*; UKACC International Conference on Control; Vol. 2, 1996, Pages: 1484-1489.

[39] Sepehri, N.; Sassani, F.; Lawrence, P. D.; Ghasempoor A.; *Simulation and Experimental Studies of Gear Backlash and Stick-slip Friction in hydraulic Excavator Swing Motion*; Journal of Dynamic Systems, Measurement, and Control; Vol. 118, 1996, Pages: 463-467.

[40] Skormin, V.A.; Apone, J.; *On-line diagnostics of a variable displacement pump of a flight actuation system*; Proceedings of the IEEE 1995 National Aerospace and Electronics Conference; Vol. 1, 1995, Pages: 503-510.

[41] Skormin, V.A.; Apone, J.; Dunphy, J.J.; *On-line diagnostics of a self-contained flight actuator*; IEEE Transactions on Aerospace and Electronic Systems; Vol. 30, 1994, Pages: 186-196.

[42] Snider, L.A.; Yuen Yee Shan; *The artificial neural networks based relay algorithm for distribution system high impedance fault detection*; Fourth International

Conference on Advances in Power System Control, Operation and Management; Vol. 1, 1997, Pages: 100-106.

[43] Song, R.; Sepehri, N.; *Fault detection and isolation in fluid power systems using a parametric estimation method*; IEEE Canadian Conference on Electrical and Computer Engineering; Vol. 1, 2002, Pages: 144-149.

[44] Sridhar, B.; Smith, P.; Suorsa, R.E.; Hussien, B.; *Multirate and event-driven Kalman filters for helicopter flight*; IEEE Control Systems Magazine; Vol. 13, 1993, Pages: 26-33.

[45] Tan, Hong-Zhou; Sepehri, N.; *Parametric fault diagnosis for electrohydraulic cylinder drive units*, IEEE Transactions on Industrial Electronics; Vol. 49, 2002, Page(s): 96-106.

[46] Welch, G.; Bishop, G.; *An introduction to the Kalman Filter*; UNC-Chapel Hill, 2001.

[47] Yang, H.; Saif, M.; *Monitoring and diagnostics of a class of nonlinear systems using a nonlinear unknown input observer*; Proceedings of the IEEE International Conference on Control Applications; 1996, Pages: 1006-1011.

[48] Yu, Dingli; Shields, D.N.; Mahtani, J.L.; *Fault detection for bilinear systems with application to a hydraulic system*; Proceedings of the Third IEEE Conference on Control Applications; Vol. 2, 1994, Pages: 1379-1384.

[49] Yu, D.; *Fault diagnosis for a hydraulic drive system using a parameter-estimation method*; Control Engineering Practice; Vol 5, 1997, Pages: 1283-1291.

[50] Yu, Xiaohui; Liao, Ruijin; Yao, Chenguo; *Fault diagnosis in hydraulic turbine governor based on BP neural network*; Proceedings of the Fifth International Conference on Electrical Machines and Systems; Vol. 1, 2001, Pages: 335-338.

[51] Zavarehi, M. K.; Lawrence, P. D. and Sassani, Farrokh; *Nonlinear modeling and validation of solenoid-controlled pilot-operated servovalves*; IEEE/ASME Transactions on Mechatronics; Vol. 4, 1999, Pages: 324-334.

[52] Zhang, Y.M. and Jiang, J.; *Active fault-tolerant control system against partial actuator failures*; IEE Proceedings of Control Theory Application; Vol. 149, 2002, Pages: 95-104.

[53] Zhou, R.; Lin, T.; Han, J.; Yan, D.; *Fault diagnosis of airplane hydraulic pump*; proceedings of the 4th World Congress on Intelligent Control and Automation; Vol. 4, 2002, Pages: 3150-3152.